MICRO-SCANNING MIRRORS AND LENSES FOR IMPROVING IMAGE RESOLUTION

A THESIS SUBMITTED TO
THE GRADUATE SCHOOL OF NATURAL AND APPLIED SCIENCES
OF
MIDDLE EAST TECHNICAL UNIVERSITY

BY

AHMET SÖZAK

IN PARTIAL FULFILLMENT OF THE REQUIREMENTS
FOR
THE DEGREE OF DOCTOR OF PHILOSOPHY
IN
MICRO AND NANOTECHNOLOGY

MAY 2022

Approval of the thesis:

MICRO-SCANNING MIRRORS AND LENSES FOR IMPROVING IMAGE RESOLUTION

submitted by **AHMET SÖZAK** in partial fulfillment of the requirements for the degree of **Doctor of Philosophy in Micro and Nanotechnology Department, Middle East Technical University** by,

Prof. Dr. Halil Kalıpçılar
Dean, Graduate School of **Natural and Applied Sciences**

Prof. Dr. Deniz Üner
Head of Department, **Micro and Nanotechnology**

Assoc. Prof. Dr. Kıvanç Azgın
Supervisor, **Micro and Nanotechnology, METU**

Examining Committee Members:

Assoc. Prof. Dr. Emre Yüce
Physics, Middle East Technical University

Assoc. Prof. Dr. Kıvanç Azgın
Micro and Nanotechnology, METU

Assoc. Prof. Dr. Erdem Akagündüz
Electrical and Electronics Engineering, METU

Assist. Prof. Dr. Emir Kutluay
Mechanical Engineering, Hacettepe University

Assist. Prof. Dr. Abdullah Demir
Materials Science and Nanotechnology, Bilkent University

Date: 18.05.2022

I hereby declare that all information in this document has been obtained and presented in accordance with academic rules and ethical conduct. I also declare that, as required by these rules and conduct, I have fully cited and referenced all material and results that are not original to this work.

Name, Surname: Ahmet Sözak

Signature:

ABSTRACT

MICRO-SCANNING MIRRORS AND LENSES FOR IMPROVING IMAGE RESOLUTION

Sözak, Ahmet
Doctor of Phılosophy, Micro and Nanotechnology
Supervisor: Assoc. Prof. Dr. Kıvanç Azgın

May 2022, 156 pages

Enhancement of image resolution has been one of the main interests in optical research for many years. In this context, many different methods have been developed. While some of these methods found use in the field, some remained at the level of laboratory demonstration. There have been numerous approaches to reduce the pixel size of staring focal plane array detectors since 1980, and the number of pixel on unit area and resolution are increased since then. However, the difficulty at the fabrication of small pixel pitch and limited fill-factor of the pixel structure of focal plane array are critical limitations of this method especially at the infrared wavelengths. Micro scanning the other method in order to obtain resolution enhancement has proven its applicability in the field. There are many variants of the application of this technique such as the scanning of lenses, mirrors, prisms and coded mask for resolution enhancement. The macro and micro actuators are utilized for scanning of optical components in different optical architectures. Conventional micro scanning systems for the infrared imaging have a size from 50mm range up to 200 mm, need a large space in optical system and consume high power and excitation voltage from 45V range up to 150 V due to bulky optical components and actuators. Also, the conventional micro scanning systems for infrared imaging have high part quantity and need to use separate compliance mechanism parts for the displacement amplification.

The aim of this study is to develop a novel Micro-Opto-Electro-Mechanical System (MOEMS) with small size, large displacement and low power consumption for the stabilization and enhancement of the resolution of a real macro scale infrared imaging system. In this context, throughout this study a piezo electrical, a thermal and an electro-magnetic micro scanning system were designed and optimized by using CAD modeling and parametrical multi-physics finite element analysis with both PTC CREO and ANSYS. Optical architecture, ray tracing and lens designs were done by Zemax. Lumerical software tool were used for designing of the metalens. Silicon on Insulator (SOI) is chosen as the substrate of structure. Deep Reactive Ion and Wet Etching methods were applied to fabricate the integrated MOEMS actuator. Determining the optical architecture and components used for scanning are significant points of the study. A metalens and a coded mask, both of which can be produced by micro fabrication methods, were the optical payload of the actuator. For this purpose, a metalens consisting of nano-holes was designed as the first alternative. Secondly, a specific coded mask was designed and applied to the center of MOEMS structure for obtaining the spatial light modulation.

To obtain the desired displacement for subpixel scanning, the excitation voltage of the thermal chevron actuator is 12V, which is %8- %27 of the bulk piezo ceramic actuator counter parts in literature. The best performance of the excitation voltage 10.2V was achieved with a thermal and electro-magnetic hybrid Micro-Opto-Electro-Mechanical System (MOEMS) based scanner by means of additional Lorentz force caused by magnetic field. Core size of MOEMS actuator is 19 mm, which is %10-%38 of macro actuator equivalents.

Keywords: Micro Scanning, Adaptive Optics, Resolution Enhancement, Infrared Image, Coded Mask, Compressive Sensing, Electromagnetic and Thermal Actuators, Integrated Optics, Metalens, MOEMS

ÖZ

GÖRÜNTÜ ÇÖZÜNÜRLÜĞÜNÜN ARTTIRILMASI AMACIYLA MİKRO TARAMA AYNA VE LENS GELİŞTİRİLMESİ

Sözak, Ahmet
Doktora, Mikro ve Nanoteknoloji
Tez Danışmanı: Doç. Dr. Kıvanç Azgın

Mayıs 2022, 156 sayfa

Görüntü çözünürlüğünün geliştirilmesi, uzun yıllardır optik araştırmaların ana ilgi alanlarından biri olmuştur. Bu kapsamda birçok farklı yöntem araştırılmıştır. Bu yöntemlerin bazıları sahada kullanım alanı bulurken, bazıları da laboratuvar gösterimi düzeyinde kalmıştır. 1980'den bu yana odak düzlemli dizi dedektörlerin piksel boyutunu azaltmak için çok sayıda yaklaşım olmuştur ve o zamandan beri birim alandaki piksel sayısı ve çözünürlük artırılmıştır. Bununla birlikte, odak düzlemi dizisinin piksel yapısının küçük piksel aralığının üretilmesindeki zorluk ve sınırlı doldurma faktörü, özellikle kızılötesi dalga boylarında bu yöntemin kritik sınırlamalarıdır. Çözünürlüğü artırmanın diğer yöntemi olan mikro tarama, sahada uygulanabilirliğini kanıtlamıştır. Çözünürlüğü artırmak için, lenslerin, aynaların, prizmaların ve kodlanmış maskelerin taranması gibi bu tekniğin birçok uygulama çeşidi vardır. Makro ve mikro eyleyiciler, farklı optik mimarilerde optik bileşenin taranması için kullanılır. Kızılötesi görüntüleme için geleneksel mikro tarama sistemleri, 50 mm'den 200 mm'ye kadar boyutlara sahiptir. Bunlar, optik sistemde geniş alana ihtiyaç duyar ve hacimli optik bileşenler ve eyleyiciler nedeniyle 45V aralığından 150V'a kadar yüksek güç ve uyarma voltajı tüketir. Ayrıca, kızılötesi görüntüleme için geleneksel mikro tarama sistemleri yüksek parça adetine sahiptir ve yer değiştirme amplifikasyonu için ayrı mekanizma parçalarının kullanılması gerekir.

Bu çalışmanın amacı, gerçek bir makro ölçekli kızılötesi optik sistemin stabilizasyonu ve çözünürlüğünün arttırılması için küçük boyutlu, büyük yer değiştirmeli ve düşük güç tüketimine sahip yeni bir Mikro-Opto-Elektro-Mekanik Sistem (MOEMS) geliştirmektir. Bu bağlamda, bu çalışma boyunca hem PTC CREO hem de ANSYS ile CAD modelleme ve parametrik çoklu fizik sonlu elemanlar analizi kullanılarak bir piezo elektrik, bir termal ve bir elektro-manyetik mikro tarama sistemi tasarlanmış ve optimize edilmiştir. Optik mimari, ışın izleme ve lens tasarımları Zemax ile yapılmıştır. Metalenslerin tasarımı için Lumerical yazılım aracı kullanılmıştır. Silicon on Insulator (SOI), yapının alt taşı olarak seçilmiştir. Entegre MOEMS eyleyiciyi imal etmek için Derin Reaktif İyon ve Islak Dağlama yöntemleri uygulandı. Tarama için kullanılan optik mimarinin ve bileşenlerin belirlenmesi çalışmanın önemli noktalarıdır. Eyleyicinin optik faydalı yükü, her ikisi de mikro fabrikasyon yöntemleriyle üretilebilen bir metalens ve bir kodlu maskedir. Bu amaçla ilk alternatif olarak nano-deliklerden oluşan bir metalens tasarlanmıştır. İkinci olarak, uzamsal ışık modülasyonunu elde etmek için MOEMS yapısının merkezine özel bir kodlanmış maske tasarlanmış ve uygulanmıştır.

Piksel altı tarama amacıyla istenen yer değiştirmeyi elde etmek için, termal chevron eyleyicinin uyarma voltajı 12V'dir ve bu, literatürdeki piezoseramik eyleyicilerin %8 ila %27'sidir. Eni iyi performans olan 10.2V uyarım gerilimi, manyetik alanın neden olduğu ek Lorentz kuvveti sayesinde termal ve elektromanyetik hibrit Mikro-Opto-Elektro-Mekanik Sistem (MOEMS) tabanlı tarayıcı ile elde edilmiştir. Geliştirilen MOEMS eyleyicinin çekirdek boyutu 19 mm olup, makro eyleyici muadillerinin %10-%38'i kadardır.

Anahtar Kelimeler: Mikro Tarama, Adaptif Optik, Çözünürlük Geliştirme, Kızılötesi Görüntü, Kodlu Maske, Algılama, Elektromanyetik ve Termal Eyleyiciler, Entegre Optik, Metalens, MOEMS

This work is completely dedicated to my beloved wife and son without whose constant support this thesis paper was not possible. They always inspire me.

ACKNOWLEDGEMENTS

I would like to express my sincere gratitude to my supervisor Asst. Prof. Dr. Kıvanç Azgın for his supervisions, guidance and encouragements throughout this study.

I would also like to thank my friends and colleagues for their precious support and fellowship.

Finally, I would like to thank my wife, my son and my family for their love, support and patience over years.

TABLE OF CONTENTS

LIST OF TABLES

TABLES

LIST OF FIGURES

FIGURES

xxiv

CHAPTER 1

INTRODUCTION

Ever since the first ancient scientists started experimenting and trying to understand the secrets of life, universe and the world we live in, imaging has been one of the most important keys for exploring the unknown. Light which is the base of imaging was tried to be determined with specific questions like what light is, how it travels and how we can take advantage of its properties. Ancient Egyptians and Mesopotamians developed the first crude lenses [1]. From that point on, scientists from all major cultures in Asia, Middle East, Africa, and Europe started working on testing, hypothesizing, and testing instruments with a goal of understanding the behavior of light, its properties and the way it interacts with matter. For two thousand years, discoveries in many fields of science enabled engineers and inventors to develop the physical and diffractive optics named as classical optics and wave and quantum optics named as modern optics, respectively.

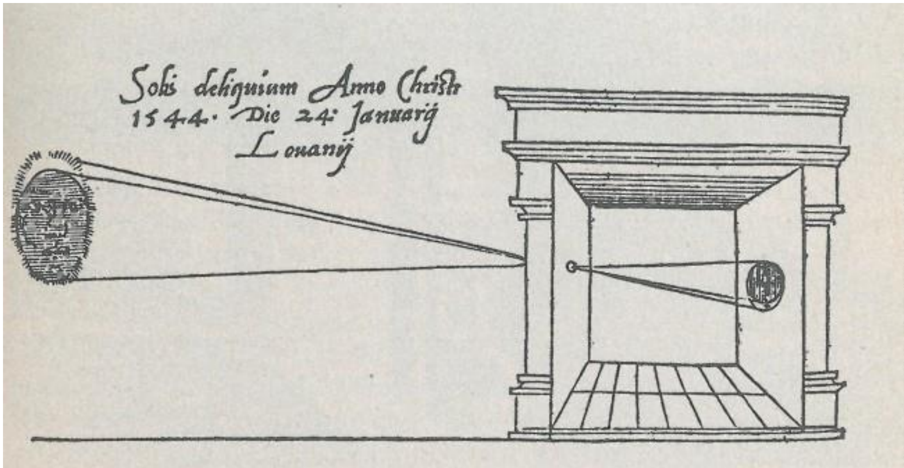

Figure 1.1. Camera Obscura [2]

The first camera, named the camera obscura, was invented in 11th Centuries. Camera obscura is the natural optical phenomenon. Light enters into a black box form a pin hole and the inverted image of scene is projected to the inner wall of the box. Joseph Nicéphore Niépce made the first permanent photograph of a camera image in 1825 by using a sliding wooden box camera.

The photographic film was invented by George Eastman, who started manufacturing paper film in 1885. The name of the first camera was Kodak. The first semiconductor image sensor was the charged-coupled device (CCD), invented by Willard S. Boyle and George E. Smith at Bell Labs in 1969. This invention was the first step of digital camera. The pixel resolution of the sensor was 100 x 100.

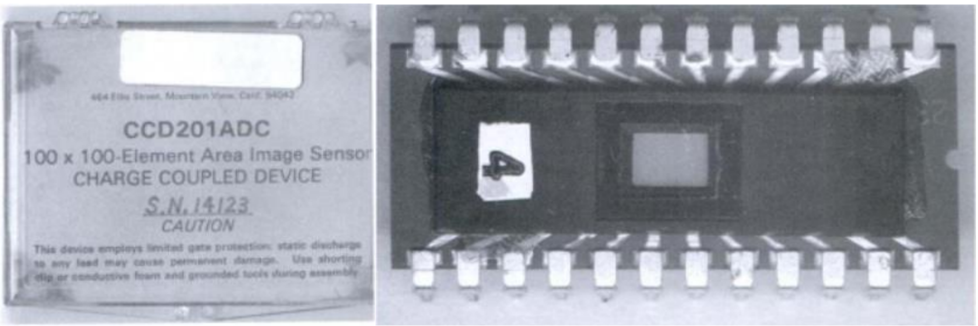

Figure 1.2. The 100 x 100 Fairchild CCD [3]

On the other hand, the development of infrared imaging technology began over 200 years. John Frederik William Herschel experimented the refraction of invisible rays by using a prism and a monochromator and discovered infrared radiation. Thermometers, thermocouples, and bolometers were the first infrared detection systems. After the invention of the transistor by John Bardeen and William Shockley in 1947, the modern InSb, HgCdTe, and Si photon based infrared detectors were started to be developed. In 1963, Texas Instruments became the first developer of forward-looking infrared system. The design and fabrication of complex focal plane arrays became possible with the revolution of molecular beam epitaxy and photolithographic processes at the semiconductor industry. There are three detector generations for civilian and military applications. Scanning systems with linear array detectors were the first generation. Multiplexing read out circuitry in the focal plane array capability was added in the second generation. Third generations include more pixel elements with superior on chip generation. [4]

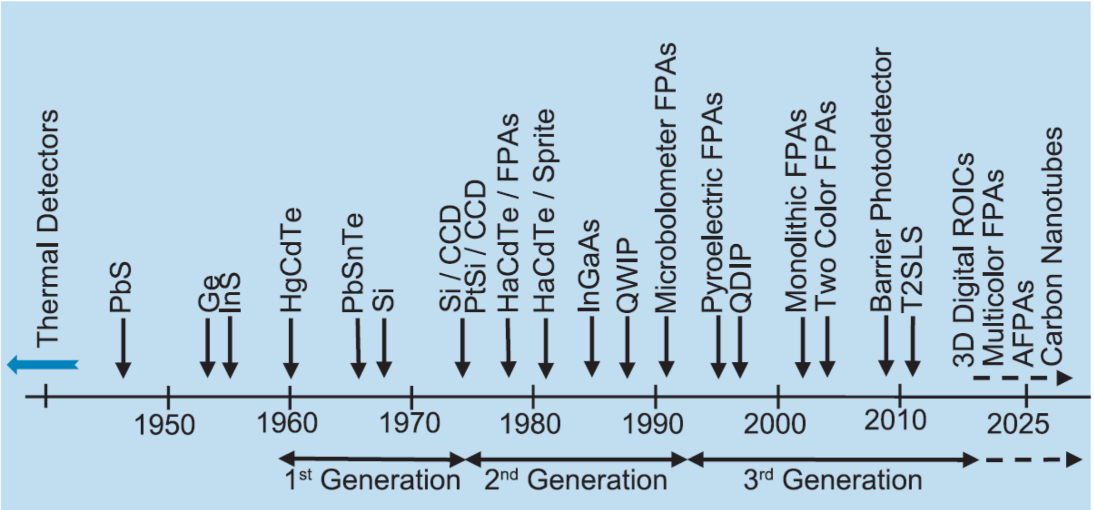

Figure 1.3. Detector IRFPA Roadmap [4]

The size of infrared focal plane arrays (IRFPAs) has been following the Moore's Law since 1980 with lag in size. Especially military projects have demanded to increase the number of pixel elements, but the size development of IRFPAs is below the Moore's curve. Therefore, the resolution enhancement of IRFPGAs with micro scanning is still a significant research topic. In this context, many different methods have been investigated [5]. While some of these methods found use in the field, some remained at the level of laboratory demonstration. The method of obtaining resolution enhancement with micro scanning [6] has proven its applicability in the field [7] , [8], [9]. There are many variants of application of this technique such as scanning of lenses, mirrors and coded mask for resolution enhancement [10].

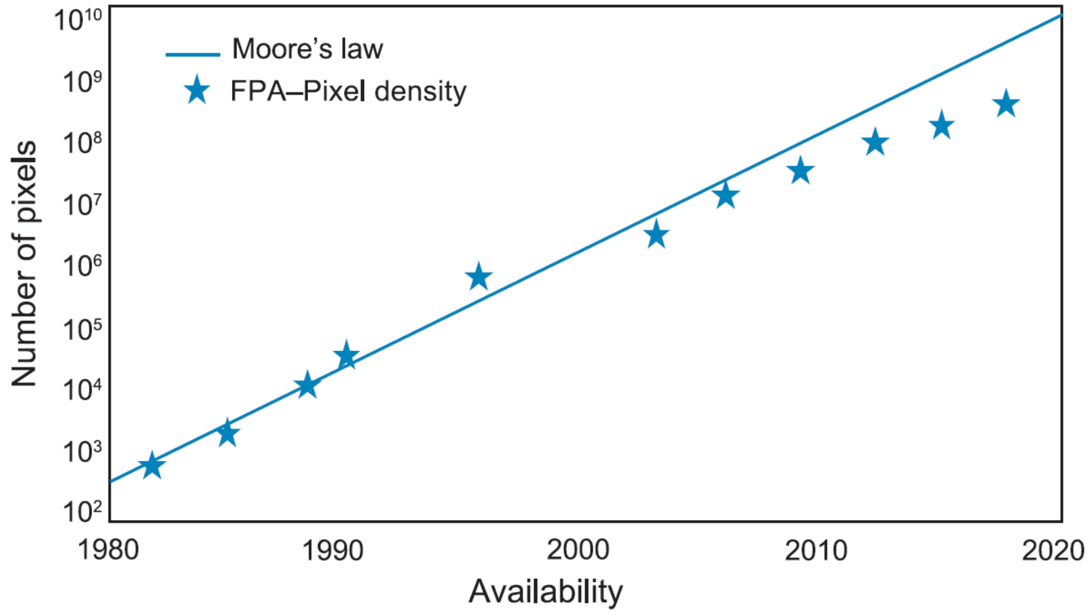

Figure 1.4. Pixel Density Graph w.r.t Moore's Law [4]

1.1. Microscanning Theory for Optical Systems

Infrared Staring Focal Plane Array (IRFPA) Detectors continue to develop because of their main advantages defined below.

- High sensitivity
- Small package
- Low power consumption
- Low integration time

However, Staring Focal Plane Array (FPA) Detectors have a main disadvantage that is resolution limitation caused by pixel size and number. This resolution limitation is caused by the array material properties, MEMS manufacturing technology and the physical limitations of optical systems.

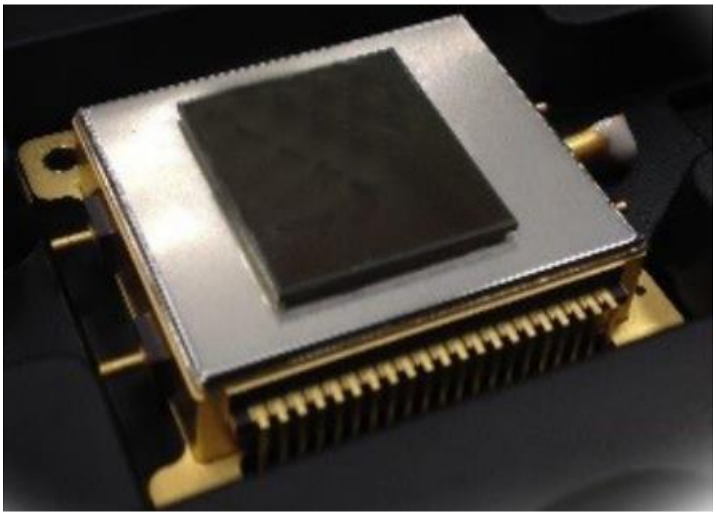

Figure 1.5. Focal Plane Array Package [11]

A Micro scanning is a method to improve the resolution of sensor images (CCD, IR etc.). The idea is the scanning image in sub pixel steps on the staring focal plane array and over sampling.

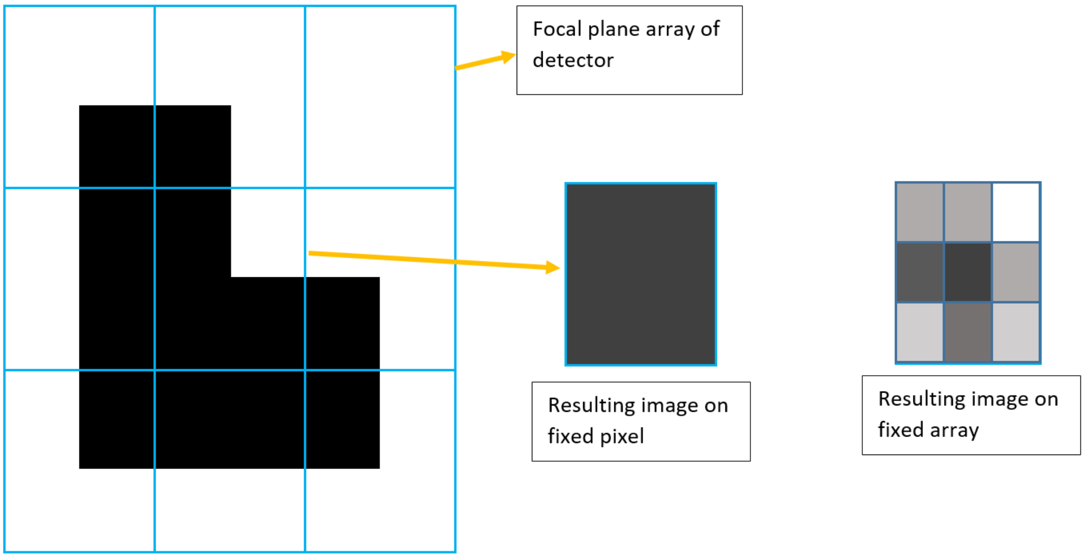

Figure 1.2. Pixel Size Effect

In an electro optical system, micro scanning can be applied by;

- Moving Detector FPA
  - Complicated

- Cryogenic limitations for cooled detector
- Tilting the Mirror
  - If you have in the system
- Prism Pair
  - High Chromatic Aberrations
- Moving Lens
  - Low chromatic aberrations
  - Low electric consumption
  - High speed and repeatability
  - Ease to implementation

From an optical system performance point of view, a moving lens is the most efficient way to enhance image resolution.

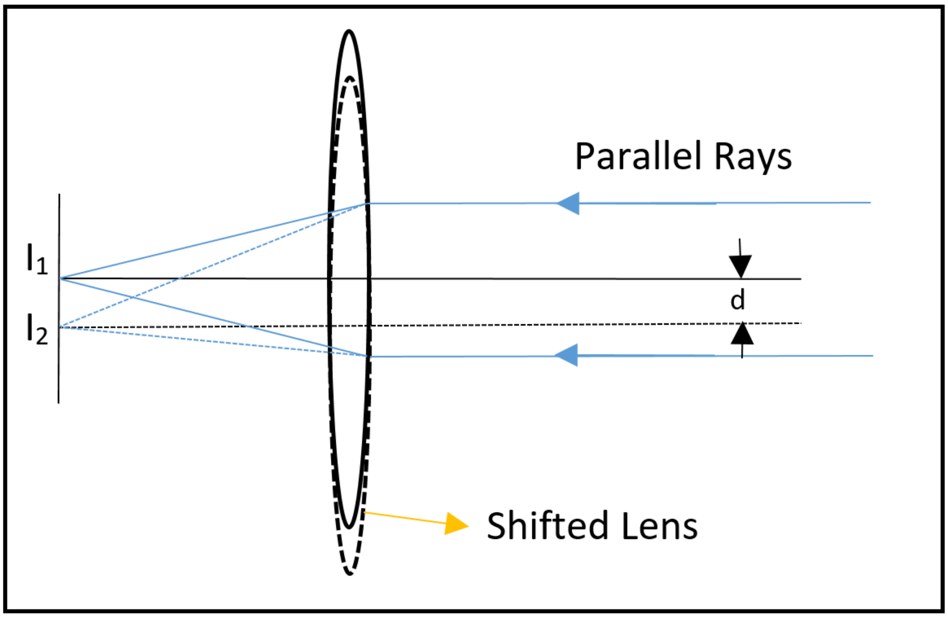

Figure 1.3. Lens Motion Effect

This research concentrates on the development of novel micro scanner and improvement of infrared image resolution of an electro optical system (EOS). For

Infrared electro optical systems, the parameters of micro scanning depend on mainly the pixel size and fill factor of detectors, as well as integration time, frame rate and other optical performance (Modulation Transfer Function (MTF), Noise Equivalent Temperature Difference (NETD) etc.) requirements.

1.2. Characterization of an Optical System

The main performance parameters for an infrared optical system are Pixel Size, Fill factor of detector, Integration time, Frame rate, Modulation Transfer Function (MTF), Minimum Resolvable Temperature Difference (MRTD) and Noise equivalent Temperature Difference (NETD). From that point of view, Pixel Pitch Size, Modulation Transfer Function (MTF), Integration Time and Minimum Resolvable Temperature Difference (MRTD) are used to design and evaluate the scanning systems. Current commercial cooled and uncooled infrared detectors have 17,15 µm and 10 µm pixel pitch (pixel size) that is the distance between the centers of the two adjacent pixels on the detector array. These sizes define the displacement of the lens scanned for super resolution with respect to optical design.

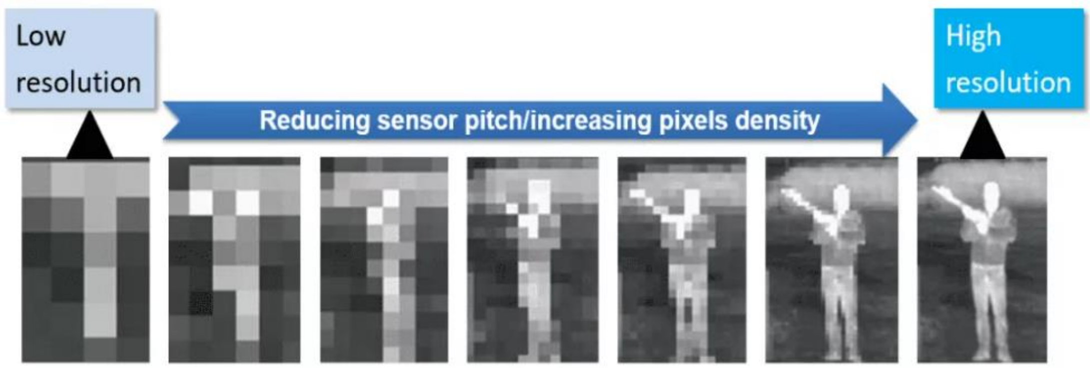

Figure 1.4. The Effect of pixel pitch on resolution [12]

Integration time directly related with frame rate is another parameter that defines acceleration, speed and control of scanning motion. Frame shifting time of scanning shall be lower than integration time and waiting time while capturing the single frame shall be higher than integration time.

1.2.1. Modulation Transfer Function (MTF)

Modulation Transfer Function (MTF), a way to incorporate resolution and contrast into a single specification, is a critical parameter showing performance enhancement.

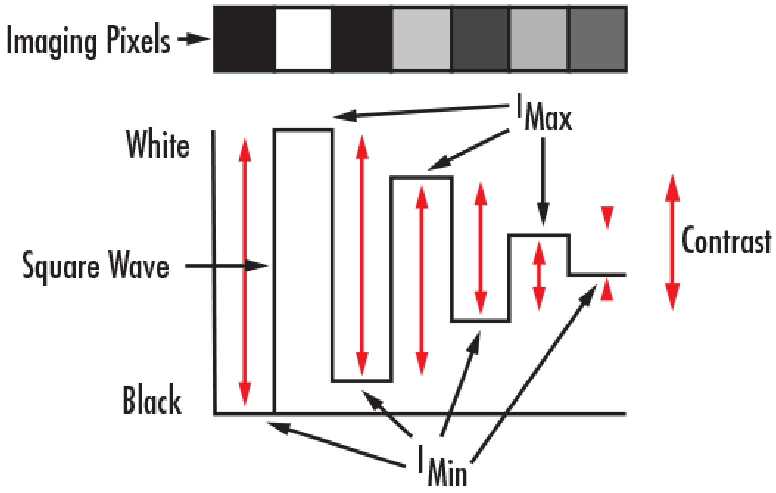

Figure 1.5. Contrast [13]

$$\%Contrast = \left[\frac{(l_{max} - l_{min})}{(l_{max} + l_{min})}\right] \times 100 \qquad (1)$$

Resolution is the ability of an optical system to distinguish an object. When the object is defined as line pair, resolution defines the minimum sized line pair that can be distinguished by an optical system. In general, the resolution of an optical system is tested by using an USAF target.

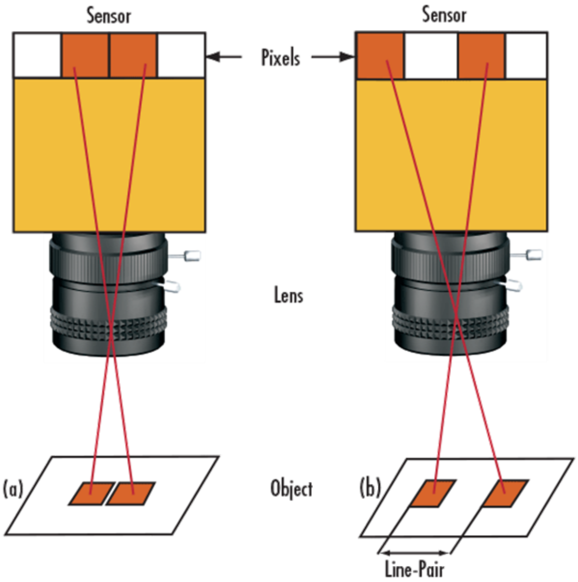

Figure 1.6. Resolution [13]

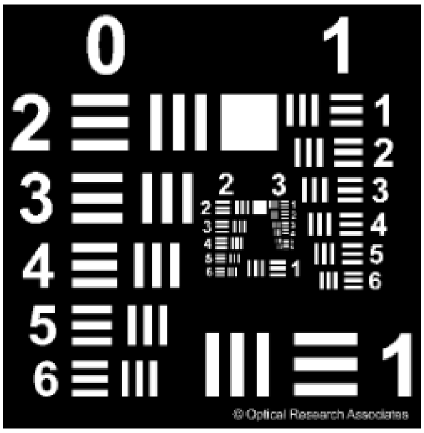

Figure 1.7. USAF Target [13]

The MTF of an optical system is a measurement of its ability to transfer contrast at a particular resolution from the object to the image. Contrast transfer is directly proportional with line spacing and MTF is a function of spatial resolution (ξ). In other words, as the line spacing decreases, contrast transfer decreases and becomes zero at the resolution limit (Cut-off Frequency (ξ_c)). The pixel pitch size (*PPS,mm)* of a detector is another critical parameter defining the spatial cut-off frequency (ξ_d, line pair per mm).

$$NA = n \cdot \sin\theta \tag{2}$$

$$\varphi = \cos^{-1}(\lambda \cdot \frac{\xi}{2NA}) \tag{3}$$

$$MTF = 2 \cdot \frac{(\varphi - \cos\varphi \cdot \sin\varphi)}{\pi} \tag{4}$$

$$\xi_c = \frac{1}{\lambda \cdot F\#} \tag{5}$$

$$F\# = \frac{f}{D} \tag{6}$$

$$\xi_d = \frac{1}{2 \cdot PPS} \tag{7}$$

Where *NA* is numerical aperture, the f-number (*F#*) is the ratio of the optical system's focal length (*f*, *mm*) to the diameter of the entrance pupil (*D*, *mm*), λ (mm) is the wavelength of the optical system, n is the index of refraction of the medium in which the lens is working, and θ is the maximal half-angle of the cone of light that can enter or exit the lens.

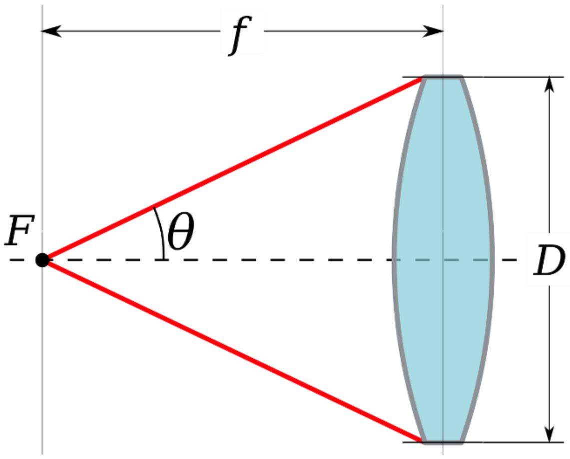

Figure 1.8. Numerical aperture of a thin lens

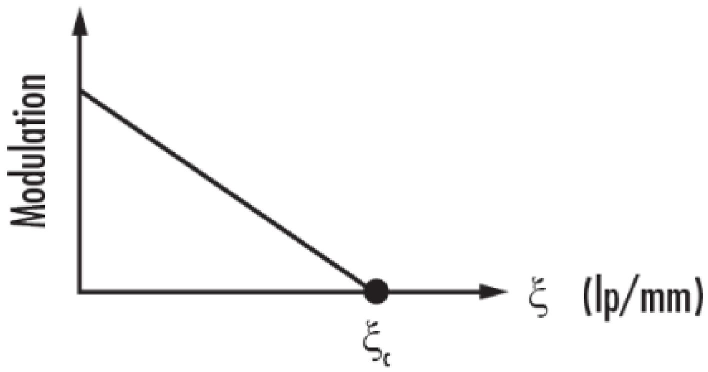

Figure 1.9 MTF Graph of an Aberration Free Optical System[13]

1.3. The Performance Effect of Resolution Enhancement

When the resolution of a system is enhanced with a micro scanning system, the contrast transfer can be obtained at higher spatial resolution and the system performance increases artificially. In theory, cutoff frequency of the system isn't changed but the super impose of the frames gives chance to enhance the resolution of the optical system.

In 1996, Fortin et al. reported the realization of a fast microscanning device for infrared focal plane arrays [14]. Figure 1.10 shows the effect of micro scanning on the optical system performance.

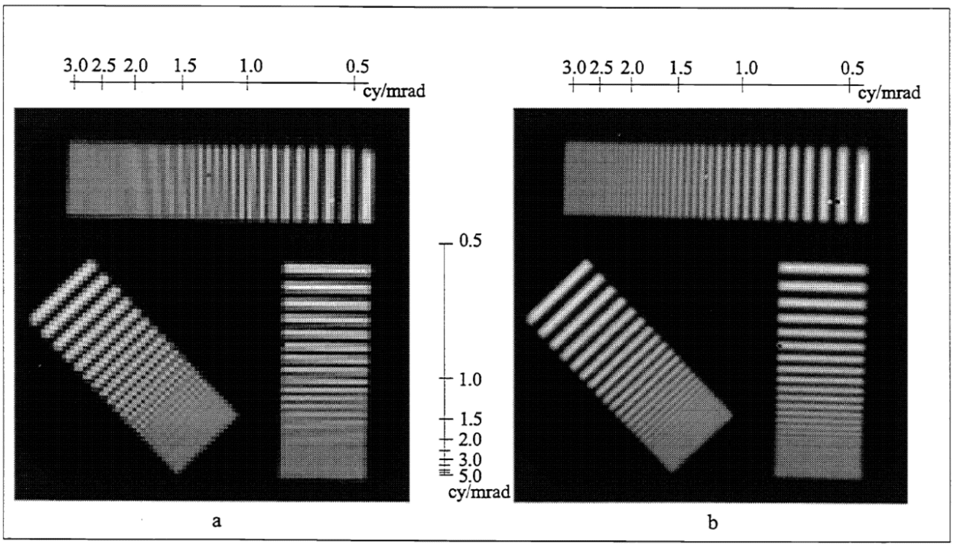

Figure 1.10 Images before and after 4x4 micro scanning [14]

1.4. Classification of Actuators

Actuators can be classified with respect to different performance metrics. The classification starts with the size of an actuator as Macro and MEMS actuators. The displacement magnitude, maximum force, precision, position accuracy and size are the main parameters for the optimization of actuators. In addition to these parameters, high frequency necessities discriminate the application type of actuators [15].

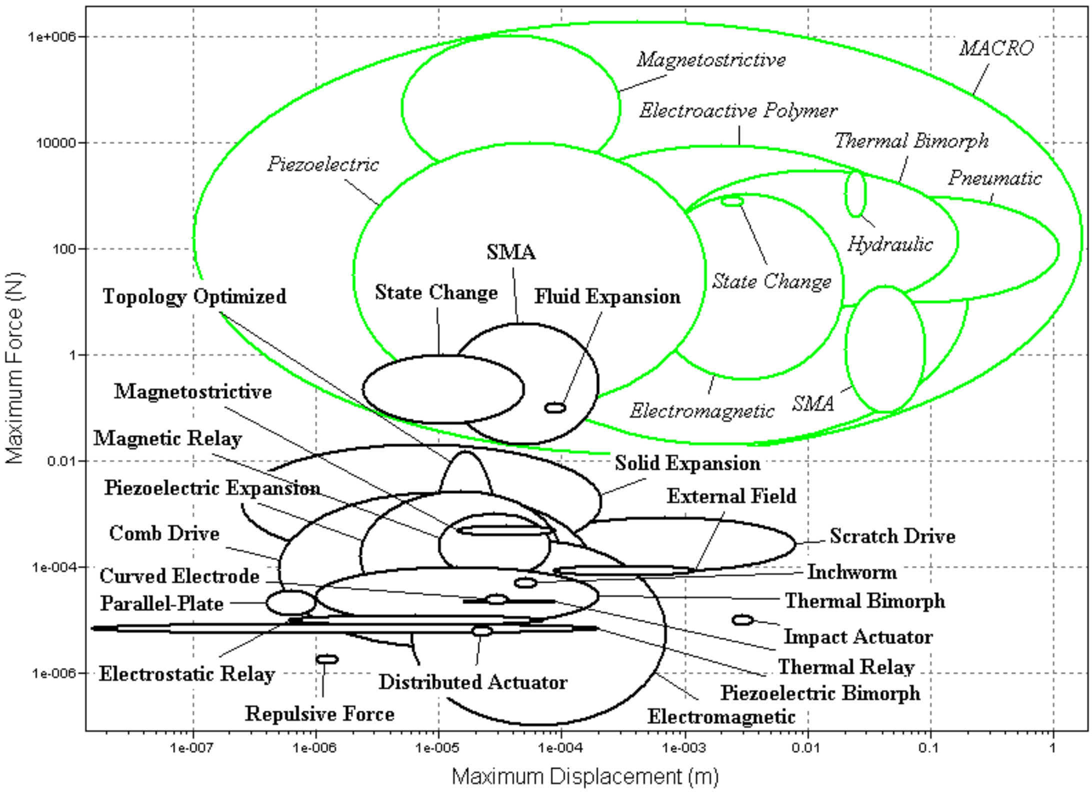

Figure 1.11 Force vs displacement for macro and MEMS actuators [15]

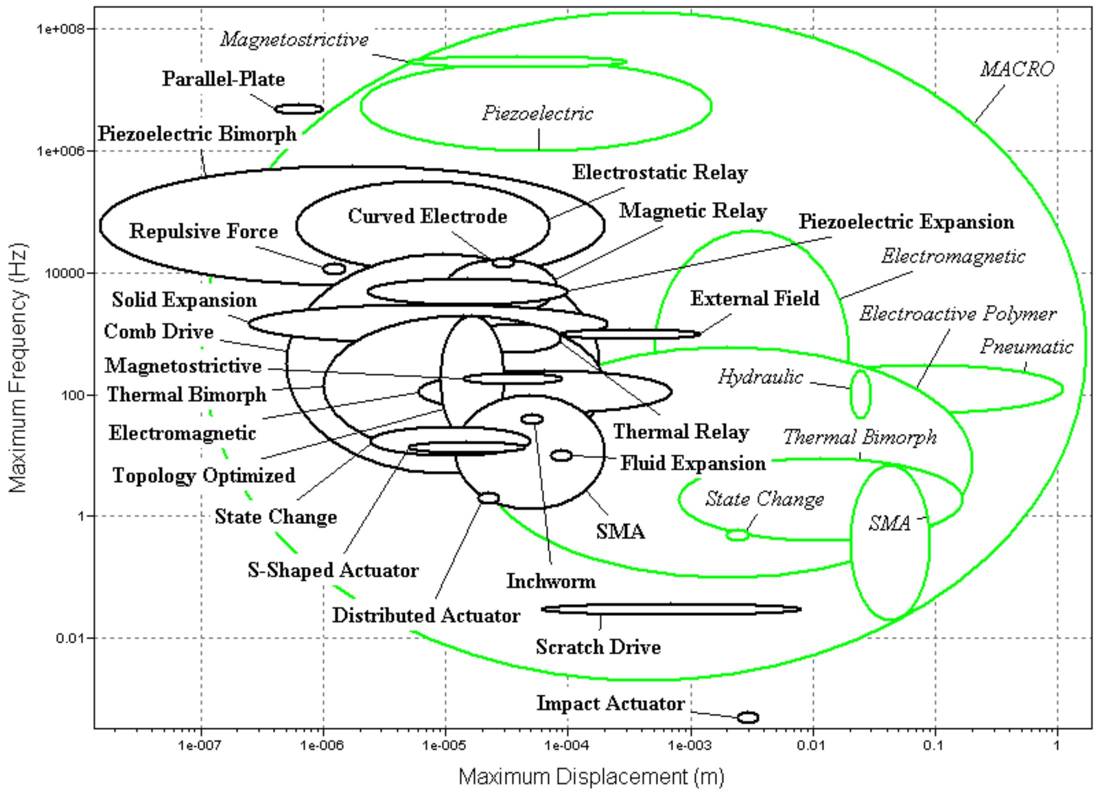

Figure 1.12 Displacement versus frequency for macro and MEMS actuators [15]

1.5. Characteristics of Macro Actuators

1.5.1. Piezoceramic Actuators

Bulk piezoceramic based actuators are used for nanopositining. The piezoelectric effect, a mechanical flexural guiding system and often an additional motion amplifier are utilized to obtain high precision positioning. Multi axis design gives the opportunity to operate up to 6 axes. In this way, super resolution and fine focusing of the optical system becomes possible. To improve the displacement and obtain multi axis motion, a different type of flexure and amplifier mechanisms are developed by using compliance mechanism design techniques.

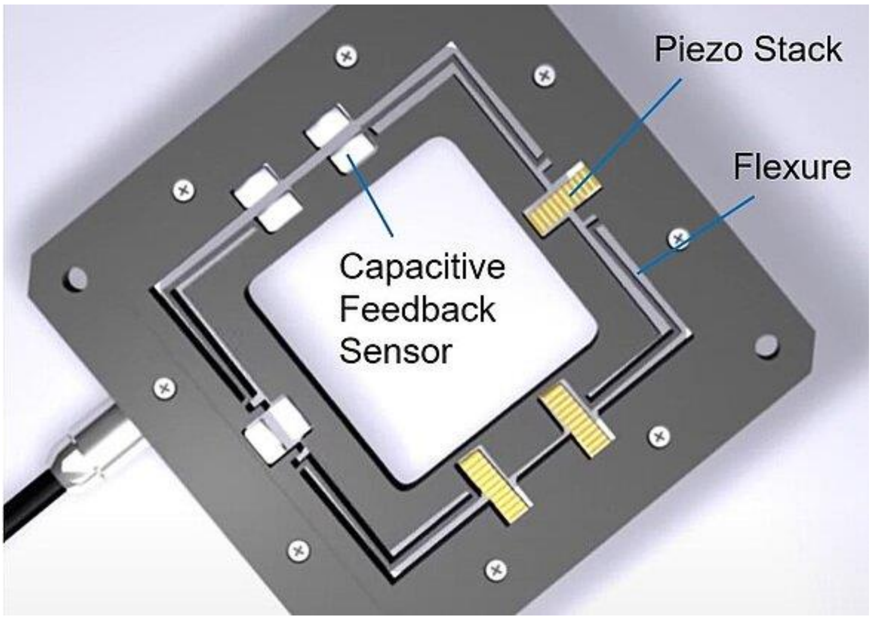

Figure 1.13 Basic design of a 3-axis piezo flexure stage (XY-Theta-Z) [16]

1.6. Magnetic Actuators

Magnetic actuators basically consist of a permanent magnet and a current-applied conductive structure. The permanent magnet supplies the required magnetic field at defined direction. One of the magnets or current applied structures constitutes the fixed part and the other the movable part. Different types of sensors, like Hall Effect sensors, optical encoders etc., are used to measure the amount of position precisely. Voice coil is the most common electromagnetic linear motor to drive the lens for optical image stabilization.

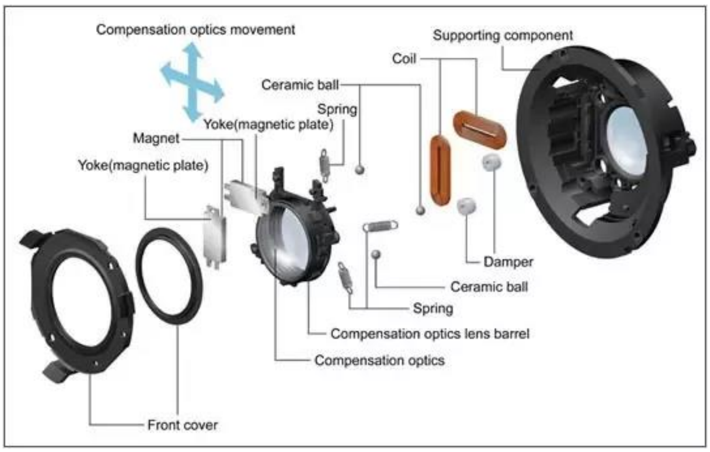

Figure 1.14 Magnetic Actuator Layout of Nikon D7200 Optical Image Stabilization [17]

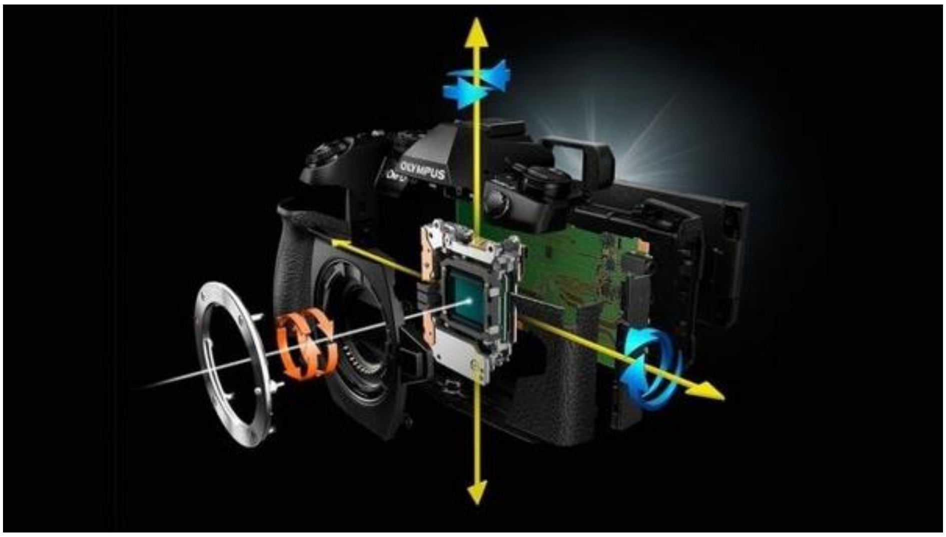

Figure 1.15 Magnetic Actuator Layout of In Body Image Stabilization [17]

1.7. Characteristics of MEMS Actuators

MEMS consists of mechanical microstructures, microsensors, micro actuators and microelectronics, all integrated onto the same semiconductor chip. MEMS has taken its place at the research laboratories like Kulite, Microsytems and Honeywell since 1950. In the 1990’s, MEMS components began appearing in numerous commercial products and applications. The greatest potential for MEMS devices lies in new applications within telecommunications, biomedical and process control areas.

MEMS has several distinct advantages as a manufacturing technology. In the first place, the interdisciplinary nature of MEMS technology and its micromachining techniques, as well as its diversity of applications has resulted in a unique range of devices and harmony across previously unrelated fields. The main MEMS based actuation techniques are electrostatic, thermal, piezoelectric and magnetic.

- Electrostatic MEMS actuators use the attraction between oppositely charged conductors. Electrostatic actuation is based on Coulomb's law which depicts the reciprocal force between two charges with a certain distance that generated between fixed and movable plates. The motion behavior is changed as displacement or resonance by the type of applied voltage DC or AC. [18]

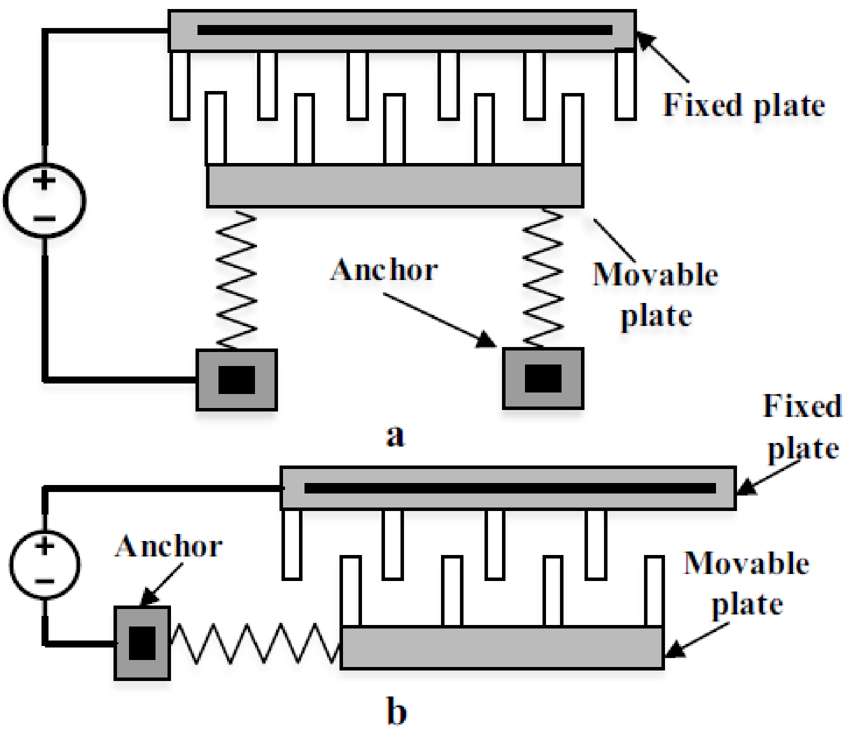

Figure 1.16 Electrostatic comb-drive configurations, a) longitudinal interdigitated comb actuator; b) transverse actuator [18][19][20]

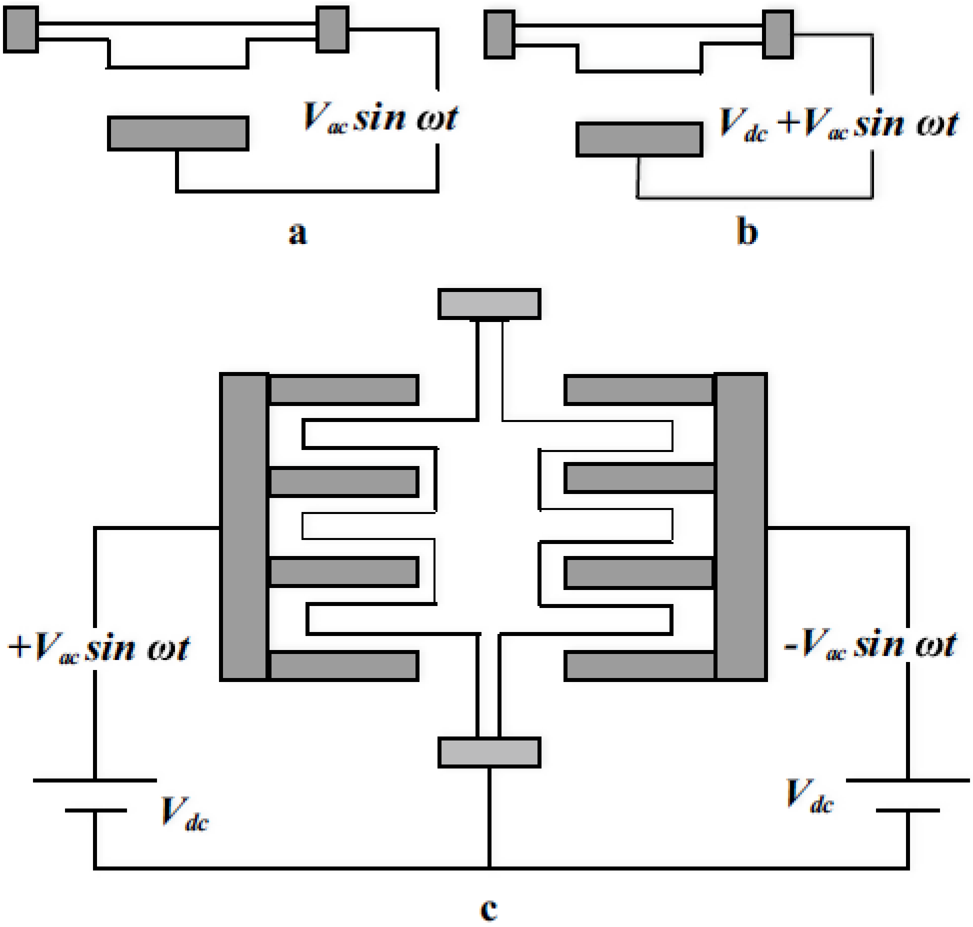

Figure 1.17 Comb driving resonator a) alternative voltage driving, b) alternating voltage with a dc bias, and c) push–pull driving [18]

- Thermal actuator techniques generally utilize the expansion arising from the change of temperature of the material under applied current. Using two materials having different coefficient of thermal expansion is one method to obtain displacement by heating. The other method is to use geometrical buckling from the expansion of material.

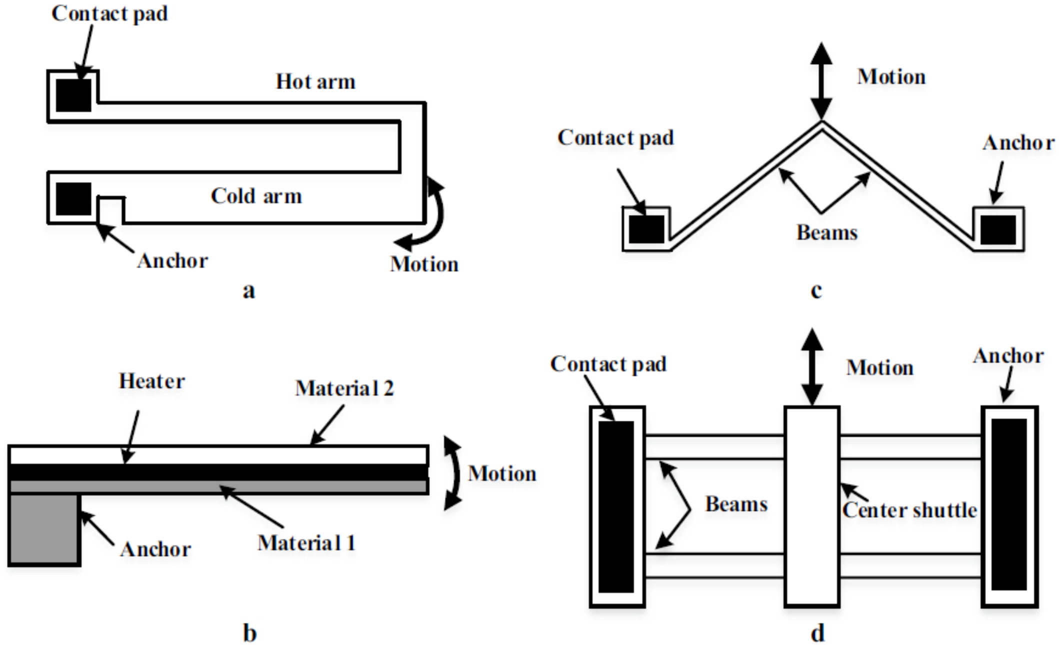

Figure 1.18 Electrothermal actuation a) hot and cold arm, b) bimorph actuator, c) and d) buckling actuators (V-Beam Actuator and shuttle beams) [18][22]

- Electromagnetic actuation uses the electromagnetic force which is also called Lorentz force surname of Dutch physicist Hendrik A. Lorentz 1895. Lorentz Force is defined as the force generated on a point charge as a result of the combined electric and magnetic forces on the charge [24]. Magnetic actuators use interaction among various magnetic elements like permanent magnets, external magnetic fields, magnetic material, and current carrying conductor.

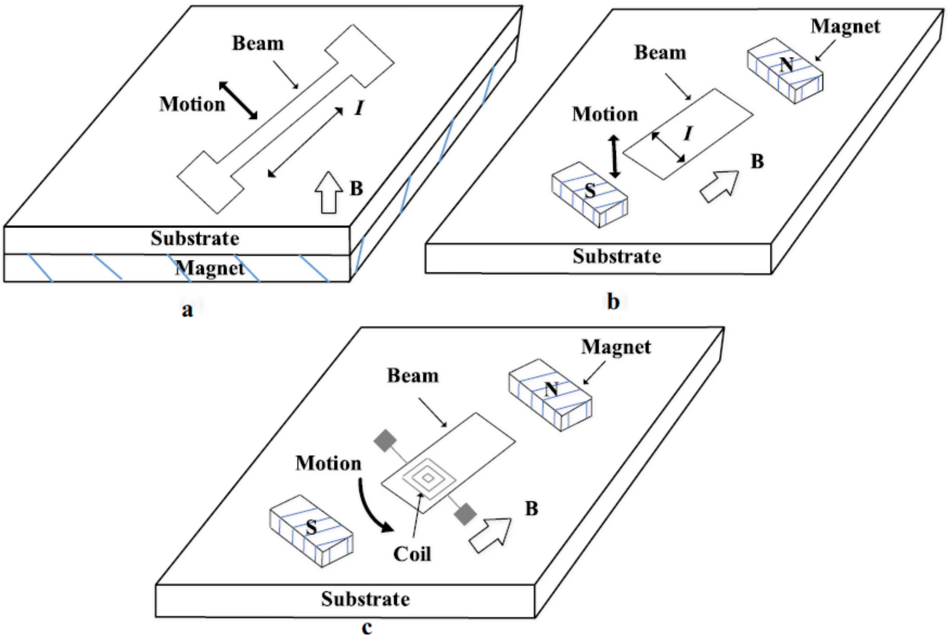

Figure 1.19 Electromagnetic actuation using Lorentz forces a) in-plane actuator, b) and c) out-of-plane actuator [18][23]

- Piezoelectric effect indicates the capability of a particular material to produce an electrical voltage in response to the applied mechanical stress. Piezo meaning is press or push and it is coming from the Greek language. Piezoelectricity was discovered by the Curie in 1880 [18]. A piezoelectric actuator converts an applied potential into a mechanical movement or strain based on the piezoelectric influence. Piezoelectric materials like quartz, zinc oxide, lead zirconate titanate (piezoelectric ceramic material PZT), and polyvinylidene difuoride (PVDF) are commonly used in sensor and actuator applications on a macro scale as well as in MEMS applications in recent years. The basic principle of the piezoelectric actuation method is based on using a thin piezoelectric layer that is deposited as a part of the MEMS beam between flexures. When a voltage is applied to the piezoelectric layer, the piezoelectric material expands according to the polarization of the applied voltage, which causes an axial bending across the length of the flexible beam.

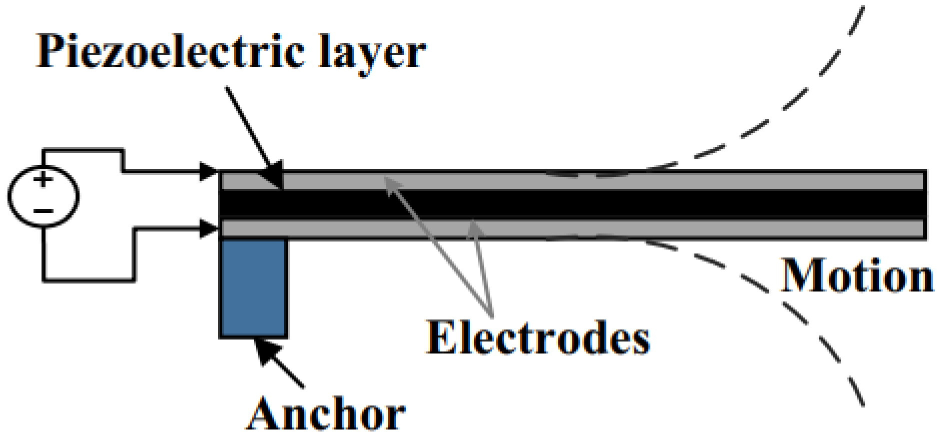

Figure 1.20 Schematic of the piezoelectric actuator [18][23]

All techniques have advantages and disadvantages when compared to one another.

Table 1.1. Characteristics of MEMS Actuators

Characteristics	Electrostatic	Thermal	Piezo	Magnetic
Low Power	✓	✗	✓	✗
Fast Switch	✓	—	✓	—
High Force	✗	✓	✓	✓
Large Travel	✗	✓	—	✓
Simple Fabrication	✓	✓	✗	✗
Low Voltage	✗	✓	—	✓
Robutness	—	✓	✓	✓

In 1993, integrations of mechanical, optical, and electrical micro systems were named as Micro-Opto-Electro-Mechanical Systems (MOEMS) by Dr. M. Edward Motamedi , a former Rockwell International innovator, at the SPIE Critical Reviews of Optical Science and Technology conference in San Diego officially [25]. The main difference between the optical MEMS and MOEMS is that the optical MEMS can include bulk optics but MOEMS is a pure micro technology combination of MEMS and micro-optics utilizing micro and nano fabrication methods. The main aims of the MOEMS are to steer, scan, focus, modulate the light with micro actuators and micro-optical structures. Micro mirrors, micro lenses, metalenses, diffraction gratings, micro interferometers, optical choppers and micro ring resonators are some of the micro optical structures.

A number of MOEMS display and imaging products and technology demonstrators have been developed for defense, aerospace, industrial, medical, and consumer markets in the form of wearable displays, projection displays, imaging devices, barcode readers, and infrared imaging cameras. Optical switches [27], digital micromirror device (DMD), lidar, retinal scanning displays and light focusing systems are the examples of MOEMS.

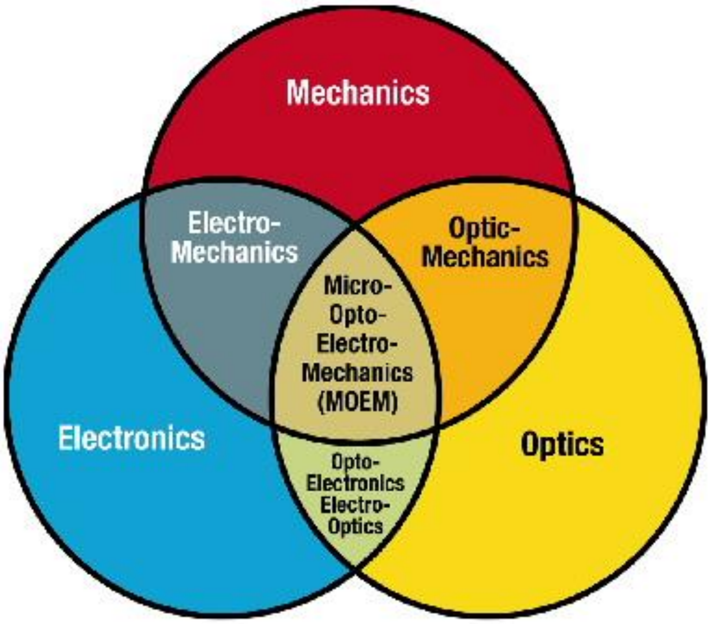

Figure 1.21 The interactions of micro-optics and micromechanics [26]

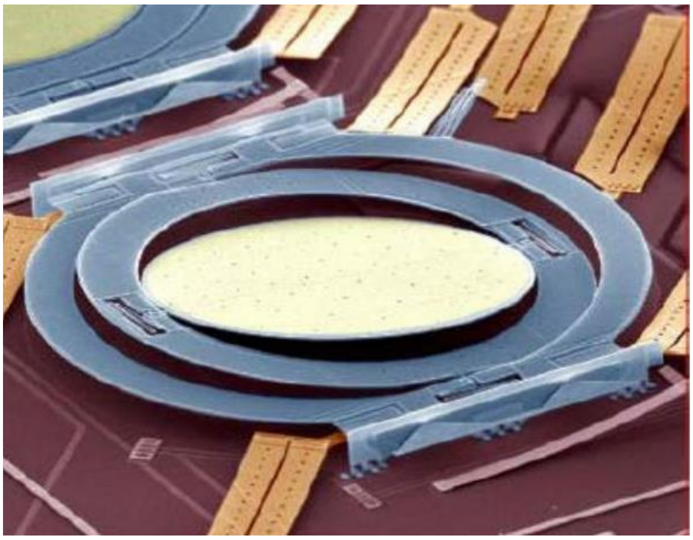

Figure 1.22 Micro-Mirror of MOEMS photonic switch [26]

In 2012, C.Y. Lin and J.C Chiou demonstrated a MEMS-based thermally actuated image stabilizer for cell phone camera. The proposed system has two axis X-Y stage and suspend an image sensor which is bonded to the actuator by using flip-chip bonding techniques. The electrical signals pass through the suspension beams. [28]

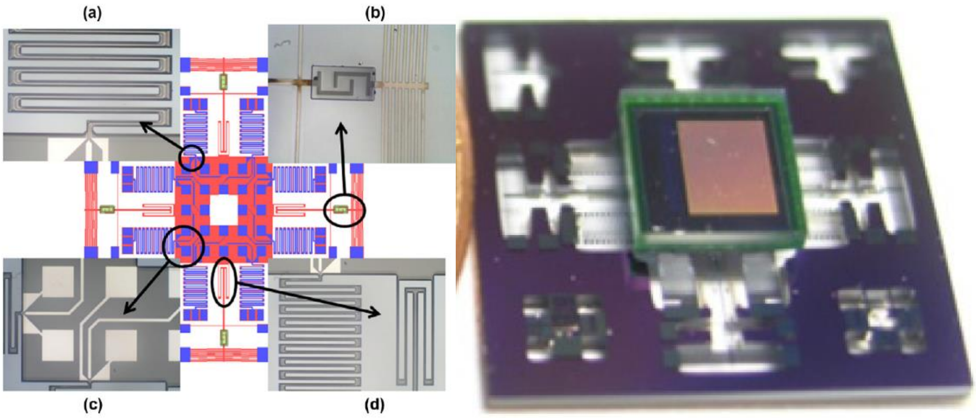

Figure 1.23 MEMS-based thermally actuated image stabilizer for cell phone camera [28]

In 2020, L. Zhou et al. reported a study entitled as a MEMS lens scanner based on serpentine electrothermal bimorph actuators for large axial tuning. This system is a good example for an optical MEMS. The system gives the focusing capability to the two-photon microscope by displacing the aspherical glass lens axially via a serpentine inverted-series-connected (ISC) electrothermal bimorph actuator [29].

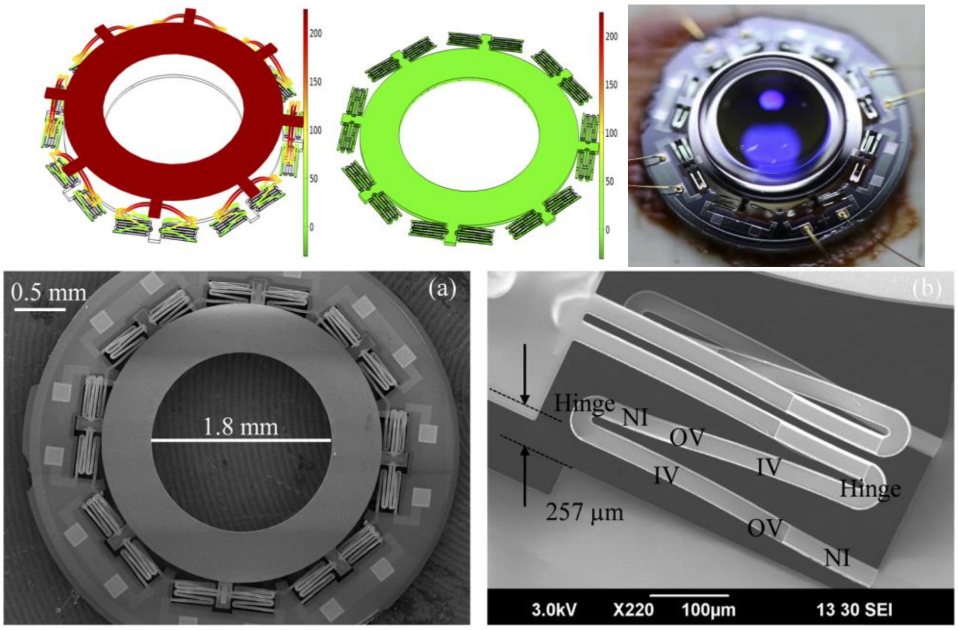

Figure 1.24 A MEMS lens scanner based on serpentine electrothermal bimorph actuators for large axial tuning [29]

Metalens or metasurfaces have significant potential advantages at the future MOEMS application because of the compatibility to microfabrication techniques. F. Capasso and N.Yu explained this potential of metalens in replacing the existing optical component in 2014 [30].

In 2017, the study of a dynamic metasurface lens based on MEMS technology was presented by S. Zhang et al [31]. The figure below indicates the proof-of-concept integration of metasurface-based flat lenses with 2D MEMS scanners. The optimization and test wavelength of metasurface is 4.6 µm. 2D angular rotation of a flat lens can be electrically controlled. The position of the focal spot varies several degrees.

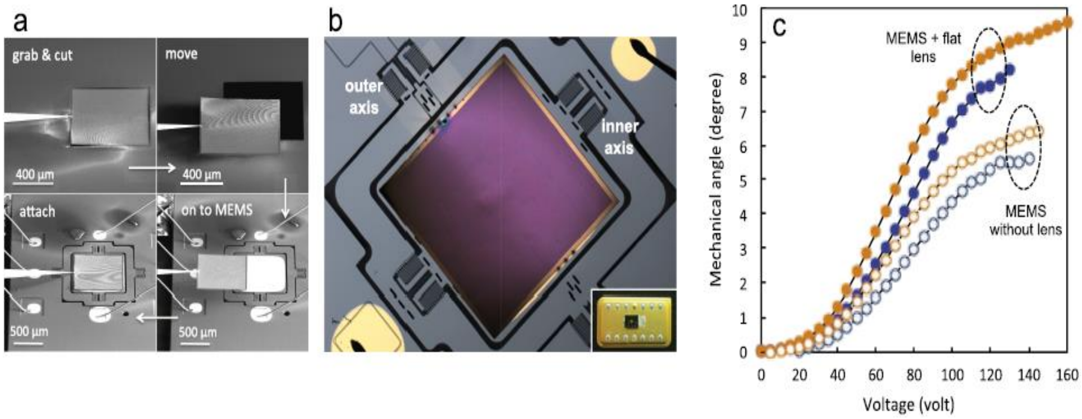

Figure 1.25 Integration of the flat reflective lens onto MEMS [31]

In 2018, E. Arbabi et al. published in Nature Communications about a MOEMS which is a MEMS integrated dielectric metasurfaces as a platform for tunable and reconfigurable optics [32]. This study demonstrates a tunable metasurface doublets actuated with electrostatic actuation to change the air gap and obtain focusing. The optimized test wavelength of this system is 910 nm. This concept has submillimeter aperture and consists of a stationary metasurface on a glass substrate, and a moving metasurface on a SiNx membrane.

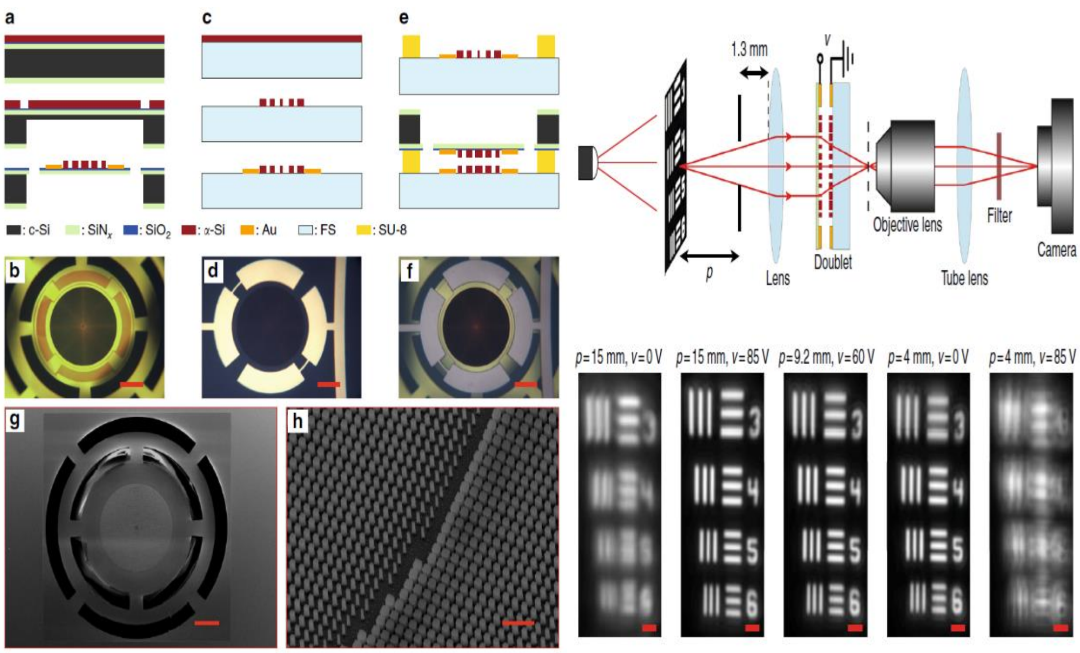

Figure 1.26 Fabrication steps, microscope and SEM images and the layout of test setup. [32]

In 2020, Han et al. reported a MEMS- actuated metasurface Alvarez Lens [33]. With lateral shifts of the Alvarez lens, metasurfaces, subwavelength-patterned diffractive optics, changes the optical power and by means of this, focusing can be obtained. Metasurfaces are utilized to reduce the device volume. Lateral shift is achieved by a MEMS electrostatic actuator. The operation wavelength of the prototype is 1550 nm. The 6.3 μm uniaxial displacement is obtained from actuator.

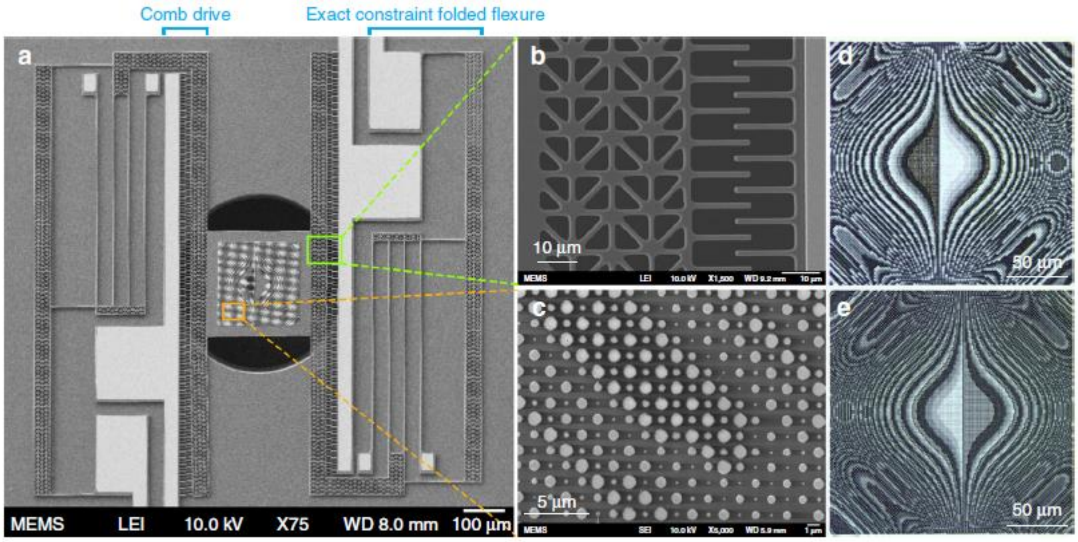

Figure 1.27 SEM images of MEMS actuated Alvarez lens [33].

1.8. Objective of This Study

When the literature was surveyed extensively, it is seen that conventional micro scanning systems for infrared imaging are bulky and consume high power due to bulky optical components. Various macro and micro actuators are used for the scanning of an optical component in different optical architectures. The main motivation of this study is to design a MOEMS system for stabilization and enhancement of the resolution of a real macro scale infrared optical system without increasing the size of system too much and with using novel optical payload. The MOEMS has unique potential in application of infrared imaging applications because the main substrates, semiconductor materials like silicon, germanium etc., are commonly used in MEMS micro-nano fabrication. Also, they are the main substrates of optical components of infrared imaging systems so that integration is possible. With this motivation, these unique properties of MOEMS systems defined above have directed this study to propose a MEMS based actuator design. However, the relatively lower output force of MEMS based systems compared to the conventional macro scale actuators is a obstacle that must be overcome.

In order to complete this study, following goals are achieved in the given order.

- Design of an optical layout, architecture and system specification for a scanning test system with a macro actuator:

  Since the aim of this study is to design a MOEMS based microscanner for real a macro scale system, the first layout is chosen as Long Wave Infrared (LWIR) imaging system with uncooled microbolometer detector to set up a test station and understand the microscanning behavior of an optical system. LWIR imaging system consists of 2 germanium lenses, one of them for scanning, and an uncooled microbolometer having 17 micrometers pixel pitch. A macro scale piezo actuator is designed for X-Y scanning of lens #2 and enhancing the image resolution from 640*480 to 1280*960 pixel resolution. Multi physics finite element analyzes is executed to obtain desired displacement performance. An open loop controller is obtained and decouple and the displacement performance of piezo ceramic actuator is tested at the optical autocollimator at submicron level precision. The parts are manufactured or supplied. The LWIR objective with a scanner is assembled and the scanning performance is tested with capturing the image of 4 bar on infrared collimator. The captured image is processed to superimpose and obtain high resolution images.

- Design of an optical MEMS scanner and a diffractive germanium lens instead of a macro scale piezo ceramic based micro scanner:

In order to achieve the displacement performance and miniaturization for MEMS applicability, a compact lens with diffractive surface is designed. The actuator type is defined as V shaped Chevron thermal actuator because of high force output and displacement. The substrate type of the MEMS actuator is decided as Silicon on Insulator (SOI) to achieve the structural and electrical requirements. The actuator is designed to have required force by optimizing the beam size and number, to have good decouple by applying flexures and dynamic performance with scanner lens. As a second iteration, an electrostatic displacement sensor is decided to add to measure the displacement of thermal actuators.

- Design of a proper fabrication flow for compact optical MEMS scanner fabrication:

  For the fabrication of device and handle layer, the Deep Reactive Ion Etching method is decided to use due to the high aspect ratio of features. Photolithography mask is utilized to impose the geometries. Electrical contact zones are coated with Au and fabricated with wet etching to achieve good conduction and bonding to wire or ribbon bond.

- To achieve further miniaturization, utilization of a coded mask spatial light modulator on the MEMS scanner:

  In order to achieve miniaturization, a coded mask is placed to the center of the MEMS actuator instead of the lens so that the optical element can be fabricated using same microfabrication methods with the MEMS actuator. This change gives a critical opportunity for miniaturization, using compressive sensing methods for micro scanning and simplification of the system. In this way, the system starts to become MOEMS. The optical architecture and layout of this objective is also changed to integrate the coded mask into the internal image plane of the objective. The wavelength of system 3-5 μm range where the proper SOI wafer has transmission. The MWIR imaging system consists of a cooled detector having 15 μm pixel pitch and a continuous zoom objective with an internal image plane. The fabrication technique DRIE is the same as the previous design with a minor difference in which an intermediate step is added to improve the actuator fabrication. The thermal actuation technique is not changed at this step.

- Design of a new optical architecture to improve the optical transmission of system and changing the coded mask with metalens on the MEMS scanner:
  A metalens, flat optics, is one of the most popular and significant studies at the current researches because it is light weight and fully compatible to microfabrication techniques. The layout of the optical system is changed a bit to integrate metalens.
- Design of a MOEMS based electromagnetic micro scanner with metalens:
  An electromagnetic actuator is designed and placed instead of a thermal actuator and the performance is evaluated with multi physics finite element analyses in terms of the displacement and voltage requirement. A permanent magnet is placed below and above to obtain a magnetic field.
- Design of a MOEMS based thermal and electromagnetic hybrid micro scanner with a coded mask and/or metalens:
  In order to combine the best properties of both actuation techniques and to achieve the improvement of displacement with the reduction of excitation voltage, the Lorentz force on the thermal actuator is analyzed for a defined magnetic field which can be obtained with permanent magnets. The permanent magnets were placed on the probe station and the displacement test was applied.
- The performance tests of the aforementioned approaches:
  The excitation of the actuator is done by power supply from contacts and the displacement of actuator is monitored by a microscope camera and the displacement is calculated from pixel size of microscope camera.

During this study, several actuation techniques, optical layouts and scanning techniques are tried and at the end of this study a high performance thermal and electro-magnetic hybrid MOEMS micro scanner with integrated spatial light modulation and metalens for resolution enhancement of an infrared imaging system could be developed successfully. Hybrid MOEMS micro scanner with integrated spatial light modulation could be fabricated successfully. To obtain the desired displacement for subpixel scanning, the excitation voltage of a thermal chevron actuator is 12V which is from %8 to %27 of the bulk piezo ceramic actuator equivalents in literature. Best performance in terms of excitation voltage 10.2V has been achieved with thermal and electro-magnetic hybrid micro-opto-electro mechanical system (MOEMS) based scanning actuator by means of additional Lorentz force caused by magnetic field. A hybrid actuator achieves minimum %17 better displacement performance than a thermal actuator. The core size of this MOEMS actuator is 19mm %10-%38 of macro actuator equivalents.

Contributions of this thesis to the literature can be summarized as:

- A novel thermal and electro-magnetic hybrid MOEMS micro scanner with integrated spatial light modulation for resolution enhancement of an infrared imaging system is developed. Hybridization of electrothermal and electromagnetics actuation techniques improves the displacement performance of an actuator. In addition to this, using spatial light modulation with coded mask for resolution enhancement on a MEMS based actuator adds the literature a different approach.
- A novel thermal and electro-magnetic hybrid MOEMS micro scanner with metalens for resolution enhancement and stabilization of infrared imaging system is developed. There are some MOEMS metalens applications at visible (Red,Green,Blue) and near infrared wavelengths (910 nm,1550 nm) at transmission mode for focusing and imaging and at 4,6 µm wavelength at reflective mode for steering. This study utilizes the translational scanning of metalens to enhance the resolution of macro level MWIR camera image.

- A hybrid actuator is fabricated with coded mask for spatial light modulation succesfully. This process involves 9 advanced fabrication steps.
- Bi-telecentric metalens doublet is integrated to the internal image plane of conventional infrared optical system for scanning and stabilization. This optical layout is unique for this purpose. Metalens doublet is designed to obtain wide range wavelength as 3.6 - 4.8 μm range. In general, metalenses operating at single wavelength exist in literature.
- Optical transmission of silicon wafers at mid-wave infrared band depends on the resistivity. When the beams of actuators are coated with conductive material, resistivity does not become a concern for the power consumption of the system anymore. So, the wafer with higher resistivity can be used for the device layer of SOI wafer.

1.9. Outline of the Thesis

There is a total of 6 chapters in this thesis. The first chapter is the introduction to history of optics, theory of micro scanning, macro and micro actuator techniques, MEMS actuators and MOEMS and has a literature search about the MEMS based actuation techniques.

The second chapter starts with the optical layout and parameters of LWIR Objective with piezo ceramic microscanner. Later in the chapter material characteristics of piezo ceramic material is defined and modelled. A piezo actuator is designed and analyzed by using the multiphysics finite element analysis method. The displacement test of the actuator prototype is presented. Finally, the micro scanning of the LWIR objective is done by capturing and superimposing the images. The resolution improvement of LWIR objective is indicated with images and graphs.

The third chapter explains the design, analysis and performance of the MEMS based optical microscanner. Fabrication steps and the displacement test of the optical MEMS microscanner are presented. Test results and future improvements are evaluated in order to be taken account at the next design.

The fourth chapter describes the resolution enhancement theory with spatial light modulation, an alternative optical layout and also the design, analysis, fabrication and tests of a novel MOEMS based thermal micro scanner. The size and excitation voltage reduction and displacement improvements are indicated. Finally, the position control method is mentioned with a flow chart.

The fifth chapter explains the MOEMS based electromagnetic actuator design and alternative optical architecture with metalens for microscanning. The theories of an electromagnetic actuator and metalens is defined in detail. The structural design, analysis and optimization of a magnetic actuator is explained.

In the sixth chapter, the novel micro scanning system design by using the MOEMS based thermal chevron and electromagnetic hybrid actuator is explained. The displacement improvement and excitation voltage reduction in the hybrid method are explained with the test results. The dynamic behavior of the actuator is also tested at different frequencies like 2.5, 5, 7.5, 10 Hz.

The thesis is concluded with the summary of the PhD. Study in the seventh chapter. In this chapter, goals achieved and the future works that can be done in order to improve the performance of the hybrid MOEMS microscanner are given.

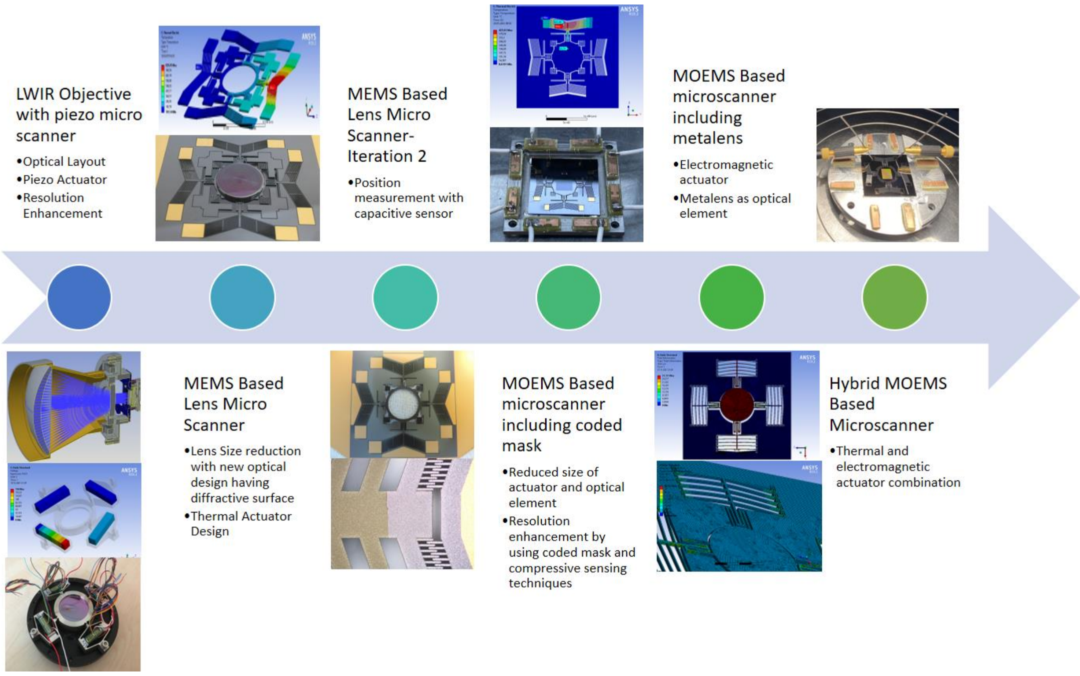

Figure 1.28 Chronology of Thesis Study

CHAPTER 2

MICRO SCANNING SYSTEM DESIGN BY USING PIEZO ELECTRIC ACTUATOR

In this chapter, the design of a piezo ceramic based macro actuator is explained. The main aim of this design is to obtain a reference micro scanning system in order to evaluate the parameters of micro scanning theory and compare the performance with a MEMS based micro scanning system.

2.1. System Specifications

The LWIR imaging system includes a 17 μm pixel pitch and 640*480 focal plane array format microbolometer detector. The f# number is 1.25 for single configuration. Effective focal length (EFL) of the system is 120 millimeters. The study first started with the determination of the necessary parameters for micro scanning. Actuator configuration was determined in line with the determined parameters and emerging requirements.

2.2. Optical Architecture

Thermal objective of this camera consists of two aspherical germanium lenses with anti-reflective coating. Mass of optical component and displacement requirement define the actuation technique.

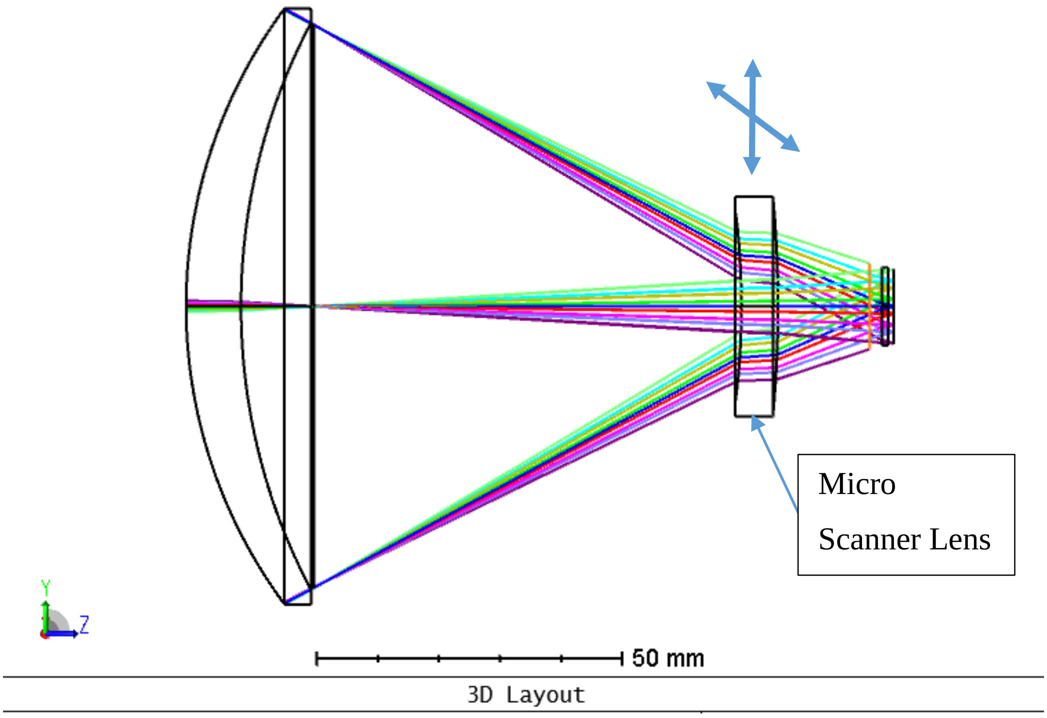

Figure 2.1 Optical Layout

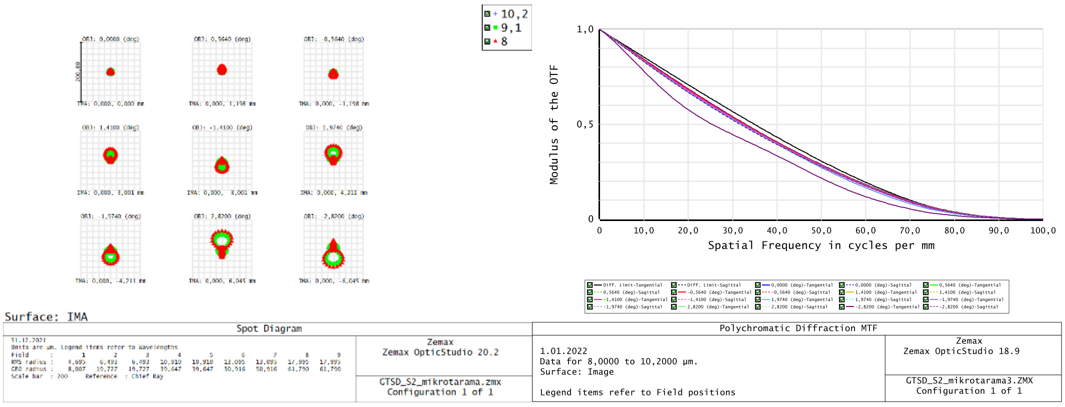

Figure 2.2 Spot Size and MTF Graph for different fields and wavelengths

2.3. Determination of Scanning Displacement Requirement

Decenter can be applied to the secondary lens by using coordinate brake and then the effect of that decenter on the FPA can be evaluated by using REAX merit function at design software Zemax. REAX shows the local real ray x-coordinate in lens units at the surface defined by **Surf** at the wavelength defined by **Wave**. There are two normalized field coordinates and two normalized pupil coordinates as defined Hx, Hy and Px, Py, respectively. Normalized pupil coordinates (Px, Py) do not change with the aperture size or position. For instance, a marginal ray at the top of pupil is defined as the normalized pupil coordinate (0.0, 1.0). A chief ray going through the center of pupil is defined as normalized pupil coordinate (0.0, 0.0). To trace the ray movement at X axis on whole image plane, Px was determined as 0, 0.5, 1.

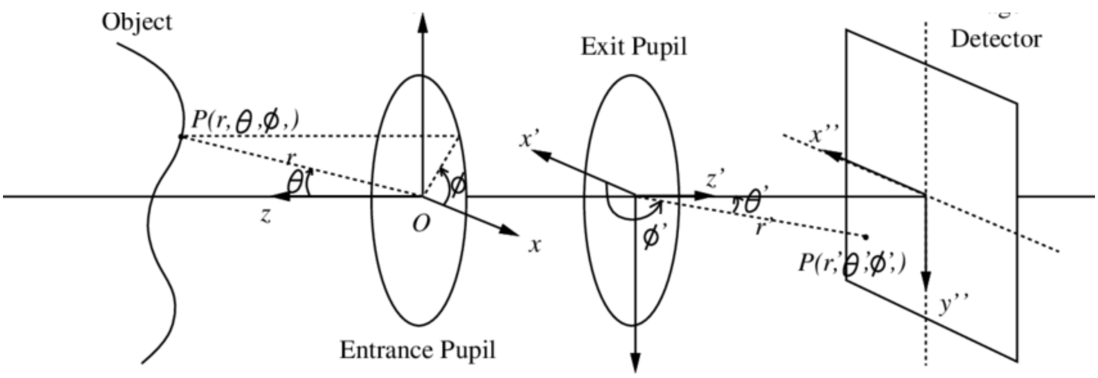

Figure 2.3 Normalized Pupil Coordinates[18]

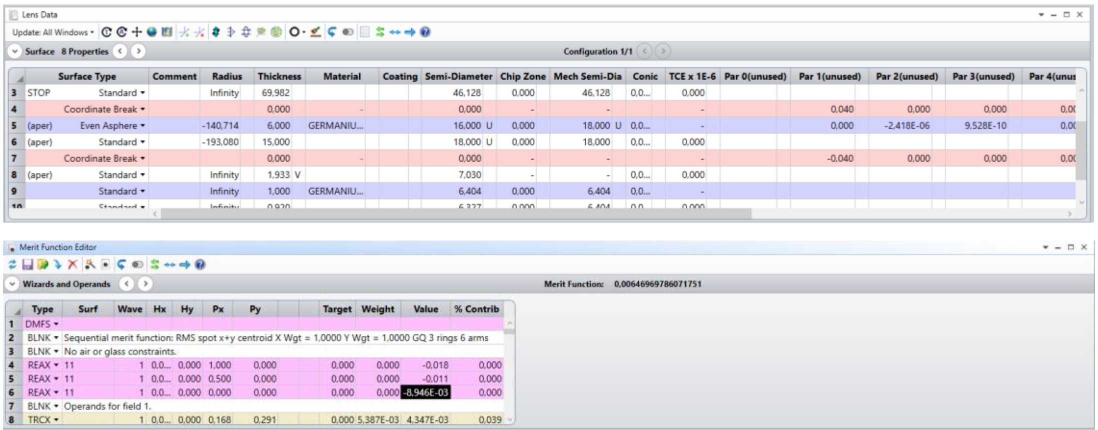

Figure 2.4 Ray trace analysis on image plane

The main requirement for resolution enhancement by using microscanning is to move the spot half of pixel sizes which should be approximately 9.5 µm for this application. To get this ray displacement, the displacement of second lens was calculated as approximately 40 µm at Zemax (See Figure 2.3). Spot size and optical performance change was checked after the decentering of the second lens 40 µm whether they all satisfy the optical performance. Figure 3.4 demonstrates that there is no significant change at the spot size and MTF magnitudes which means that micro scanning does not degrade the optical performance. Decoupled displacement for each axis is another requirement for the scanning actuator. The following table indicates the displacement variation of rays on FPA with respect to the wavelengths and pupil locations.

Table 2.1. *Ray displacement on FPA with respect to the wavelength*

Wavelength (mm)	*Marginal Ray Displacement (µm) (Px=1,Py=0)*	*Chief Ray Displacement (µm) (Px=0,Py=0)*	*Half Pupil Ray Displacement (µm) (Px=0.5,Py=0)*
8	0.012	0.0089	0.008
9.1	0.015	0.0089	0.0094
10.2	0.026	0.009	0.011

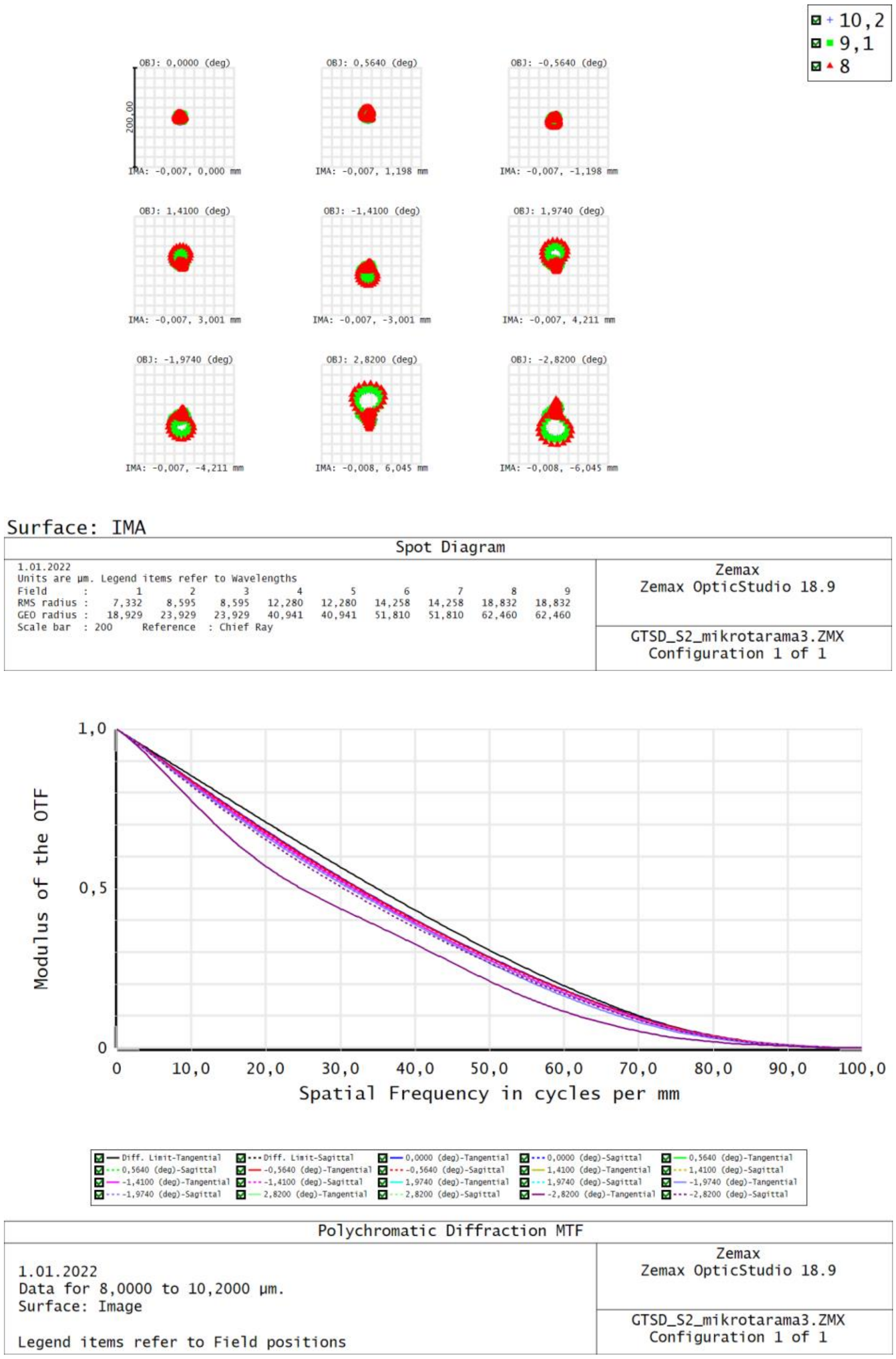

Figure 2.5 a) Spot size and b) MTF when 55 µm decentering lens at x coordinate axis

2.4. Piezo Electric Actuators

The piezo ceramic actuation is a common method to obtain micro and nano positioning. Main characteristic of piezo electric actuators is precision positioning under high load. The elongation can be measured directly with strain gage that gives the opportunity of position control. The main idea is coming from the material properties of piezo ceramics that is the strain under electric field. The desired displacement and force can be obtained with a displacement amplifier mechanism[35].

2.4.1. Material Properties of Common Piezo Ceramics and Piezoelectric Constitutive Relations

Piezo ceramic, used commonly in actuators, is the modified Lead Zirconate Titanate (PZT) having high domain mobility and ferro behavior, large piezo electric charge coefficient and moderate permittivity.

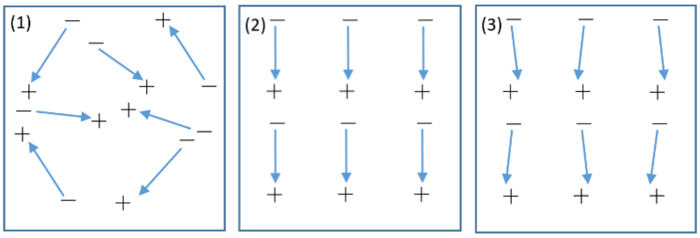

Figure 2.6 (1) Unpoled ferroelectric ceramic (2) during and (3) after poling piezoelectric ceramic

The basic relationships between the electrical and mechanical (elastic) properties can be represented as follow;

$$S = s^E \cdot T + d \cdot E \tag{7}$$

$$D = d \cdot T + \varepsilon^T \cdot E \tag{8}$$

where ε^T is Dielectric Permittivity for constant T, s^E = Elastic Coefficient (or constant E, D is Electric flux density, T is Mechanical Stress, E is Electric Field, S is Mechanical Strain.

The d term represents the full coupling between the mechanical and the electrical parts. If d term is dropped in the two equations, the uncoupled Hooke's law (mechanical) and Maxwell's equation (electrical) remain. d is usually referred to as the "piezoelectric coupling". In order to perform a piezoelectric analysis, structural elasticity (or elasticity coefficient matrix, unit: Pa or N/m^2) (s^E), piezoelectric coupling (d), and dielectric permittivity constant (ε) are required as material properties.

It is worth noting that piezoelectric material data is supplied in different formats, with ANSI/IEEE Std 176-1987 "Standard on Piezoelectricity" as the most used standard format. However, all industry standard material property data formats are not compatible with ANSYS, and they must be converted into an ANSYS compatible form.

Ansys Piezoelectric and MEMS ACT solves the conversion difficulties so that material properties of piezo ceramics can be defined to finite element analysis[37].

$$d = \begin{bmatrix} d_{11} & d_{21} & d_{31} \\ d_{21} & d_{22} & d_{23} \\ d_{31} & d_{32} & d_{33} \\ d_{41} & d_{42} & d_{43} \\ d_{51} & d_{52} & d_{53} \\ d_{61} & d_{62} & d_{63} \end{bmatrix} \tag{9}$$

$$s^E = \begin{bmatrix} s_{11} & & & & & \\ s_{21} & s_{22} & & & & \\ s_{31} & s_{31} & s_{33} & & & \\ s_{41} & s_{42} & s_{43} & s_{44} & & \\ s_{51} & s_{52} & s_{53} & s_{54} & s_{55} & \\ s_{61} & s_{62} & s_{63} & s_{64} & s_{65} & s_{66} \end{bmatrix} \tag{10}$$

$$\varepsilon = \begin{bmatrix} \varepsilon_{11} & \varepsilon_{12} & \varepsilon_{13} \\ \varepsilon_{21} & \varepsilon_{22} & \varepsilon_{23} \\ \varepsilon_{31} & \varepsilon_{32} & \varepsilon_{33} \end{bmatrix} \tag{11}$$

2.4.2. Design of Piezo Actuator

The main characteristic of piezo actuators is high position sensitivity under high load. High travel distance can be achieved by coupling the actuation with compliance mechanisms like amplification flexure structures owing to high load capacity. Compliant mechanisms are a common component of many technologies requiring ultra-high precision motion generation and displacement amplification, such as scanning probe microscopes, mechanisms for nano-imprint lithography, precision manufacturing, cell manipulation, micro grippers and optical steering mechanisms. Bi-directional motion capability is another advantage for applications. The elongation can be measured on piezo ceramic directly with strain gage.

After the evaluation of the optical design for micro scanning requirements and actuation techniques, the system design has been done as seen in figures below. The figure represents rays, optics, opto-mechanics, micro scanning mechanism and detector. As seen from the Figure 2.7, each actuator cell amplify the displacement at the vertical direction of piezo ceramic elongation direction by means of bridge-type compliance mechanism. Bridge-type mechanism is the combination of micro-flexures and micro-hinges arranged in such a way that it amplifies input displacement several times depending on the micro-flexure dimensional parameters, angle made with horizontal and micro-hinge types used. Extensive research has been carried out on bridge type displacement amplification mechanism by researchers all around the world. The mechanism has been designed with different geometric properties and types of flexure hinges used. Different geometries make it difficult to characterize the displacement analytically. In this researches, the finite element method is used for calculating displacement amplification ratio R_{amp} in detail. However, for understanding the theory, the analysis method based on kinematic theory is explained shortly in this section.

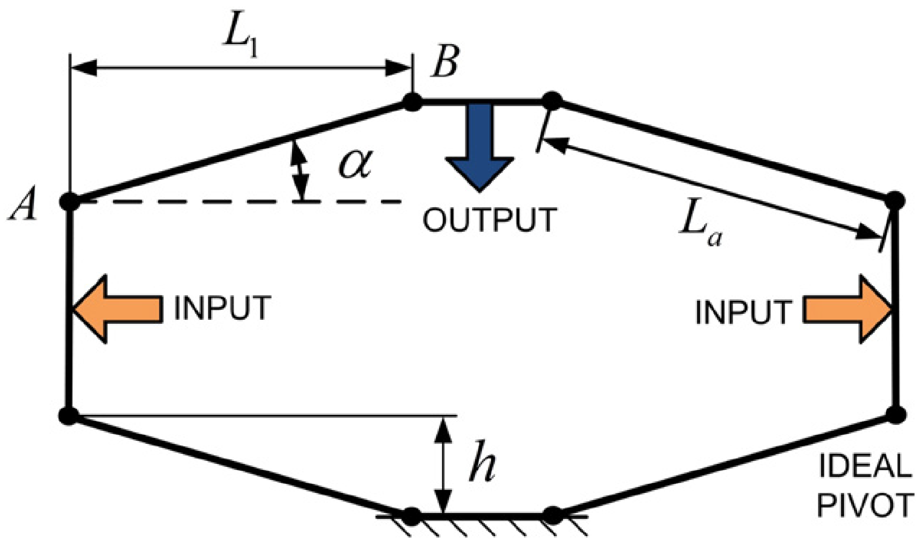

Figure 2.7 Schematic of bridge-type mechanism[42].

Because of the double symmetrical structure, only one arm of the mechanism is needed to be analyzed. Figure 2.8 shows the one quarter-model of the mechanism.

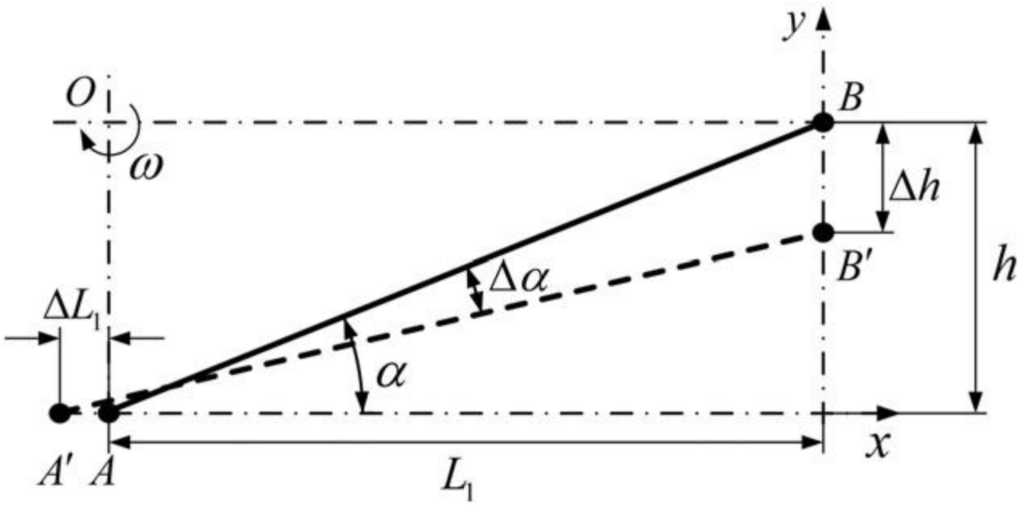

Figure 2.8 Quarter of ideal model of bridge-type mechanism[42].

The ideal displacement amplification ratio of bridge-type mechanism using geometric relations of the input displacement and output displacement was derived by Lobontiu and Garcia[42];

$$R_{amp} = \frac{\sqrt{{L_a}^2 \cdot \sin^2\alpha - 2L_a \cdot \Delta L_1 \cdot \cos\alpha - {\Delta L_1}^2} + L_a \cdot \sin\alpha}{\Delta L_1} \tag{12}$$

When the deformation is small, the following relationship can be obtained based on geometric relations:

$$\Delta\alpha \approx \frac{\Delta x}{L_a \cdot \sin\alpha} \tag{13}$$

where Δx represents the input displacement. Therefore, the equation can be written as follows:

$$R_{amp\_ideal} = \frac{h \cdot \left[ln\left(\frac{h}{\sqrt{h^2 + {L_1}^2}}\right) - ln\left(\sin\left(\arctan\left(\frac{h}{L_1}\right) - \frac{\Delta x}{h}\right)\right)\right]}{\Delta L_1} \tag{14}$$

The material of the lens is germanium and the weight of it is 52.38 gr. Stainless steel material has been used for holding the lens, piezo ceramic and wedged parts utilized to adjust preload of piezo ceramics. Also, a special epoxy based adhesive is applied to assemble the piezo ceramic to stainless steel holder through wedged parts from one side.

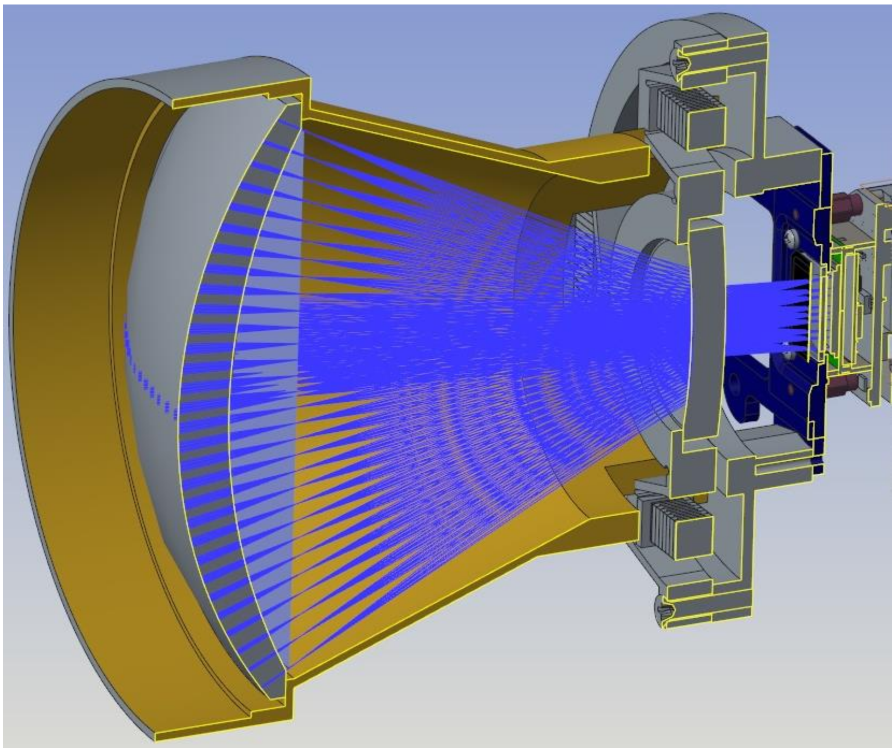

Figure 2.9 Optical system architecture

Also, a detailed model of a micro scanning mechanism and the dimensions of a single actuator can be seen at Figure 2.10 and 2.11, respectively. These dimensions are the final dimensions obtained as a result of the analysis specified in the following paragraphs.

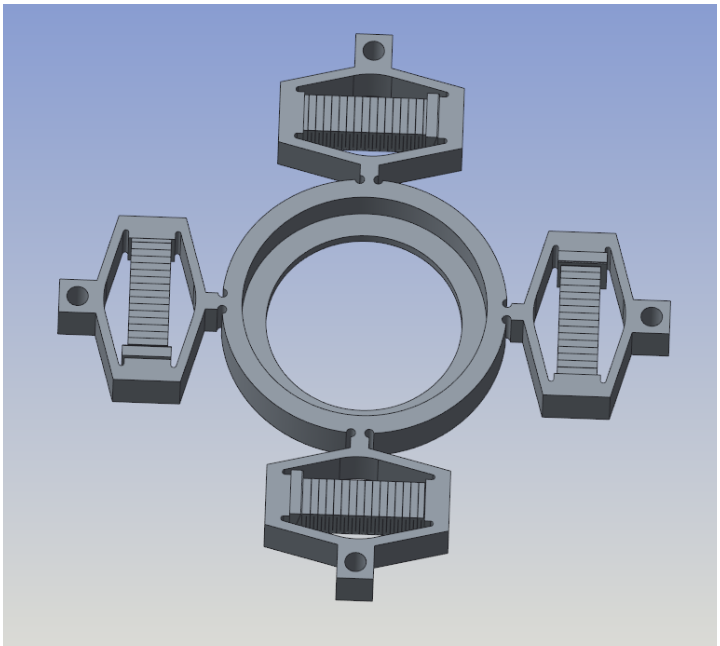

Figure 2.10 Piezo actuator for two axis-micro scanning

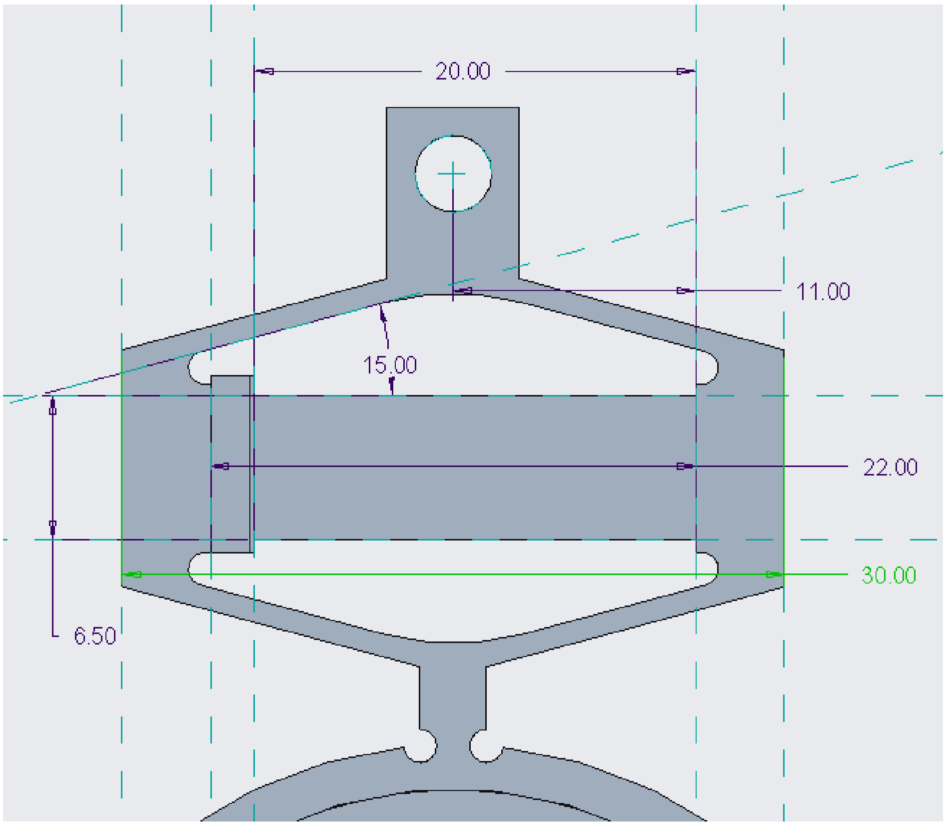

Figure 2.11 Dimensions of single piezo actuator

2.4.2.1. Piezo Electrical and Displacement Analysis of the System

With this design, the analysis and simulation of the micro scanning mechanism was performed by using the ANSYS multi physics software. Piezoelectric properties of material, especially anisotropic elasticity and permittivity, can be defined at Piezoelectric and MEMS ACT module of ANSYS.

The constitutive relations for linear piezoelectricity are given in Chapter 2.4.1.

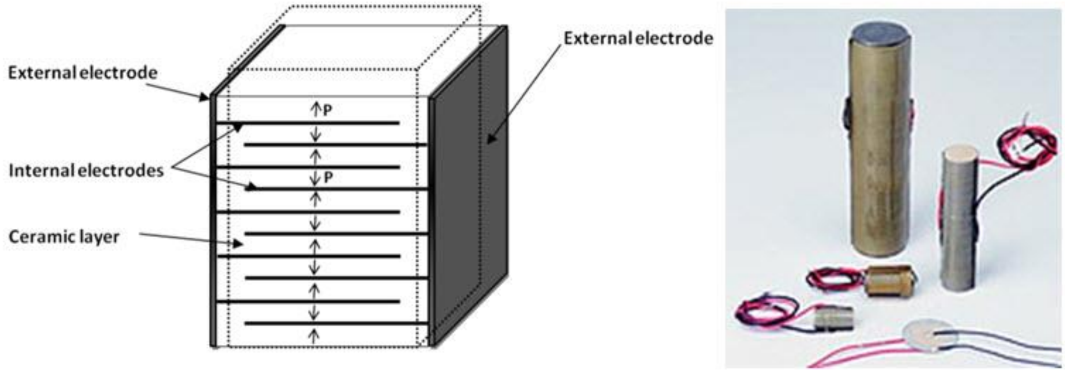

Figure 2.12 Electrode layout of multi stack piezo ceramic[36]

The main difficulties for that analysis and obtaining micro positioning are the characterization of piezoelectric material, multi stack behavior and optimization of flexure design.

$$V_M = n \cdot V_s \tag{15}$$

$$E_S = \frac{V_S}{th} \tag{16}$$

$$\varepsilon_s = E_s \cdot d \tag{17}$$

$$\Delta L_M = n \cdot E_s \cdot d = n \cdot \varepsilon_s \tag{18}$$

where V_M and V_s are the voltage of single and multi-layer stack piezo, E_S is the electric field of single layer, th is the single-layer thickness, d is the piezoelectric-strain constant, n is the number of stack, ΔL_M is the stroke of a multilayer stack piezo actuator.

The main purpose for designing a piezo actuator is to reduce size with changing the strain direction, amplify the extension and contraction displacement under load with flexure and satisfying the decenter value needed. The extension and contraction can be obtained by changing the electrical field direction between plus and minus value with required frequency. The maximum displacement for a commercially available THORLABS multilayer stack actuator comprised of PZS001 is about 17 μm at the maximum operating voltage of 150 VDC. For high frequency, harmonic excitation can be used as voltage of 0.5 V-rms, sinusoidal mode from 0 to 100 kHz. The thickness of each layer in the stack was calculated to be 0.109 mm since the overall length of the stack was known. Frequency is defined by the integration time of the detector. This change creates a push-pull motion on the lens or mirror. The first analysis results can be seen at Figure 2.14. The preload on piezo ceramic is a critical parameter effecting the elongation magnitude so while assembling the piezo ceramic to the bridge type mechanism, two wedge shape parts are used to adjust the preload of each piezo ceramic. The estimation method of preload is to measure the width of the bridge before and after assembling the wedge part and adjust the intrusion of the wedge part to obtain the required preload.

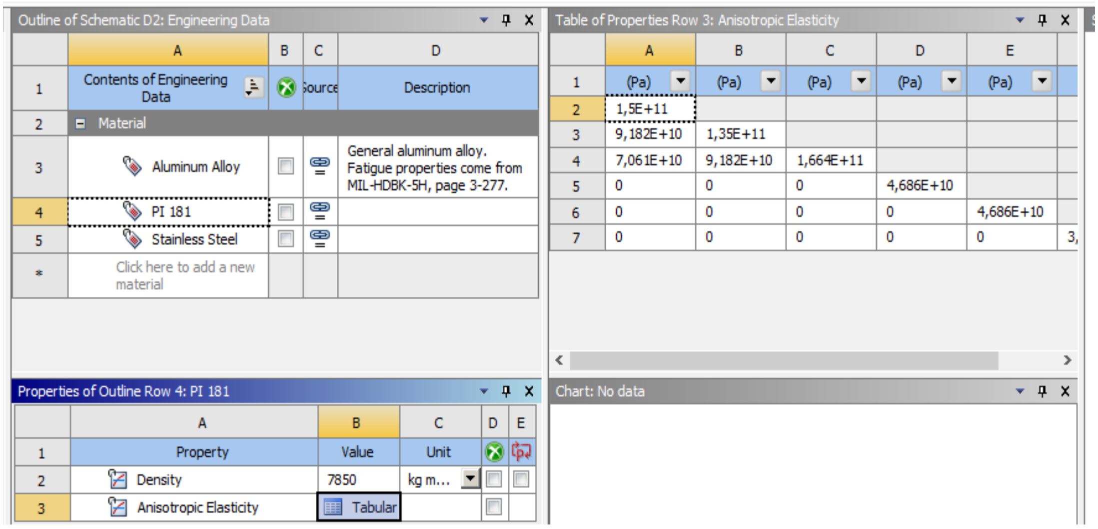

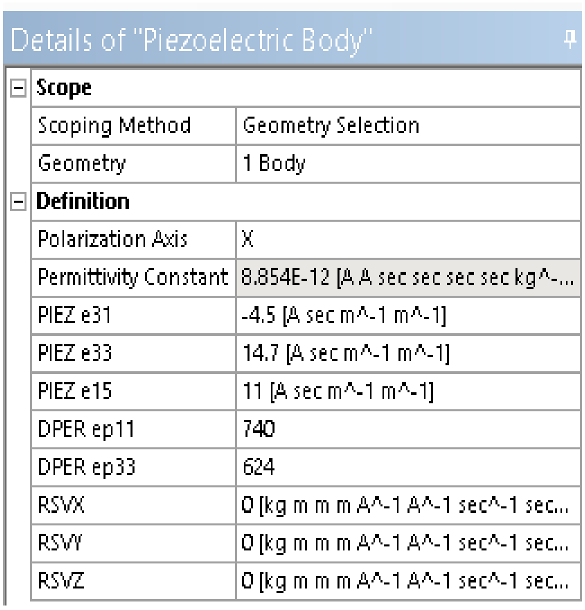
Details of "Piezoelectric Body"

Scope	
Scoping Method	Geometry Selection
Geometry	1 Body
Definition	
Polarization Axis	X
Permittivity Constant	8.854E-12 [A A sec sec sec sec kg^-...
PIEZ e31	-4.5 [A sec m^-1 m^-1]
PIEZ e33	14.7 [A sec m^-1 m^-1]
PIEZ e15	11 [A sec m^-1 m^-1]
DPER ep11	740
DPER ep33	624
RSVX	0 [kg m m m A^-1 A^-1 sec^-1 sec...
RSVY	0 [kg m m m A^-1 A^-1 sec^-1 sec...
RSVZ	0 [kg m m m A^-1 A^-1 sec^-1 sec...

Figure 2.13 Material Properties of PI 181 Piezo Ceramic

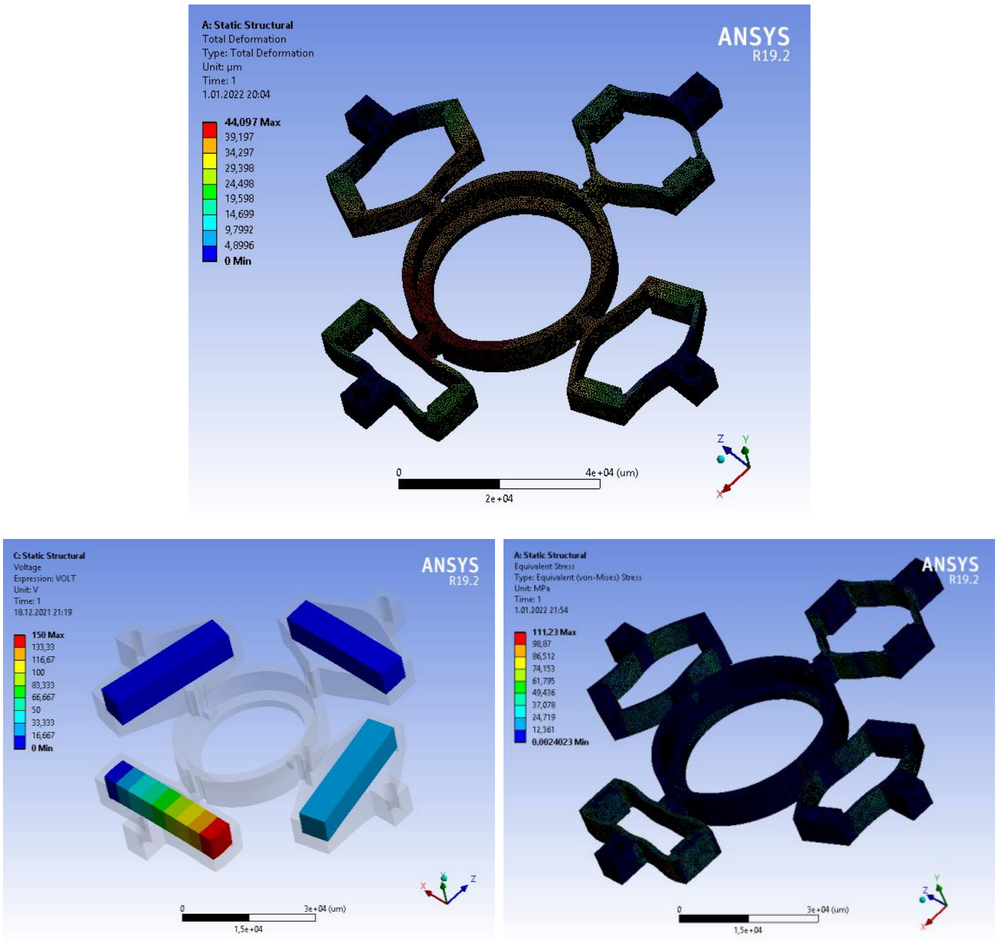

Figure 2.14 Push-Pull Displacement, Maximum Equivalent Stress and Applied voltage

2.4.2.2. The Prototyping and Testing of the Piezo Actuator

The parts were manufactured with respect to the technical drawings of the piezo actuator design and also the driver hardware was obtained from a supplier (see Figure 2.17). The displacements of lens were measured optically by using laser auto collimator. The measurement result is 44 µm at single axis which is quite close to design value 44.094 µm. This result also means that displacement amplification ratio R_{amp} of the bridge type compliance mechanism is 2.58 which is close to the analysis result. The reasons of the difference between analysis and measurement of R_{amp} are the assumptions at contact types of surfaces between parts, unpredictable adhesive behavior, the preload on piezo ceramics and material properties.

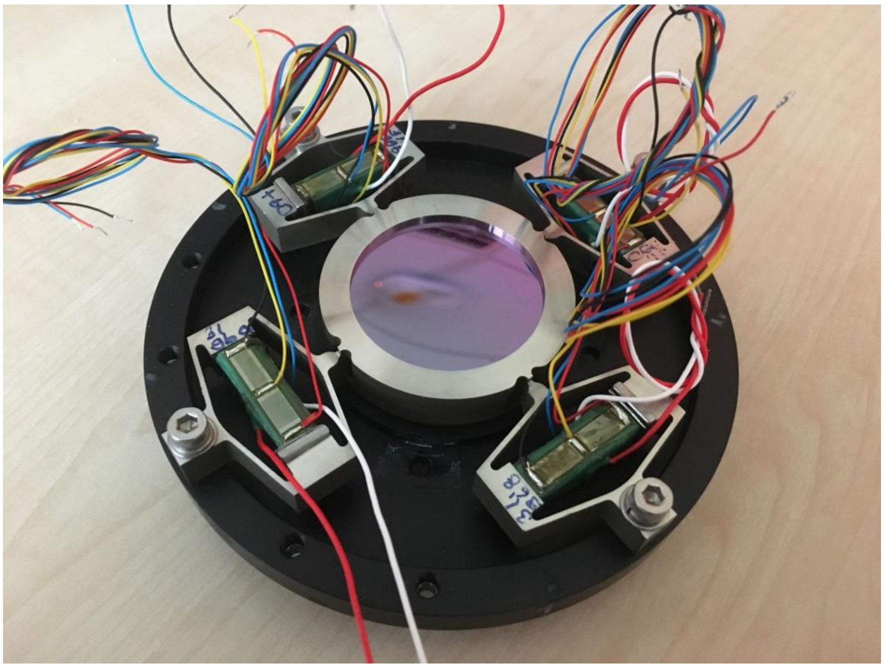

Figure 2.15 Piezo Actuator Module

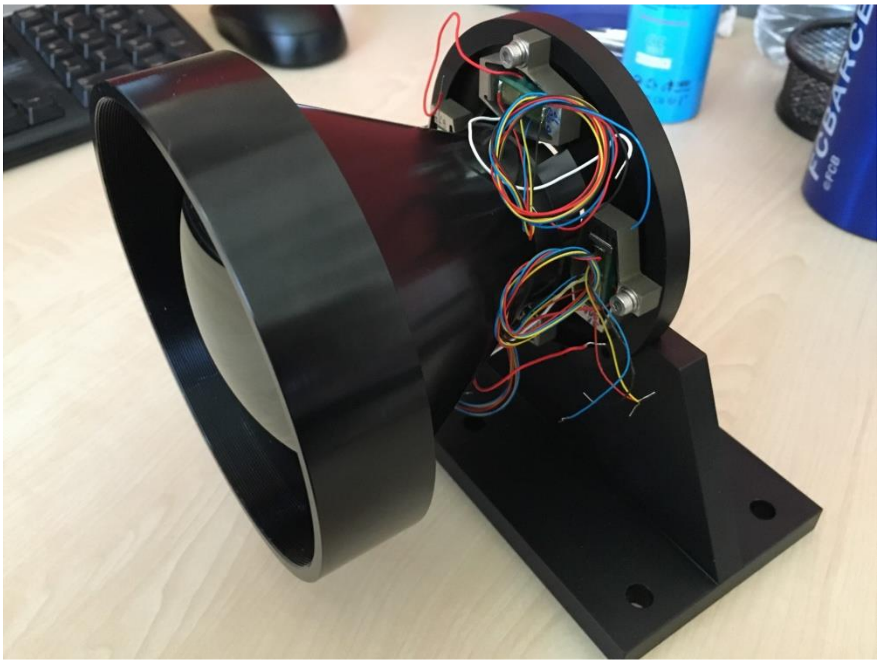

Figure 2.16 Long Wave IR Objective with Micro Scanning

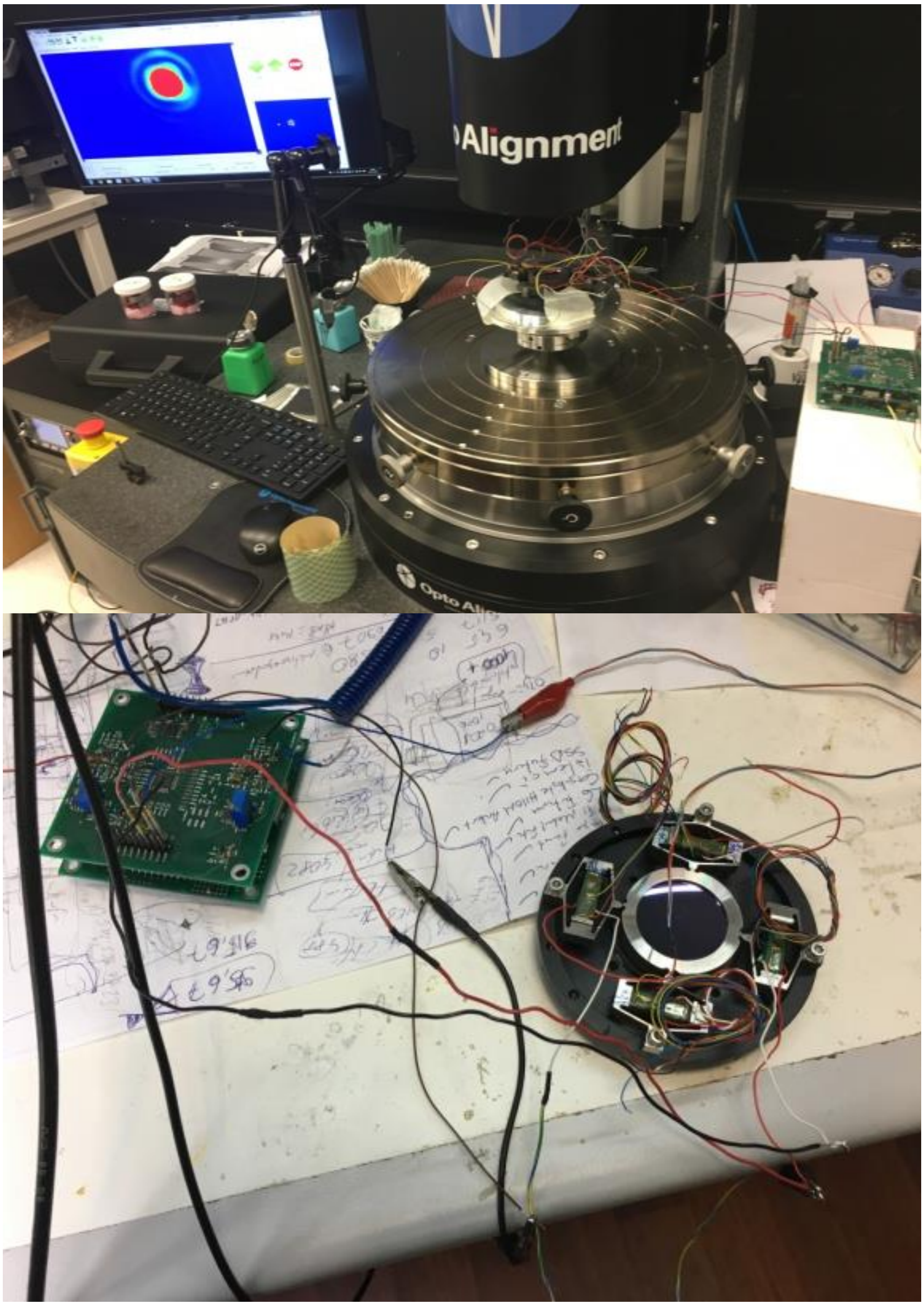

Figure 2.17 Displacement Measurement Set-up and Driver Hardware

The frequency can be adjusted from 1 Hz-100 Hz and the sinusoidal and square wave can be applied with a signal generator. The displacement test has been executed at 1

Hz – 5 Hz range. The controller board was supplied by 25 V and 0.3 A and has generated 150 V for each piezo actuator.

2.4.2.3. Objective Level Test, Image Capturing and Resolution Enhancement

The Long Wave Infrared (LWIR) objective with micro scanning system has been assembled to the uncooled 640x480 pixel resolution micro bolometer detector. USAF and half moon targets have been projected from collimator to capture the image at different scanning frequency. Non-uniformity corrected raw data was recorded pixel by pixel and reconstructed to double the resolution of image on Matlab. A super-resolution image was created from four frames taken at each actuator scanning position.

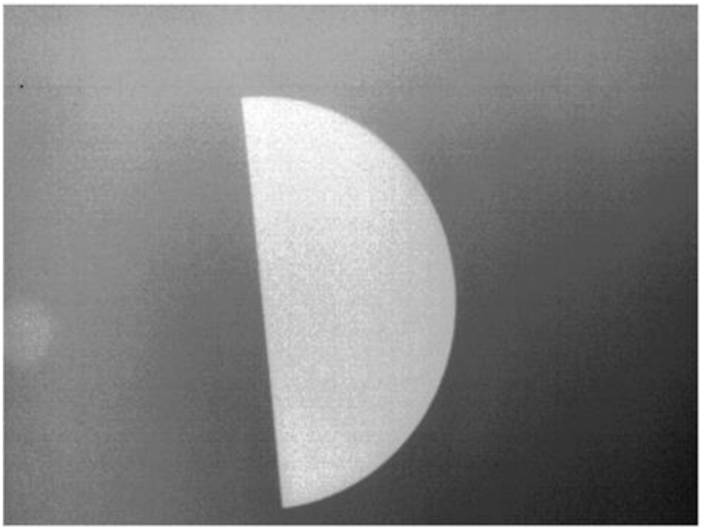

Figure 2.18 Half Moon Target 640 x480 Resolution Image

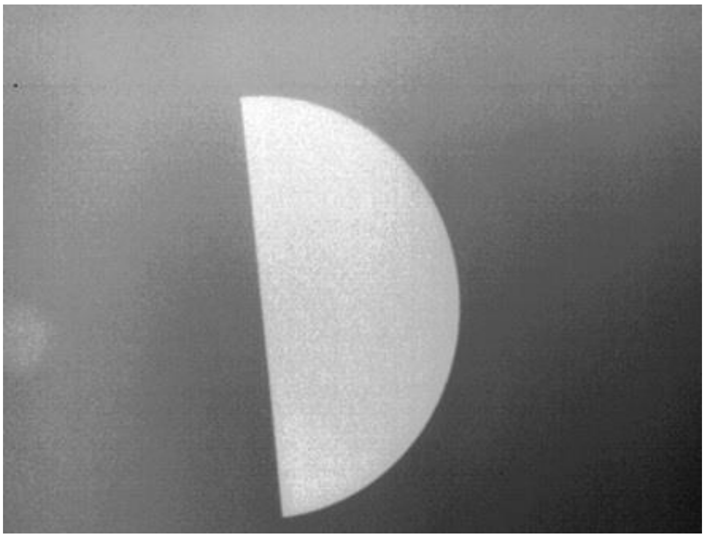

Figure 2.19 Half Moon Target 1280 x960 Resolution Reconstructed Image

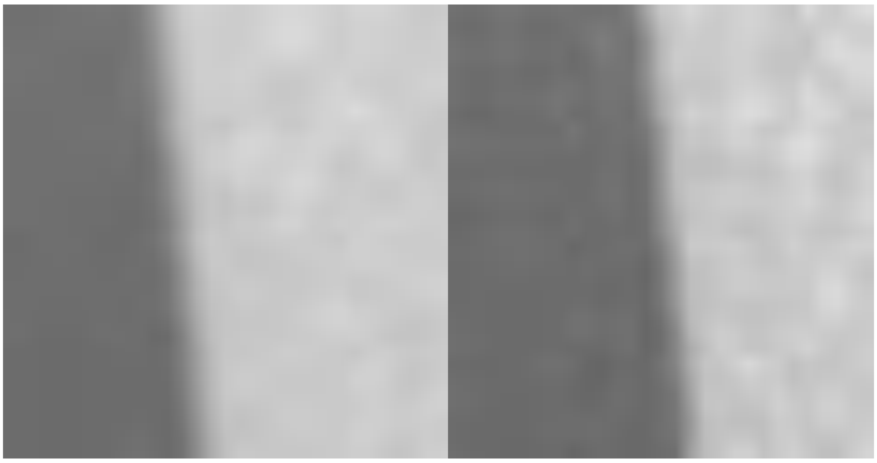

Figure 2.20 Half Moon Target Edge Sharpness a) 640 x480 Captured Image b) 1280 x960 Resolution Reconstructed Image

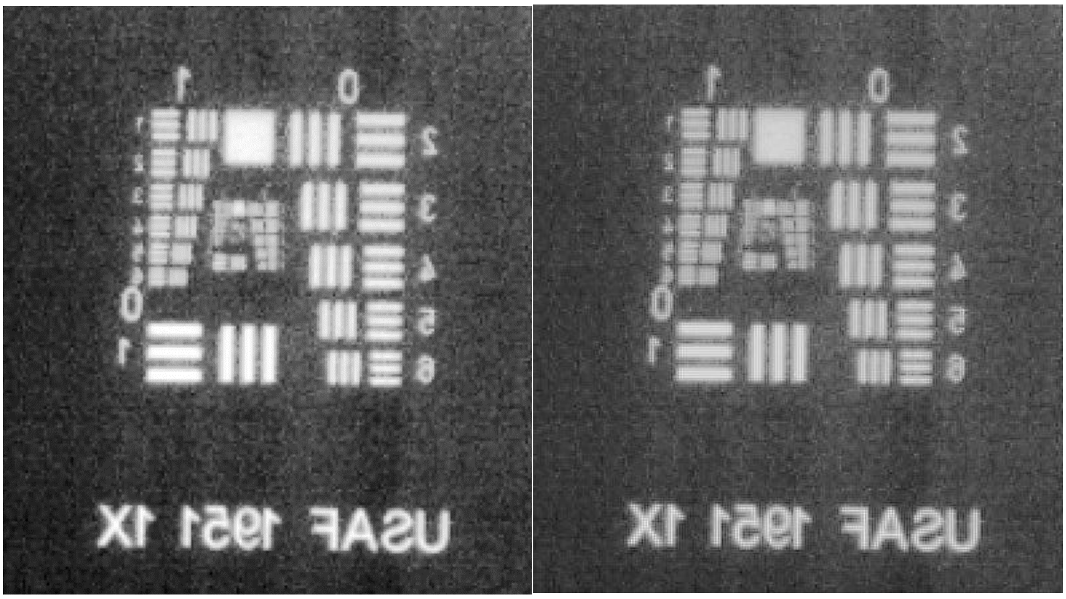

Figure 2.21 USAF Target a) 640 x480 Captured Image b) 1280 x960 Resolution Reconstructed Image

To understand the resolution enhancement and sharpness effect on the image, the edges of half moon of both images were zoomed in at Figure 2.20. Also USAF target images have been evaluated with the same method. The effect of the resolution enhancement can be seen in the figure below. The unresolved smaller 4 bar target has started to be resolved after stitching the scanning images.

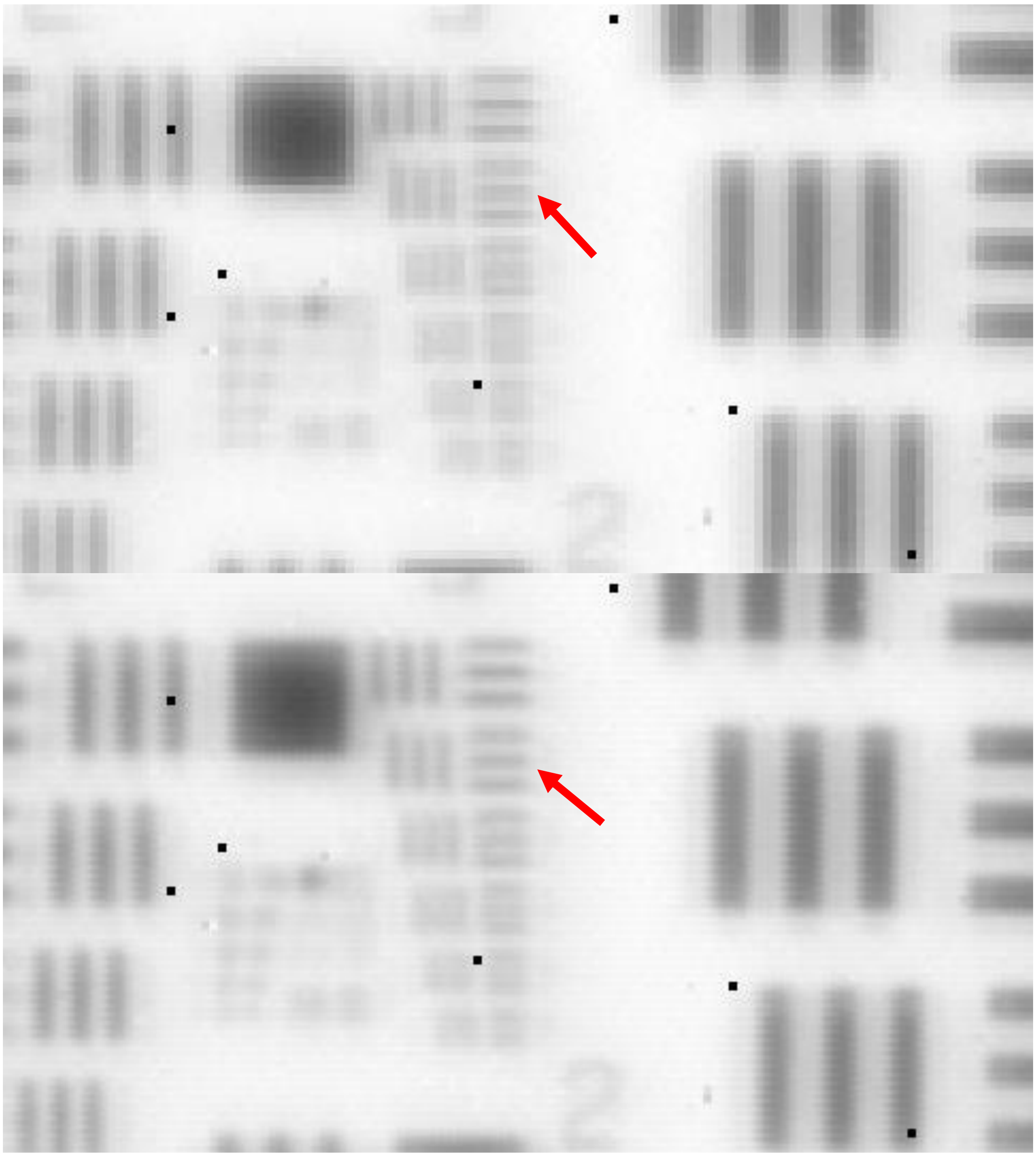

Figure 2.22 a) Low resolution 640*480 image b) High resolution stitched 1280*960 image

Deconvolution is a computationally intensive image processing technique that is being increasingly utilized for improving the contrast and resolution of digital images captured. The main aim to indicate these deconvoluted images is that high resolution image contrast can be improved by algorithmic method like deconvolution. Applying these algorithmic methods to low resolution images for improving contrast may not be so much effective so much. Figure 2.23 shows that one smaller 4 bar target can be resolved by applying vertical and horizontal deconvolution algorithm on stitched 1280x960 image.

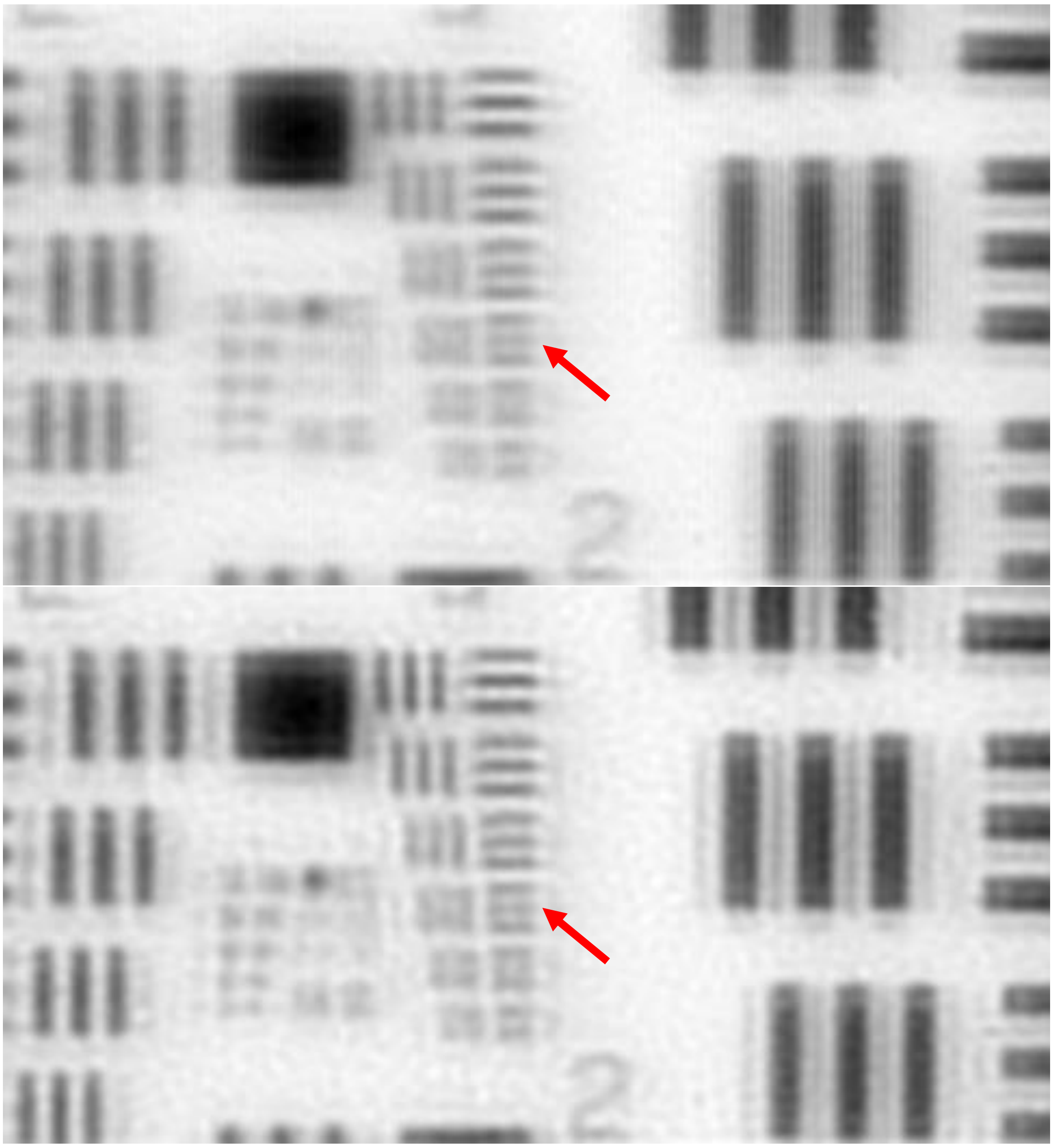

Figure 2.23 a) Vertical deconvolution b) Vertical and horizontal deconvolution

The cross section of 4 bar image marked above has been graphed below for low and micro scanned high resolution and deconvolution one and double sided. When the blue and orange lines are compared, it is seen that while the contrast difference is very small in the blue line, the transitions become more pronounced in the orange line. Owing to these transitions, the image processing algorithm was able to catch the contrast difference and increase the resolution one more level.

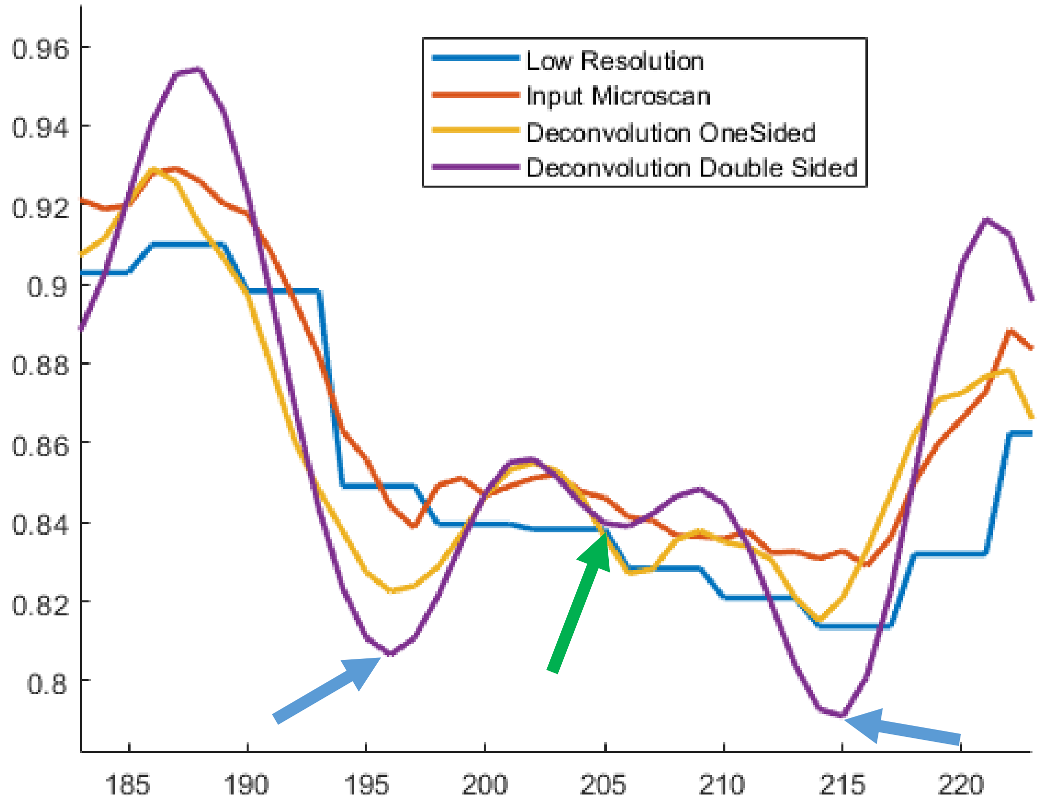

Figure 2.24 Four Bar horizontal cross section graphs of all images

2.4.2.4. Review of Piezo Actuator Design and Micro Scanning Research

Although piezo ceramic materials have high load carrying capacities, they can provide elongation from nanometer level to a few micrometer level when an electric field is applied. Since the elongation is limited, displacement amplification compliance mechanism must be used for macro applications. The displacement test results showed that the results obtained in the analysis and the test results are quite close to each other.

An increase in resolution has been demonstrated by combining the images obtained as a result of micro scanning tests. Seeing the resolution increase indicates that the lens movement required for micro scanning in the optical architecture is calculated correctly and the piezo ceramic material is modeled correctly in the analysis. Although resolution enhancement techniques using algorithms are not within the scope of the study, it has been tried to show that high resolution will also have a positive effect in this context, and an additional resolution increase has been achieved by using the deconvolution method.

Piezo actuators have some disadvantages besides the above mentioned advantages. The most important of these are that they are structurally large and require high electrical power for elongation, which creates the need for large-sized power electronics boards and high power consumption. In addition to this, it is hard to adapt the piezo material to the micro applications in terms of fabrication difficulties.

CHAPTER 3

NOVEL MICRO SCANNING SYSTEM DESIGN BY USING OPTICAL MEMS BASED THERMAL CHEVRON ACTUATOR

Bulk piezo ceramic actuators need complicated amplification mechanism, high volume and power in the system. On the other hand, thin film piezo actuator may be an alternative to the bulk ceramic one but the fabrication of thin film piezo actuators is so difficult and has lack of material alternative. Because of small volume, high force and displacement requirements, reliability and simple fabrication, MEMS based electro-thermal actuation method was chosen as a first start. In this chapter, new optical design for miniaturization, metrics for micro scanning and the design of optical MEMS electro-thermal actuator are described in detail. The mechanical and electrical features of the system affecting each performance criteria are analyzed.

3.1. Adaptation of Micro Scale MEMS Based Systems to the Macro Scale Optical Application

The main motivation of this research is to design MOEMS system for stabilization and enhancing the resolution of a real macro scale optical system. With that motivation, the unique properties of MEMS systems defined above have directed the research to make a MEMS based actuator. However, there is a significant difficulty, which is the lower output force of MEMS based systems than conventional macro scale actuators which shall be overcame. Two main things shall be done to overcome this obstacle which are the decreasing the mass of payload lens as low as possible and searching MEMS based actuator with highest output force. From these points of views, lens has been designed with using diffractive surface to obtain lower thickness and diameters. For the second requirement, the MEMS Based actuator techniques have been searched and discriminated with respect to the actuator characteristics, theoretical and practical limits like output force.

3.2. Advantages and Disadvantages of MEMS Based Actuation Techniques

Thermal Actuation is the first alternative because of its high force, large displacement, lower actuation voltages and relatively simple fabrication. Switching speed of thermal actuation (hundreds of microseconds) satisfies micro scanning applications, if the displacement requirement can be obtained without reaching high temperatures.

The Buckle Beam Thermal Actuator (Chevron), having a V shaped beam, has been chosen because its overlapping features to requirements. The force of buckle beam thermal actuator increases with connecting parallel lines. Displacement is directly proportional with the length of the beam and V shape angle of the buckle beam.

3.3. Analytical Theory Behind V-Shaped Thermal Actuators (Chevron)

The half span of a V-shaped thermal actuator with reaction forces replacing the action of the missing half typical is shown in the inset of Figure 5.1.

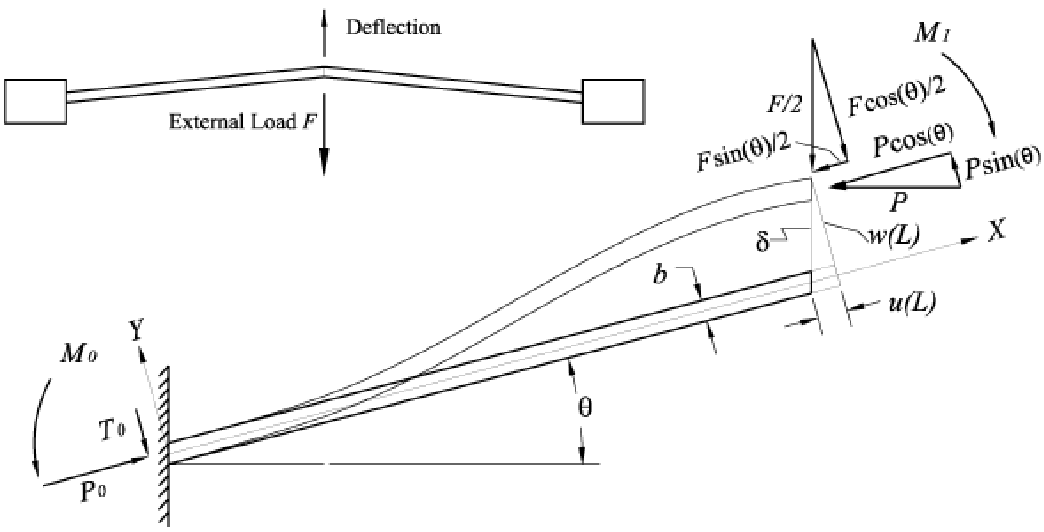

Figure 3.1 V-shaped beam actuator: geometry and loads.[39]

The constrained beam is subject to both compression and lateral bending moment, resulting in lateral displacement. Using geometric symmetry, force, and moment equilibrium conditions, the reaction forces acting at the anchor of the beam can be expressed as

$$P_0 = P \times cos\theta + \frac{F}{2} \times sin\theta \quad (19)$$

$$M_0 = M_1 - w(L) \times P_0 - L \times T_0 \quad (20)$$

$$T_0 = P \times sin\theta - \frac{F}{2} \times cos\theta \quad (21)$$

where F is the vertical load applied to the actuator, P and M_1 are the horizontal force and moment, respectively, transmitted from the missing half of the actuator. The initial angle of the beam is θ, its half-length is L , and the transversal deflection of the mid cross section is $w(L)$. Assuming that the deformed shape of the beam can be described by a longitudinal displacement $u(x)$ and transversal displacement $w(x)$, the strain in any cross section of the beam is given by

$$\varepsilon_x = \varepsilon_x^0 - y \times w''(x) \quad (22)$$

$$\varepsilon_x^0 = u'(x) + \frac{1}{2}w'(x)^2 \quad (23)$$

where ε_x^0 is the extensional (average) strain and y is the independent coordinate along the axis. Applying Euler-Bernoulli beam-column theory with the addition of the thermal strains results in the following set of differential equations for $u(x)$ and $w(x)$

$$\varepsilon_x^0 - \alpha\Delta T = -\frac{P_0}{EA} \quad (24)$$

$$EIw' + P_0 w = -T_0 x - M_0 \quad (25)$$

where A is the cross-sectional area, ΔT is the difference between local temperature and the substrate temperature, α is the thermal expansion coefficient of substrate. Equations (6-7) require three boundary conditions to solve. Since the internal force P and the reaction moment M_0 are not known, additional two boundary conditions are needed to solve the bending problem. These five conditions are

$$w(0) = 0, w'(0) = 0, w'(L) = 0, u(0) = 0, u(L) = w(L)tan\theta \tag{26}$$

The last condition expresses the fact that the center of the beam can only move in the vertical direction as shown in Figure 5.1. The other boundary conditions are self-explanatory. The detailed solution of the equation;

$$w(x) = \left(tan\theta - \frac{F}{2k^2EIcos\theta}\right)\left(\frac{sinkx}{k} + \frac{(coskL-1)(coskx-1)}{ksinkL}\right) - x \tag{27}$$

Where $k = \sqrt{\frac{P_0}{EI}}$ is the solution of transcendental equation containing the externally applied for F and the average temperature increase of the beam T_{avg}. The transcendental equation is given by

$$\begin{aligned} c(k, F, T_{avg}) = {} & \frac{k^2IL}{A} - \alpha T_{avg}L + \frac{1}{2}\left(tan\theta - \frac{F}{2k^2EIcos\theta}\right)^2 \\ & \times \left(\frac{3L}{2} + \frac{\sin(2kL)}{4k}\left(1 - tan^2\left(\frac{kL}{2}\right)\right) + \frac{L}{2}tan^2\left(\frac{kL}{2}\right) \right. \\ & \left. + tan\left(\frac{kL}{2}\right)\frac{4\cos(kL) - \cos(2kL) - 3}{2k} - \frac{2\sin(kL)}{k}\right) \\ & + tan\theta\left(\frac{2}{k}\tan\left(\frac{kL}{2}\right) - L\right)\left(tan\theta - \frac{F}{2k^2EIcos\theta}\right) = 0 \end{aligned} \tag{28}$$

The average temperature increase of the beam T_{avg} is given by

$$T_{avg} = \frac{1}{L}\int_0^L (T(x) - T_s)dx \tag{29}$$

where T_s is the temperature of the substrate. Equation (10) has been solved for a given value of external load F and average temperature increase T_{avg} to find the eigenvalue k , from which tip displacement δ is determined by Eqn. 27.

$$\delta = \frac{w(L)}{cos\theta} = \left(\frac{2k^2EIsin\theta - F}{2k^2EIcos^2\theta}\right)\left(\frac{2tan\frac{kL}{2} - kL}{k}\right) \tag{30}$$

This formula is only applicable for a single V shaped beam thermal actuator. Many researchers have worked on the comparison of the analytical thermoelastic model with non-linear finite element methods for a single element.

When a voltage is applied to the pads, the chevron beams will expand because Joule heating will exert a force on the beam. The force calculation of a single element V-Shaped Thermal Chevron actuator can be done as below

$$F_{int} = A\sigma \tag{31}$$

where F_{int} is the internal force at the actuator, A is the cross-sectional area of the beam and σ is the coefficient of thermal expansion. Because the strain $\varepsilon(x) = \alpha T(x)$ and the axial stress with Young's Modulus E is given by $\sigma = E\varepsilon$, using equation (11), the force developed by the actuator with half beam length L

$$F_{int} = A\sigma = AE\varepsilon = AE\alpha T_{avg}L \tag{32}$$

The force at the displacement direction $\delta\ is$

$$F_\delta = \frac{F_{int}}{2}sin\theta + \frac{F_{int}}{2}sin\theta = F_{int}sin\theta \tag{33}$$

For N chevron beams, the total force is

$$F_{total} = NF_{int}sin\theta \tag{34}$$

In additional, many researches have been done to solve heat transfer problem analytically. Joule heating, also known as resistive, resistance, or Ohmic heating, is the process behind the chevron heating. At Joule heating, the electric current passes through a conductor or semiconductor and produces heat.

$$P_{joule} = I^2R = VI \tag{35}$$

$$P_{joule} = \frac{mc\Delta T}{t} \tag{36}$$

$$\Delta T = \frac{P_{joule}t}{mc} = \frac{VIt}{mc} \tag{37}$$

where P_{joule} is the power (watt, energy per unit time) converted from electrical energy to thermal energy, I is current (ampere), V is voltage difference, t is time (sec), m is mass (kg), ΔT is delta temperature (C^0), c is the specific heat capacity (Joule/kgK).

In this research, the designed model is complicated to achieve system requirements which are 2 axis decoupled motion, high displacement and withstanding high payload. Because of that, the structure shall be so complicated to calculate the system analytically and therefore, finite element methods have to be applied to calculate temperature changes, displacements and forces with taking gravity into account.

3.4. The Design of a Novel MEMS Based V-Shaped Chevron Type Thermal Actuator for Lens Micro Scanning System

The V-Shaped Thermal Chevron (VSTC) actuator has several advantages when compared to the other MEMS Based actuator techniques like Electrostatic, Piezo and Magnetic. These are high force output, large stroke, high yield fabrication, low actuation voltages and robustness. The main criteria to choose VSTC type actuator for this application are high force output and long displacement due to the high weight of germanium lens and high pixel size. The actuator is designed to integrate a LWIR camera having 2 lenses and an uncooled detector with 640x480 pixel resolution with 17 micrometers pixel size. Each actuator has 40 micrometers decoupled displacement capability which required to obtain sub-pixel image motion on the detector. Frequency of actuation is 25 Hz which means the construction of one frame takes 40 milliseconds to get super resolution. SOI having low resistivity (<0,005 ohm-cm) has been selected to prevent supplying high voltage for obtaining displacements.

3.4.1. The Definition of Requirements

The proposed micro-scanning thermal chevron actuator is designed for doubling the image resolution of a LWIR camera with a 17 μm pixel size and 640x480 array format, to the 1280x960 pixel resolution. This X-Y Stage actuator also adds image stabilization capability to the imaging system, if needed.

For 17 μm pixel size, a travel of at least half the pixel size (8.5 microns) is needed on horizontal and vertical axes at image plane. This requirement is higher than imaging systems working at visible wavelength because of smaller pixel size, which makes it more challenging to miniaturize.

Zemax is the first tool to analyze the 3D optical ray behavior under micro scanning by using optical design. With this analysis, the decenter value of micro scan component, (that is aspherical surfaced germanium lens for this application) to achieve the required motion on focal plane array of detector has been defined. The layout of the optical design can be seen at Figure 1.

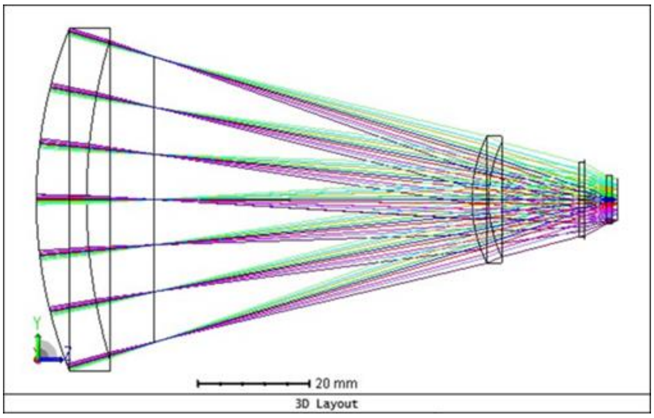

Figure 3.2 Optical Architecture

Optical performance degradation of the second germanium lens has also been checked at 40 micrometers decenter. From the optical design point of view, if the second lens is decentered with 40 micrometers, the point image moves approximately 9 micrometers, nearly half of the pixel size of detector. Therefore, the main aim is to decenter the lens with a MEMS based thermal actuator mechanism having 40 μm elongation at required frequency. Such a germanium lens weighs 1.2 grams with dimensions of 14 mm diameter 1.5 mm thickness.

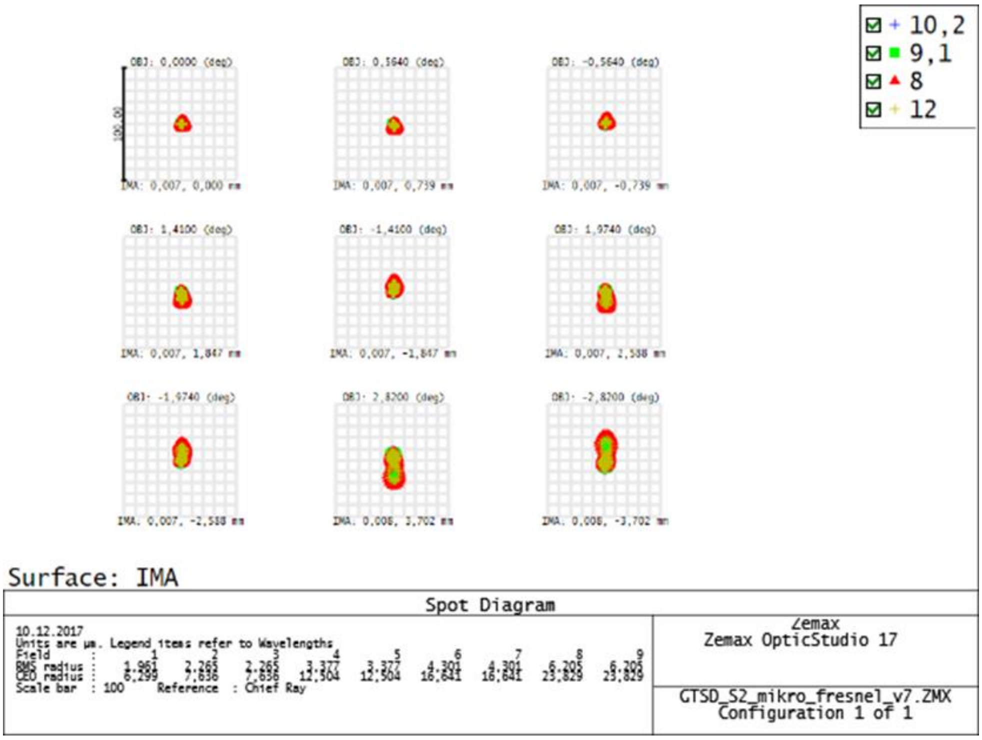

Figure 3.3 Spot size after 40 micrometers lens decenter

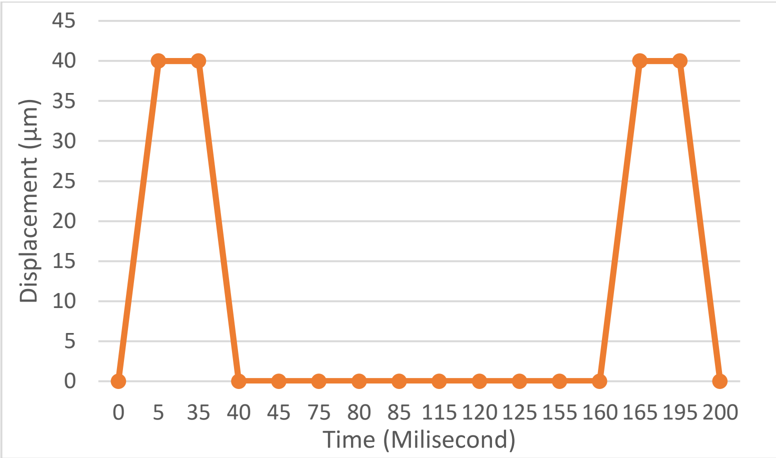

Figure 3.4 Displacement graph of single Actuator

The displacement versus time graph shows the motion profile required to double the resolution by using 4 frames. At the graph, the integration time of the detector defines the step range.

3.4.2. Thermal-Electrical, Structural Design and Analysis

From the equations in Chapter 6.1.3, the critical parameters of the V-Shaped Chevron type actuator design have been calculated for a single actuator, and later the final 3D geometry has been designed to satisfy the requirements in a CAD environment. A parametric design is utilized for reaching the target displacements by using the finite element analysis method. The most critical parameters, the number of chevron beams (N), the length (L), the angle (θ) and thickness (b) of each beam, have been defined as variables and optimized with respect to the constraint parameters like displacements and mass geometry.

The decoupling performance of each axis, which is another critical issue, is achieved with dedicated flexures to restrict the tip deflection of the thermal actuators to single degree-of-freedom. Figure 2 shows the front view of 2 axis thermal chevron actuator with decoupling flexures. Total footprint dimension is 38.8 x 38.8 mm.

For the fabrication of the scanner, a 4" Silicon on Insulator (SOI) wafer with 500µm device layer and 200µm handle layer is micromachined. The resistivity of the boron doped device layer is 0.005 ohm-cm with <1-0-0> orientation. The dimensions of the actuator and material specifications of SOI are summarized in Table 6.1 and 6.2.

Table 3.1. *Actuator Dimensions*

Length, L (mm)	*Angle,θ (deg)*	*Thickness,b (um)*	*Number of Nodes*
9	20	200	10

Table 3.2. *Properties of Silicon on Insulator (SOI)*

SOI Properties		*Handle Layer*	*Device Layer*
Size (mm)	100+/-2		
Buried Oxide Thickness (um)	2		
Type-Dopant		P/B	P/B
Orientation		<1-0-0>	<1-0-0>
Thickness (um)		200+/-5	500+/-10
Resistivity (ohm-cm)		>1,000 FZ	<.005

The analysis and simulation of the micro scanning mechanism has been done in ANSYS multi physics analysis environment. Some other material properties that are not available in data sheet of supplier like density and thermal expansion coefficient etc. have been obtained from literature.

Different spring designs have been evaluated to obtain required stiffness and flexure behavior of mechanisms. Two flexure designs illustrated at Figure 3.5 have been applied to the actuator.

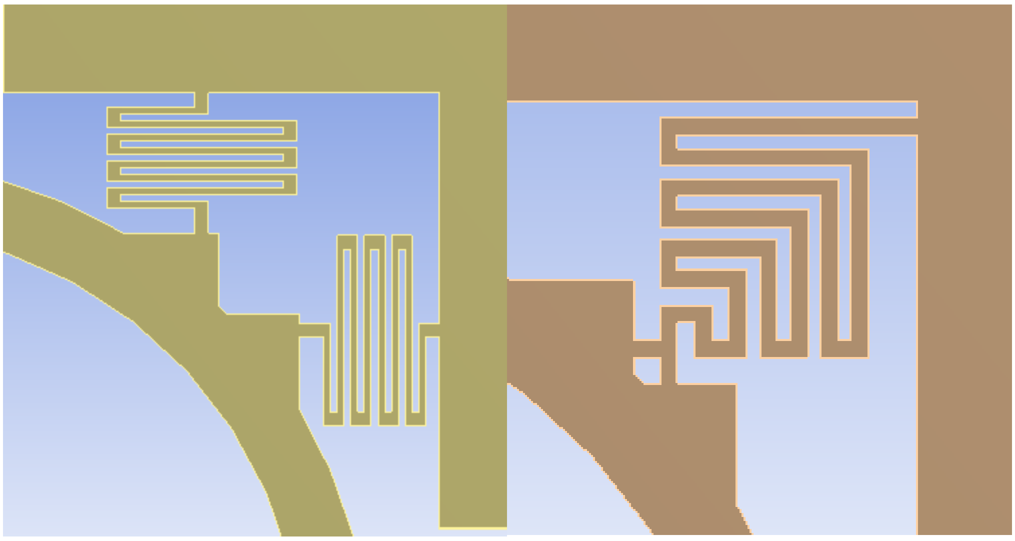

Figure 3.5 Flexure Design Alternatives

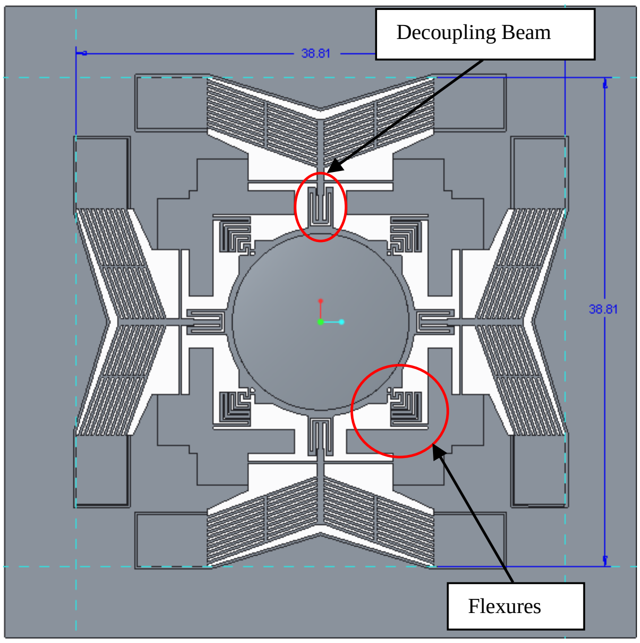

Figure 3.6 Front view of 2 axis thermal chevron actuator with decoupling flexures and dimensions in mm.

The applied voltage is 5.5 volts for the thermal-electrical analysis shown in Figure 3.7(a) where the maximum temperature is found to be 829 degree Celsius. Heat transfer boundary conditions are convection and radiation. The ambient temperature is 22 degrees Celsius and the convection film coefficient is 20 $pW/\mu m^2$. For the radiation input, emissivity is assumed as 1. The mass of germanium lens is simulated as point mass. After these analyses, the dimensions of actuator shown in Table 3.1 have been verified.

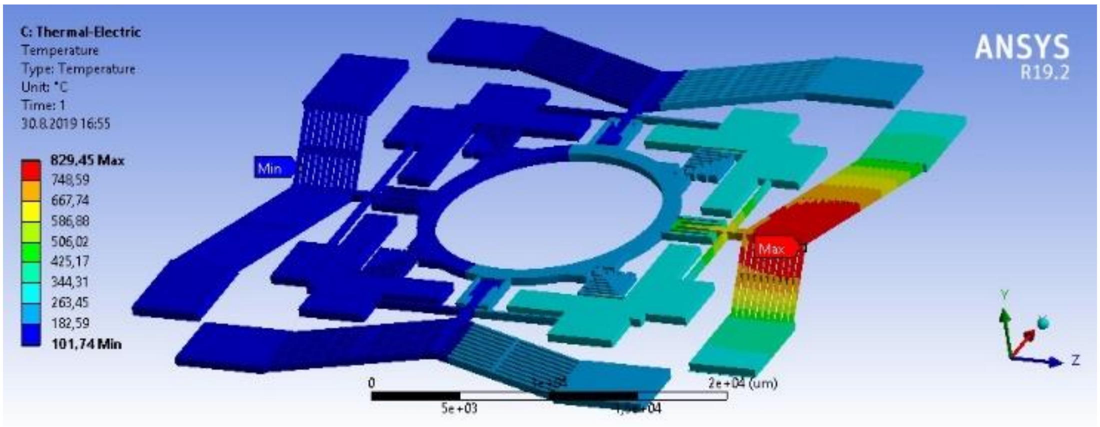

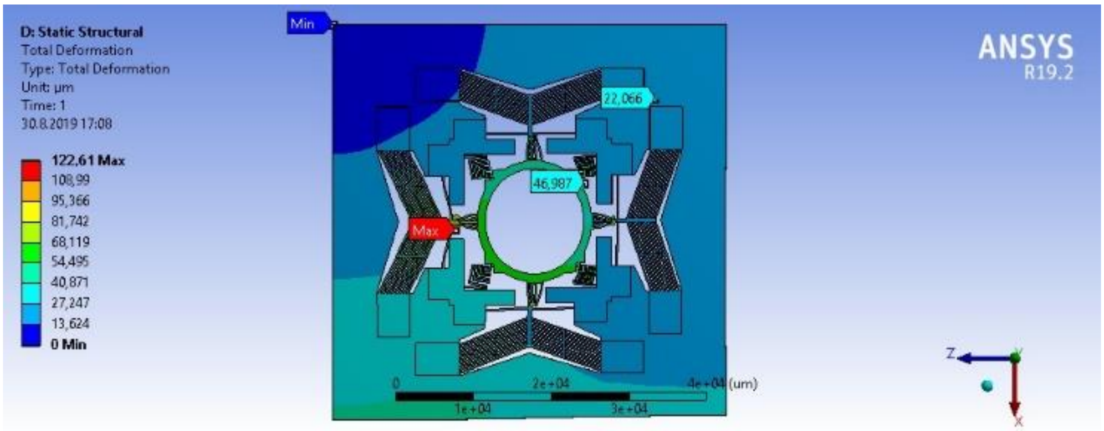

Figure 3.7 (a) Distribution of temperature and (b) axial displacement at 5.5 volts.

Figure 3.7(b) shows the total displacements of actuator for a single axis actuation and single axis displacement. The average displacement of a single axis is around 37 micrometers. The decoupled axis displacement is simulated to be less than 2µm.

3.4.3. Prototyping

Diffractive surfaced germanium lens has been manufactured with Single Point Diamond Turning and then coated with Anti-reflective thin film coating by using Physical Vapor Deposition (PVD) techniques.

Figure 3.8 Diffractive Surfaced Germanium Lens

MEMS fabrication techniques have been evaluated to manufacture the actuator and the process steps have been defined and lithography masks have been designed with respect to the patterns. Below are the steps of manufacturing process;

a. Chromium (adhesion layer) and Gold coating with Physical Vapor Deposition

b. Spin photoresist on handle layer of wafer

c. Patterning of gold contacts with lithography mask

d. Wet etching with TFA etchants for 45 seconds

e. Removing the photoresists with PRS2000 solvent

f. Removing gold layer alignment pattern

g. Patterning the micro structure with lithography mask

h. Etching with Deep Reactive Ion Etching (DRIE)

i. Removing the photoresists with PRS2000 solvent

j. Spray photoresist on device layer of wafer

k. Patterning back surface with lithography mask

l. Etching back surface with Deep Reactive Ion Etching (DRIE)

The process steps are visualized at Figure 3.5, respectively. Four different lithography masks have been drawn and manufactured for the contact layer, micro structure layer for two different flexure design alternatives and the back surface.

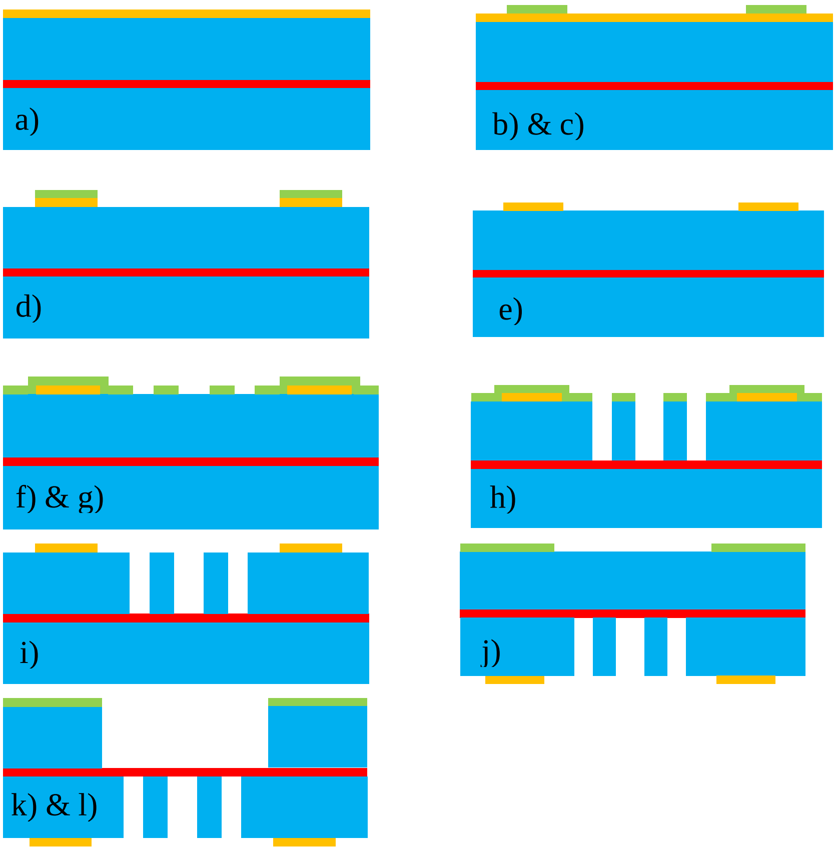

Figure 3.9 Illustration of fabrication steps

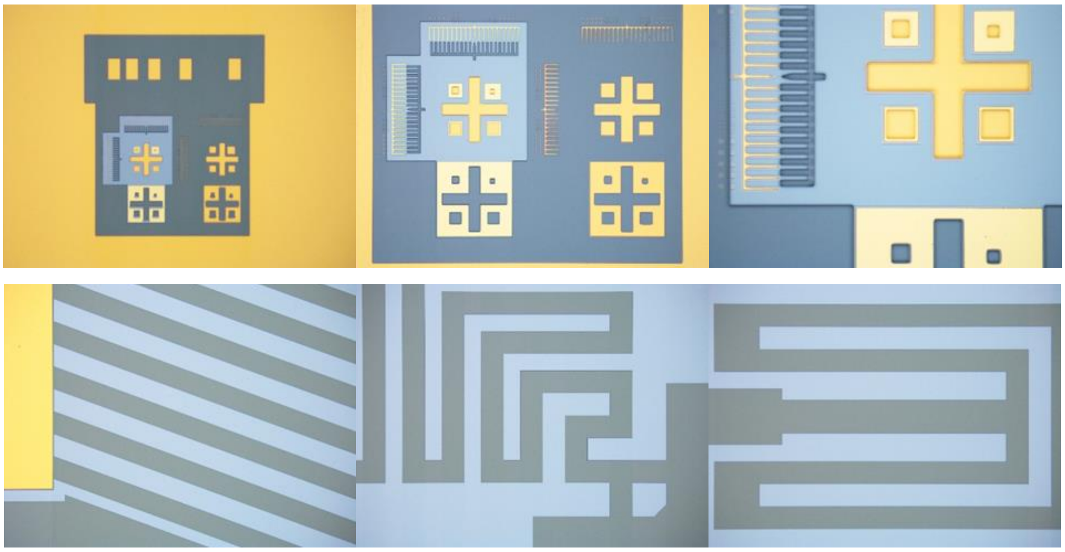

Figure 3.10 Images of lithography mask of micro structures

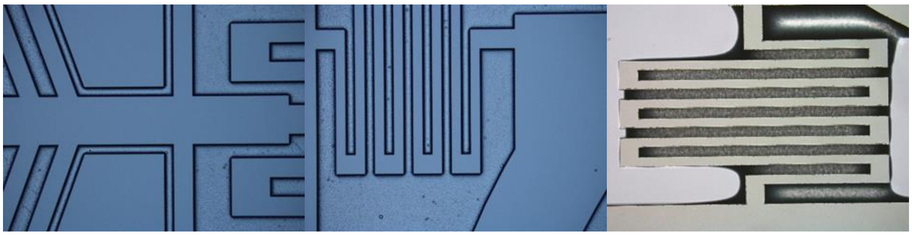

Figure 3.11 Microscope images of micro structures after DRIE etching process

Figure 3.12 indicates the SEM images of microstructure patterns and etching surfaces. The alternatives of the entire microstructure for two different flexure designs have been shown at Figure 3.13. The images were taken after process step in DRIE etching of micro structures. After that step, back surface was sprayed with photoresists and patterned.

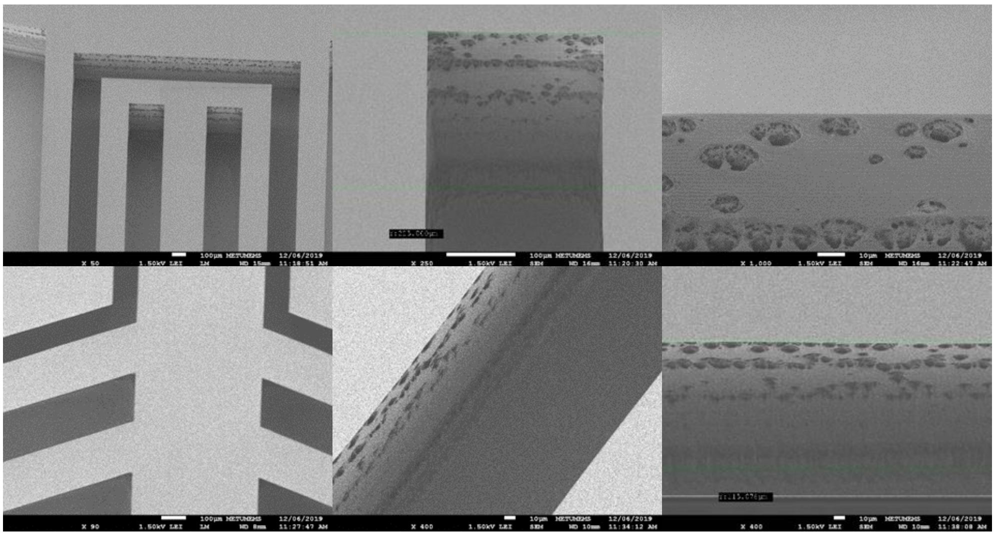

Figure 3.12 SEM images of micro structures

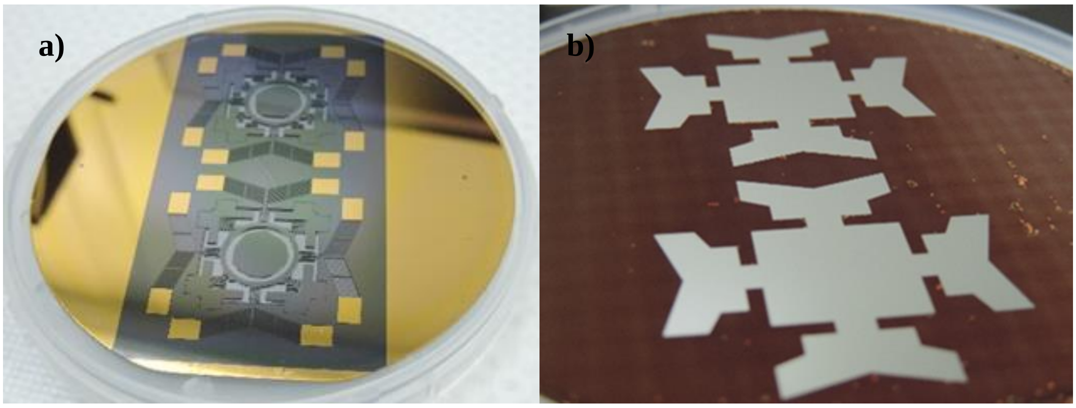

Figure 3.13 a) Images of entire micro structures after step I b) Images of back surface pattern.

After the fabrication of the VSTC actuator, the lens was attached to the center of the actuator using epoxy based adhesive.

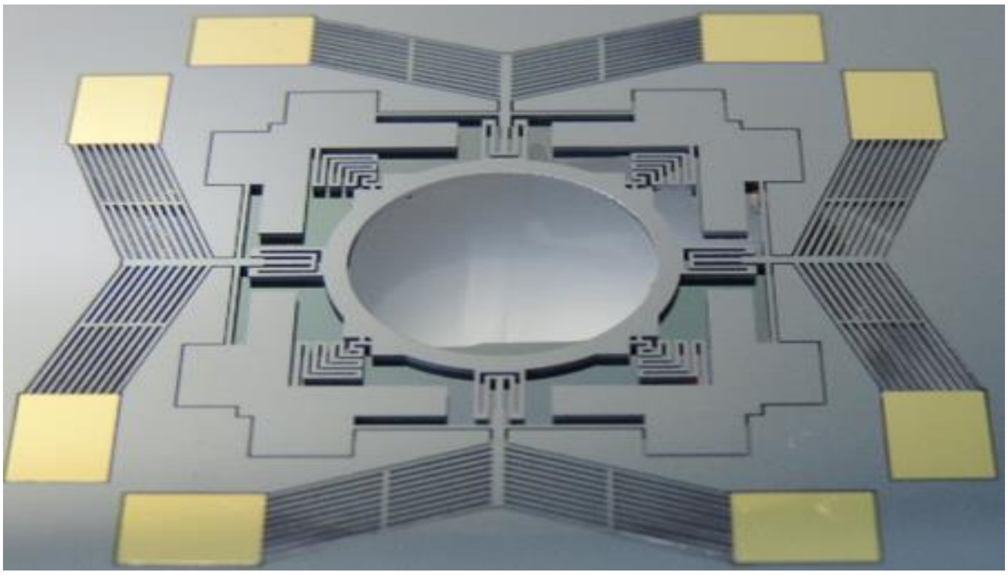

Figure 3.14 Fabricated actuator prototype.

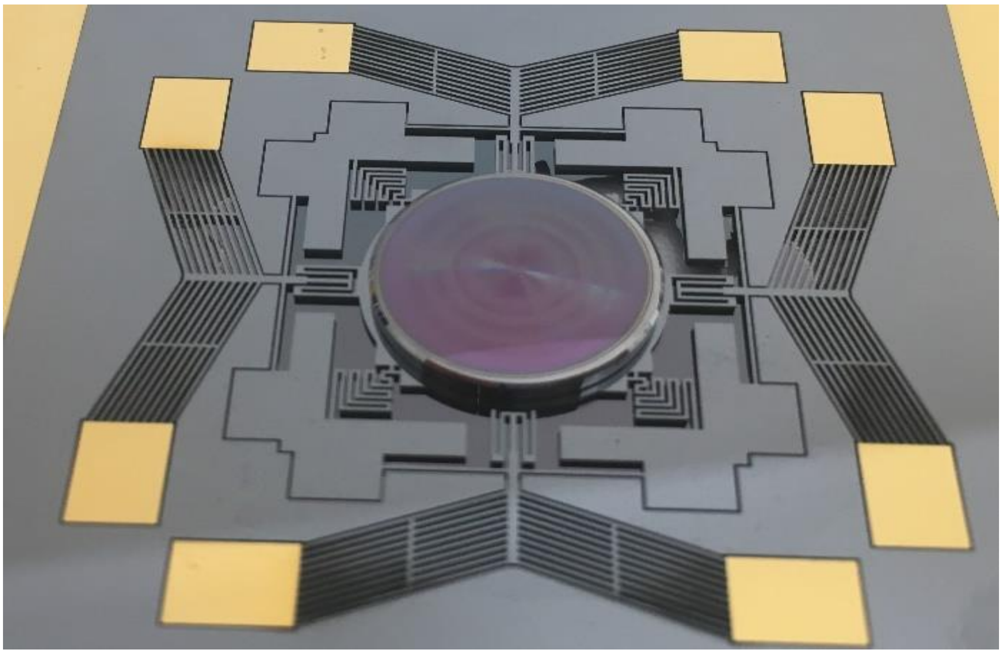

Figure 3.15 Lens micro-scanner assembly.

3.4.4. Testing

The displacement of the VSTC actuator was measured on a probe station by applying required electrical power shown in Figure 3.16. While applying the different voltage levels to the contacts, the lens displacement and the current were measured (Figure 9). Applied voltage to system by power supply via cable and contact pins is +6V and -6V for each contact of actuators. Contact resistances were calculated and eliminated for each actuator to characterize the performance of the silicon structure only.

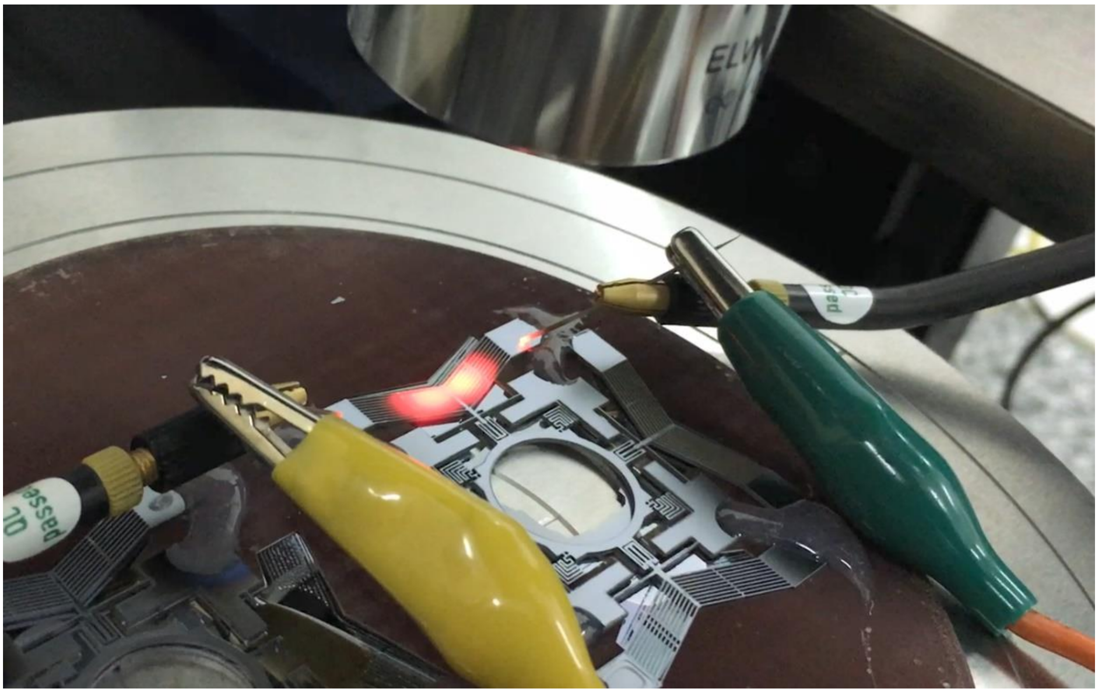

Figure 3.16 Probe Station Test Set-Up

3.4.5. Results and Discussion

The proposed VSTC actuator consists of 2 axis decoupled stage and has 4 separate V-Shaped thermal actuators supplying sufficient force and displacement to move lens within required time.

Maximum deflection obtained during the tests with +5.5V was around 22µm, while simulations were predicting a deflection of 37µm for +5.5V. This discrepancy is attributed to the relatively poor thermal conduction and the change in material properties caused by substrate heating and expansion in practical tests. Thus, the second design iteration will take these effects into account.

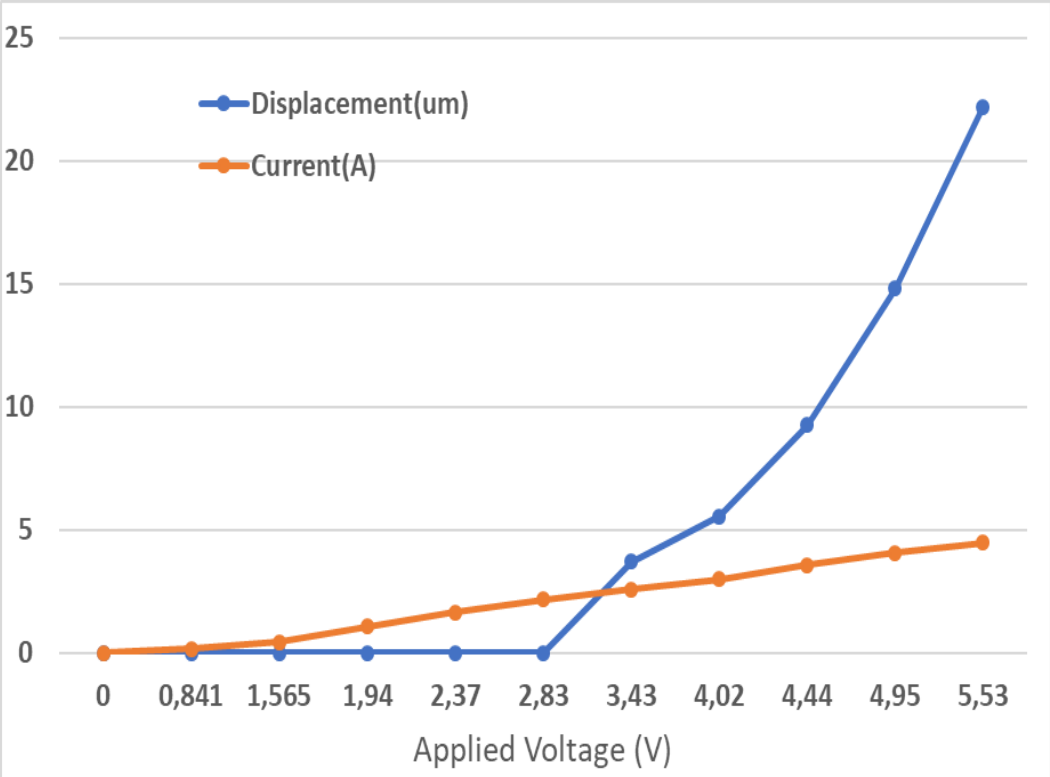

Figure 3.17 Tip displacements and currents at different excitation voltages.

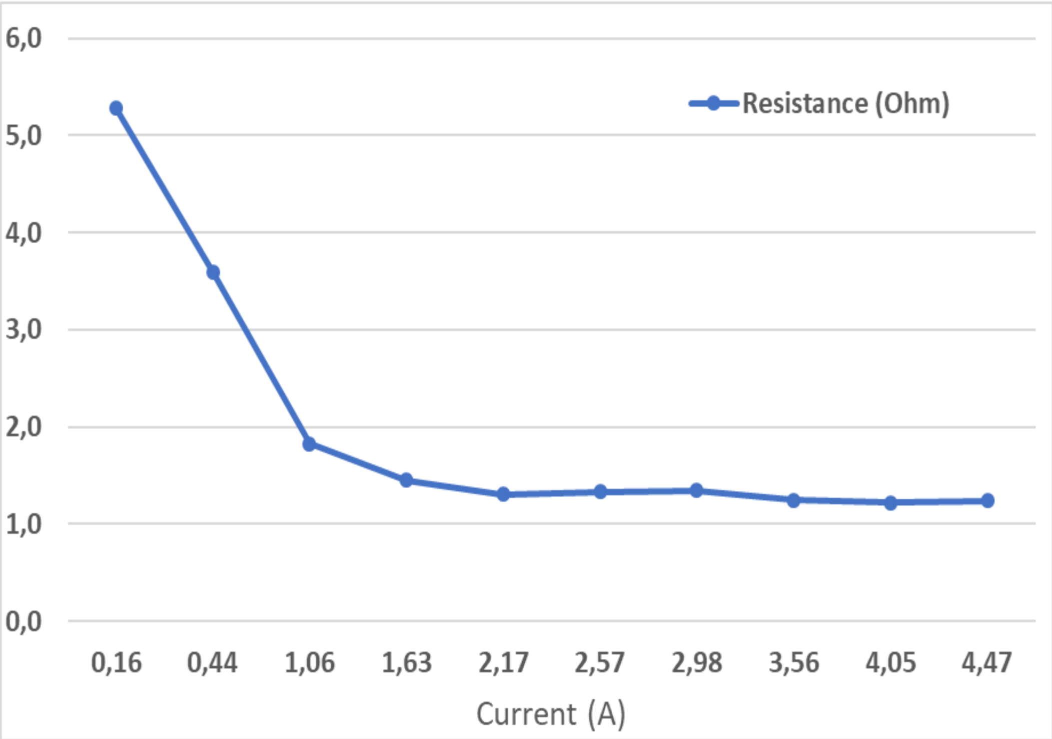

Figure 3.18 Resistance of single chevron actuator versus applied current.

Miniaturization of lens has been achieved by using aspherical surface and optimization of optical system parameters. Actuators have 40 micrometers displacement capability required for obtaining sub-pixel image motion on detector. The design enables a frequency of actuation of 25 Hz, which corresponds to the construction of 1 frame per 40 milliseconds, with the use of chopper type drivers and position feedback.

Even further miniaturization of the lens with metasurfaces or coded mask which can be applied on the germanium or silicon by using lithographic techniques will enable a smaller and more power efficient micro scanner. Also, the chevron design can be optimized with respect to the results of the first prototype tests.

CHAPTER 4

A NOVEL ELECTRO-THERMAL MOEMS MICRO SCANNER WITH INTEGRATED CODED MASK FOR SPATIAL LIGHT MODULATION

The study explained in the previous chapter indicates that the fabrication methods of the actuator and optical element are different from each other and the integration of them is a difficult process and makes the complicated. In addition to this, the mass of scanning optical element cannot be reduced without sacrificing from the imaging performance of the system. Therefore, the compressive sensing method and a coded mask for spatial light modulation was decided to use in order to obtain more miniaturization and same fabrication method for both actuator and optical element. In this chapter, the new optical layout for coded mask, the theory of spatial light modulation and the scanning techniques with compressive sensing, the design and analysis of MOEMS actuator, fabrication steps, tests and results are described in detail.

4.1. Design Improvement and New Optical Architecture

To diminish the center optical payload and eliminate the additional lens manufacturing process, the optical architecture has been changed and a gold coded mask, obscuring the image, has been placed on the internal image plane of the optical system. Actuation moves the coded mask at subpixel length and displacement changes the line of sight of the object plane of the optical system by scanning and the construction of each scanning frame has been used to obtain resolution enhancement of the image. The minimum and maximum size of pattern is defined by the pixel size of detector and magnification of relay optics.

Moreover, the total size of the system has been decreased by changing optical architecture dramatically and the manufacturing process has become more compatible with lithography techniques.

On the other hand, a single actuator design has been modified and the middle column between the chevron arms have been removed, re-optimized and the displacement-arm length ratio has increased significantly.

The other critical issue is that the remaining layer of SOI wafer on optical footprint shall transmit the related wavelength of the optical system. Meanwhile, its resistivity should be as low as possible to prevent the necessity of high driving voltage for heating.

4.2. Optical Architecture

The payload of a MEMS based actuator is a coded mask pattern placed on the internal image plane of mid wave infrared optical system. An optical architecture consists of an objective and relay group, flat mask pattern and IR detector. Mask pattern scanning on internal image plane is utilized for coded compressive imaging and behaves as a spatial light modulator. The system gathers noise under sampled measurements of spatially modulated light intensity from a scene of interest. Spatial modulation at sub-pixel level can be performed by using a coded mask having sub pixel size feature at a finite image plane of relay optics. Modulated intensity on the low-resolution Focal Plane Array (FPA) is integrated and the original image on low resolution FPA is reconstructed using different image processing algorithms like sparse recovery.

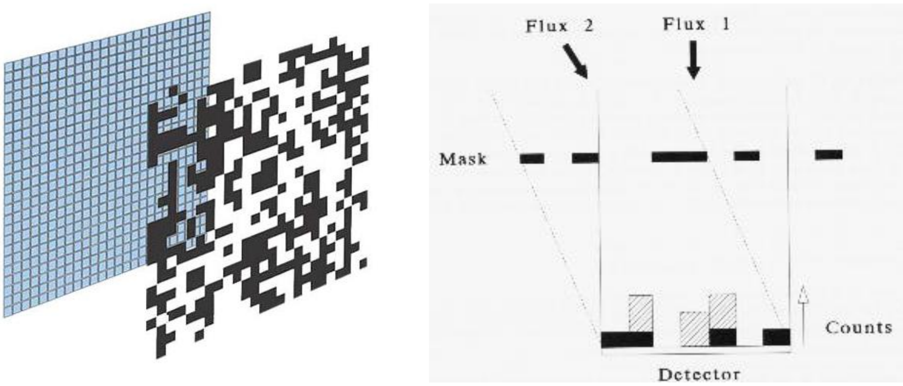

Figure 4.1 Basic Concept of Coded Mask [45]

The basic concept of coded-mask imaging is that two-point sources illuminate a position-sensitive detector through a mask. The detector thus records two projections of the mask pattern. The shift of each projection encodes the position of the corresponding point source in the scene; the 'strength' of each projection encodes the intensity of the point source.

Optical transmission, magnification of relay lens, obscuration ratio and algorithm requirements define the mask pattern. Algorithm issues are out of scope for this study.

In infrared imaging systems, the radiation from the scene is very important. With this method, although the resolution is increased, the infrared radiation coming from the scene decreases due to the masked regions and the range performance of the system decreases. For this reason, it is necessary to determine the density of the mask at the optimum level not to affect the range performance of the optical system dramatically.

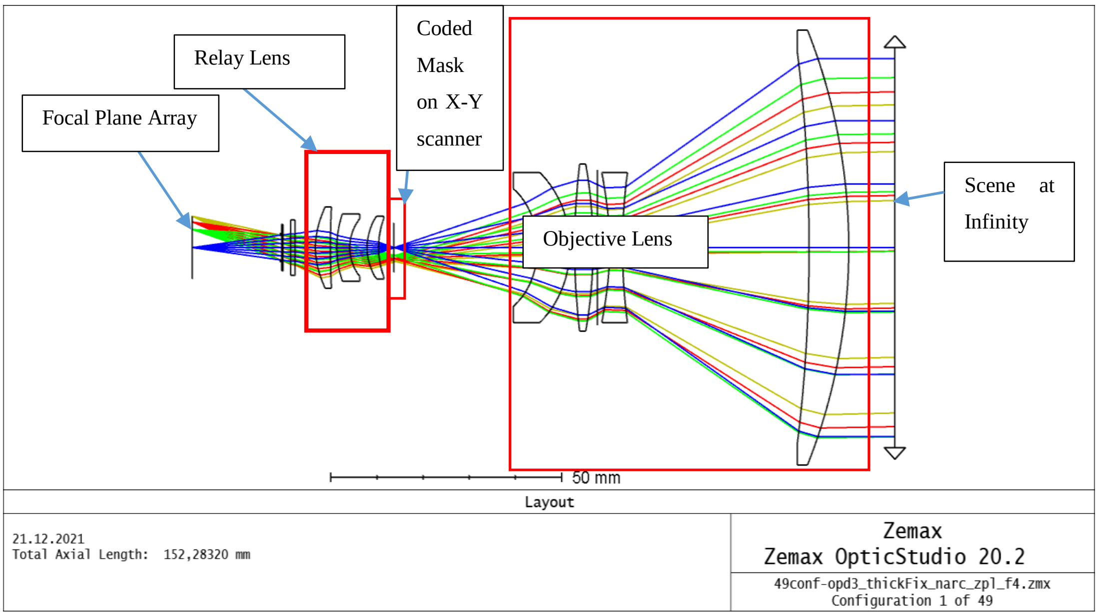

Figure 4.2 Optical Layout of Coded Compressive Imaging

Scanning position control is carried out by following the special shapes on the mask sampled in figure below.

Table 4.1. *Optical Specification*

Optical Specifications	*Value*	*Unit*
Field of View	1.8	Degree
Relay Magnification	2.5	
FPA Format	640*512	
Pixel Size	15	µm

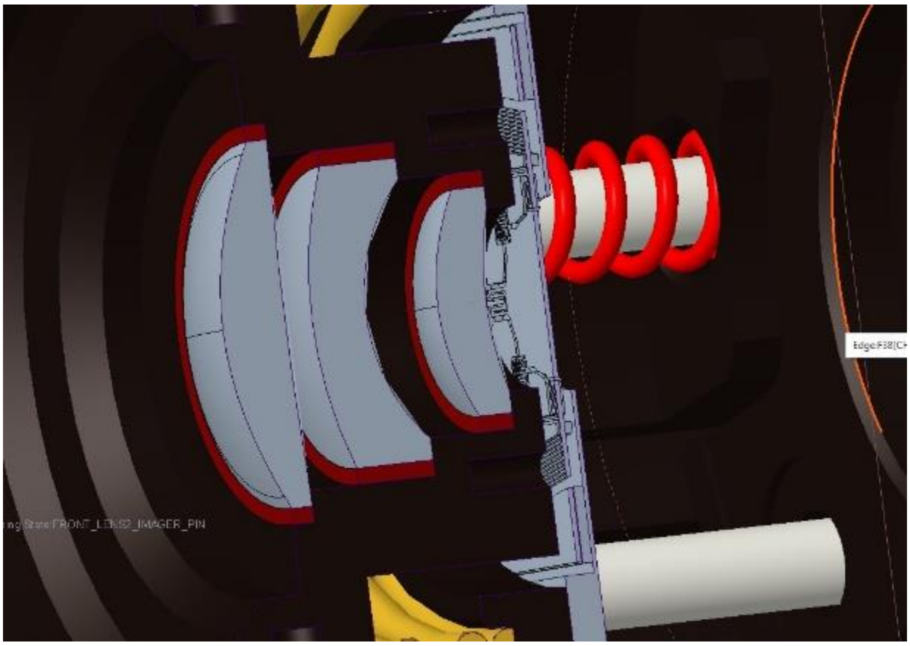

Figure 4.3 Relay Opto-mechanical view with coded mask

4.3. Alternative Designs of Decouple and Spring Flexure Structures

Due to the low displacement capability of MEMS structures, amplification mechanisms are used to obtain the required range of motion. Basically, using the leveling arm, the moment arm is extended and the displacement is increased. By using hinge structures on the leveling arm, flexible pivot points are achieved with compliant mechanism design methods. For the starting point, the design alternatives and applicability of an amplifier compliant mechanism were evaluated by designing an amplifier in front of the actuator.

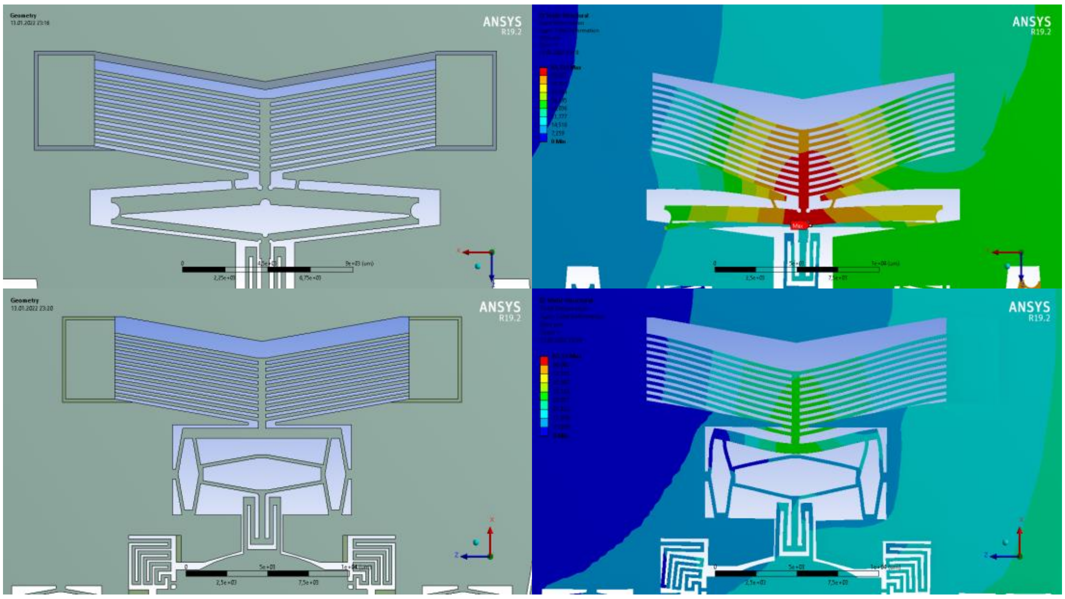

Figure 4.4 Amplifier Compliant Mechanism Designs

With this method, when the amount of movement is increased, the force decreases at the same ratio. Although these methods work in applications with free ends or where the applied force is high, they cannot be applied with this method when displacement and force are needed at the same time. It is necessary to increase the actuator force or to use high displacement actuator methods. Because of draft amplifier design and displacement results, the amplifier compliant mechanism cannot be used in this application.

With the elimination of the center conventional lens, the payload has been decreased and the structure was designed in order to obtain 7.5 micrometers subpixel displacement. Two alternative decouple and spring structures shown in Figure 4.5 have been designed and analyzed.

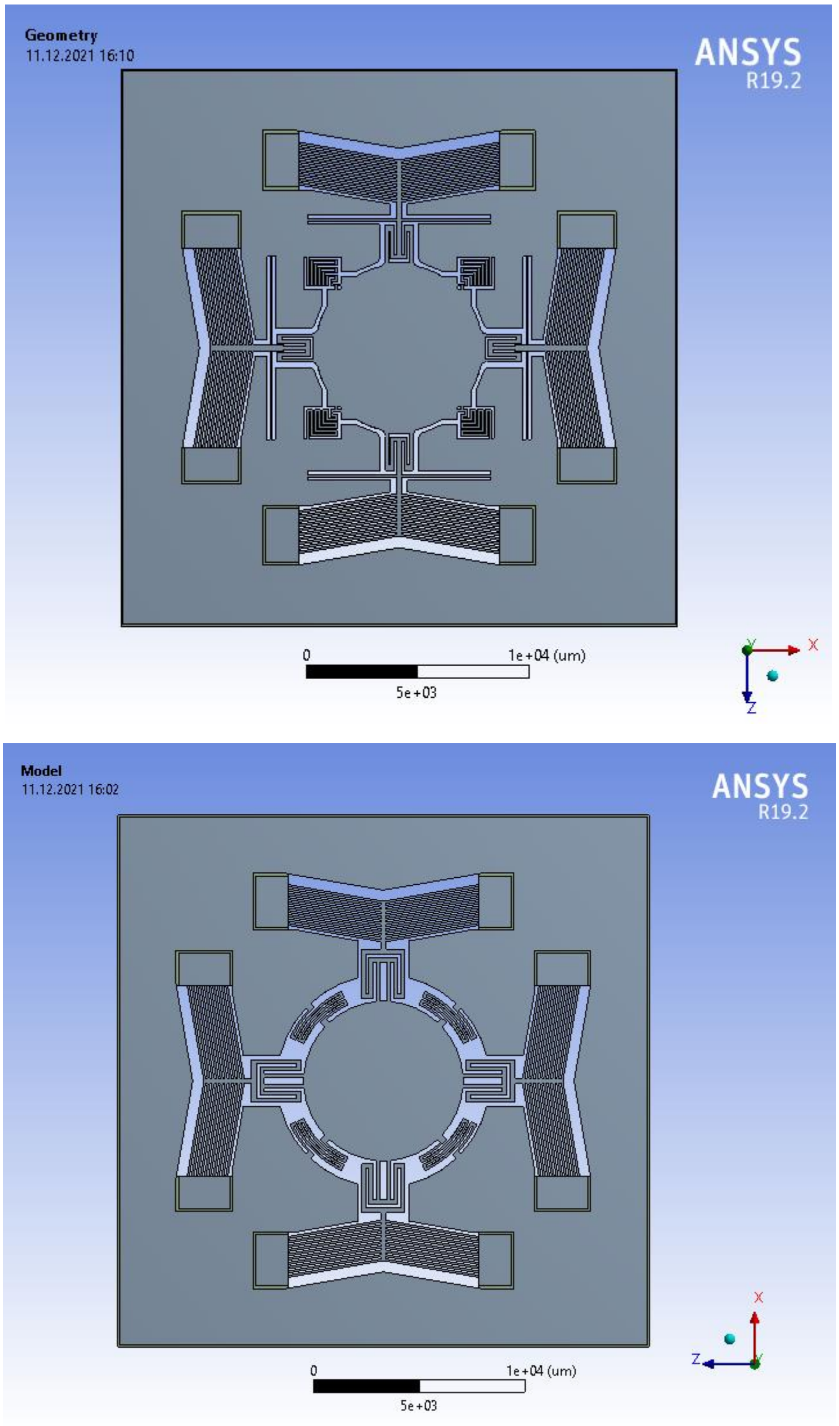

Figure 4.5 X-Y Scanning Design Alternatives

At the first design, there is a stiffener beam between the chevron and decouple structure. On the other hand, the second design does not have such a stiffener beam.

As seen from the Figure below, two axis spring design alternatives have been placed 45 degrees rotated to decouple structures.

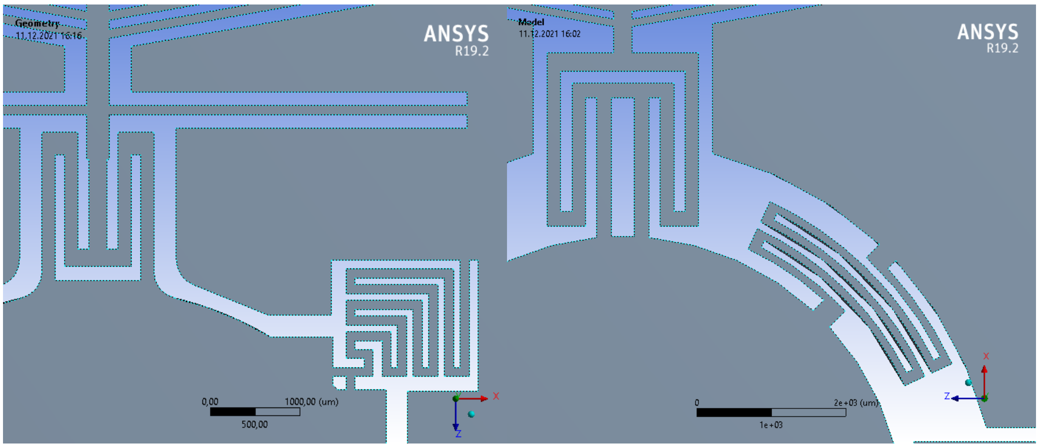

Figure 4.6 Two different decouple and spring structure alternatives

4.4. Displacement and Thermo-Electrical Analysis

Thermal-electric analysis has been performed by using the finite element method for specific boundary conditions. Convection film coefficient, radiation emissivity and ambient temperature has been taken as 2e-5 $W/mm^2 \cdot {}^0C$, 1, $22\ {}^0C$ respectively as boundary condition. Connections between layers defined as bonded and meshing has 51000 elements and 130000 nodes approximately.

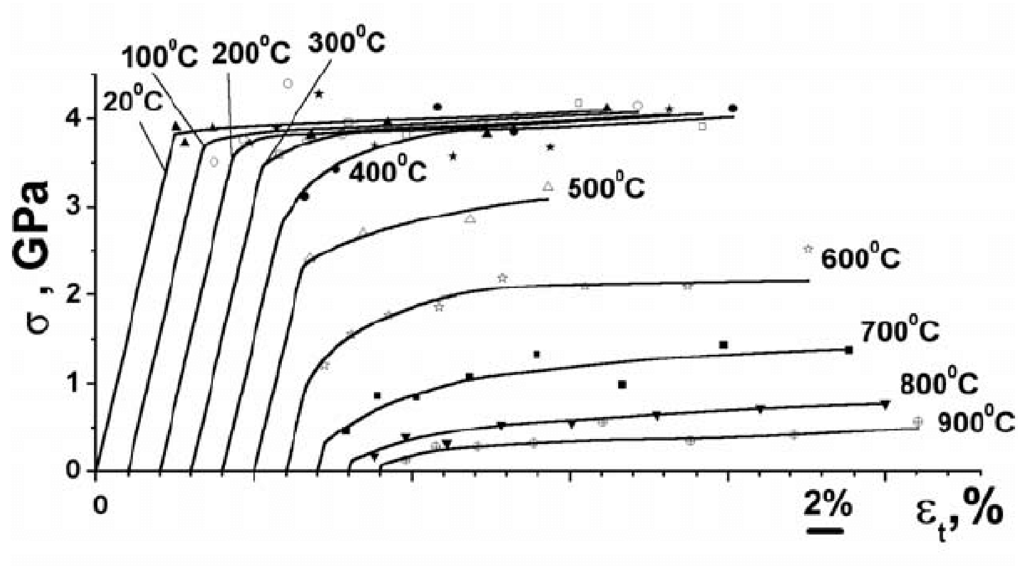

Figure 4.7 Stress–strain curves for single-crystal silicon at different temperatures under an indentation load P = 1.15 N. [50]

Single crystal Si is no longer brittle but ductile at high temperatures between 700 ^{0}C and 1200 ^{0}C. Material properties are tabulated at Table 4.2. Coefficient of thermal expansion of silicon material, shown in below graph at Figure 4.8, increases with high temperature. Indeed, the actual material properties of polysilicon depend on the deposition conditions. The elasticity property of silicon depends on crystal orientation like (100,110,111). The crystal orientation of SOI wafer used in this research is 111 so the elasticity of wafer was taken as isotropic at the FEM analysis.

Table 4.2. *Material Properties at Room Temperature (22 C^0)*

Material	*Modulus of Elasticity (GPa)*	*Density (kg/m^3)*	*Poisson Ratio*	*Coefficient of Thermal Expansion ($1/C^0$)*
Silicon Anisotropic	140	2330	0.3	Charted below
Silicon Dioxide	70	2170	0.15	Charted below
AL 6061	71	2770	0.28	2,3e-5

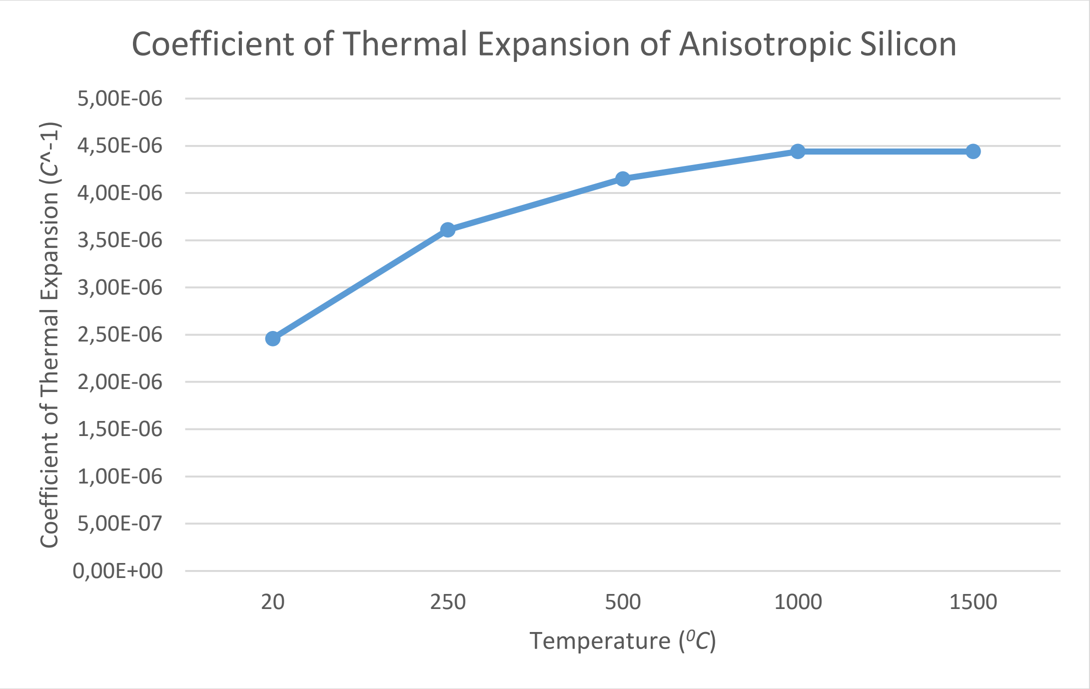

Figure 4.8 Coefficient of thermal expansion of Silicon at different temperatures

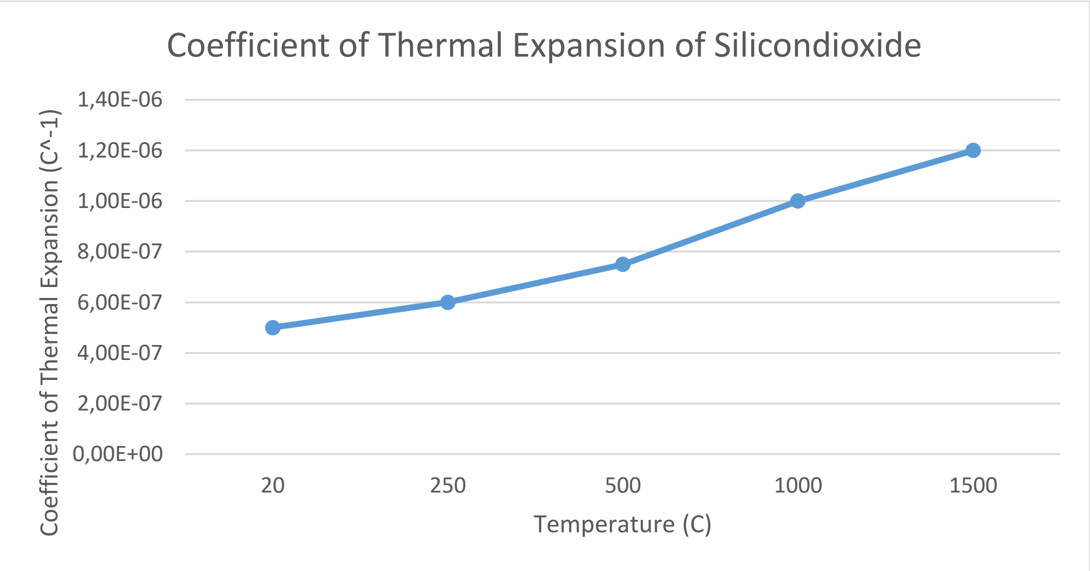

Figure 4.9 Coefficient of thermal expansion of Silicon dioxide at different temperatures

Voltage difference (*V*) has been applied to the contact region of chevron actuator zone as 4, 6, 8 V respectively. Table 4.3 indicates the analysis results where T_{max} *(C^0) and*

T_{center} are the maximum and center payload temperatures on the chevron actuator, t (sec) is the actuation time of single actuator, σ_p *(MPa)* is the maximum principal stress at actuation, $d(\mu m)$ is the directional displacement of payload.

Table 4.3. *Transient Thermo-Electrical Analysis Results of Design 1*

V	$D, \mu m$	t, sec	T_{max}, ^0C	T_{center}, ^0C	σ_p ,MPa
4	9.46	0.1	201.53	22.12	126.9
6	25	0.1	425.93	22.72	339
8	49.26	0.1	740	23.02	661
10	43.96	0.05	653.65	22.4	582.9
12	25.9	0.02	426.27	22.07	339

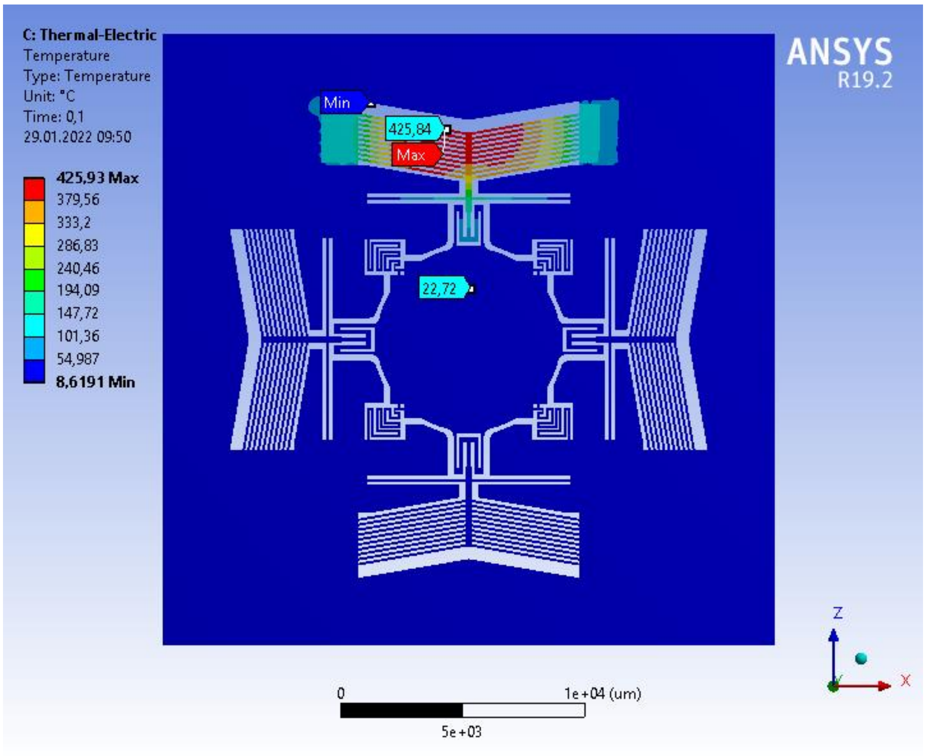

Figure 4.10 Temperature distribution of design 1 at actuation with 6V

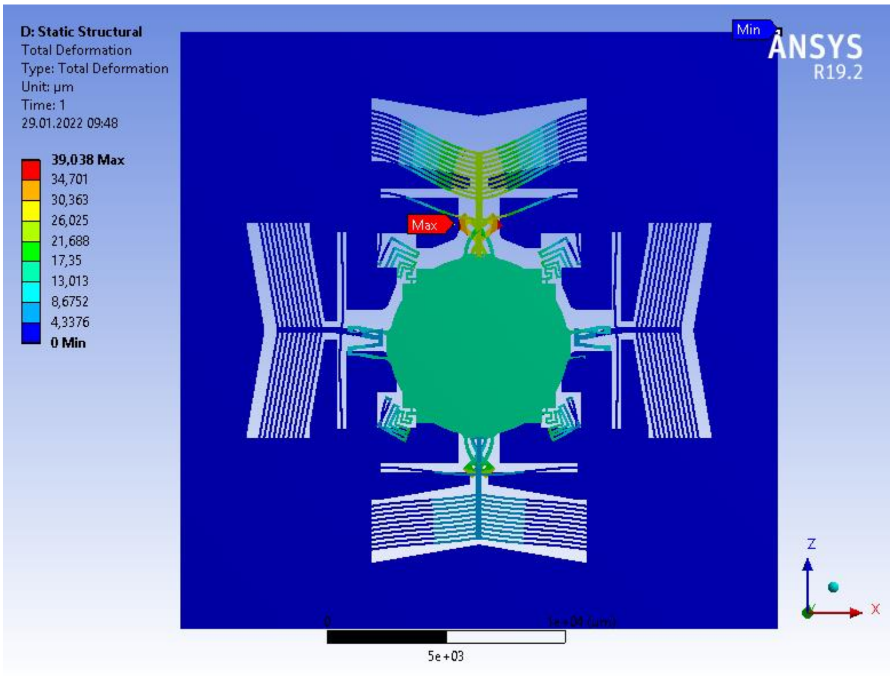

Figure 4.11 Total deformation of design 1 at actuation with 6V (Scale Factor=8)

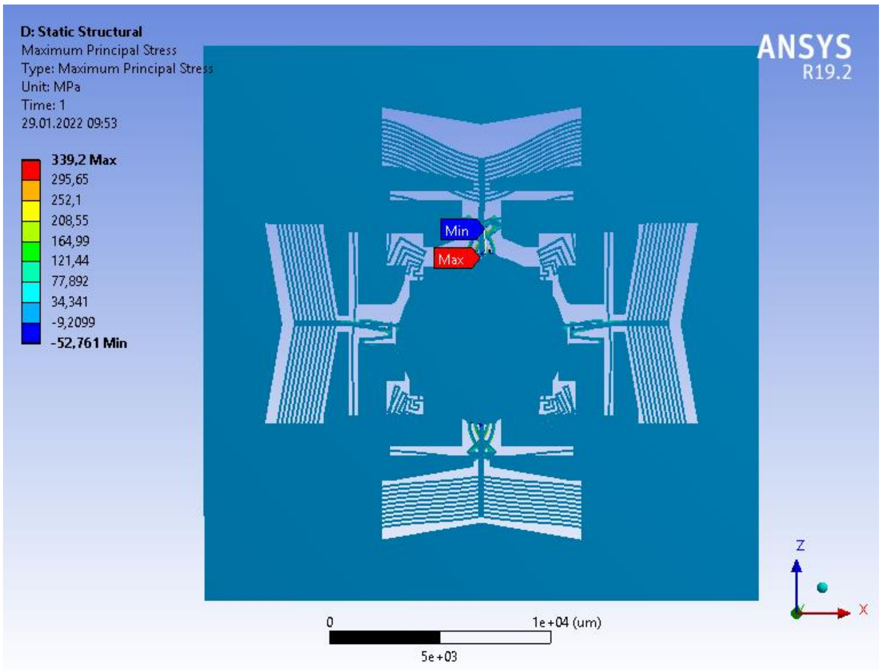

Figure 4.12 Maximum principal stress distribution of design 1 at actuation with 6V (Scale Factor=8)

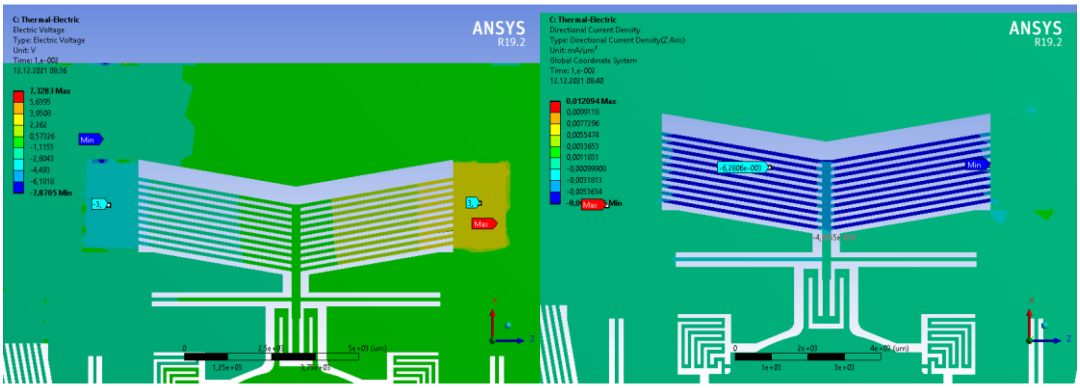

Figure 4.13 Electrical voltage distribution and directional current density at actuation

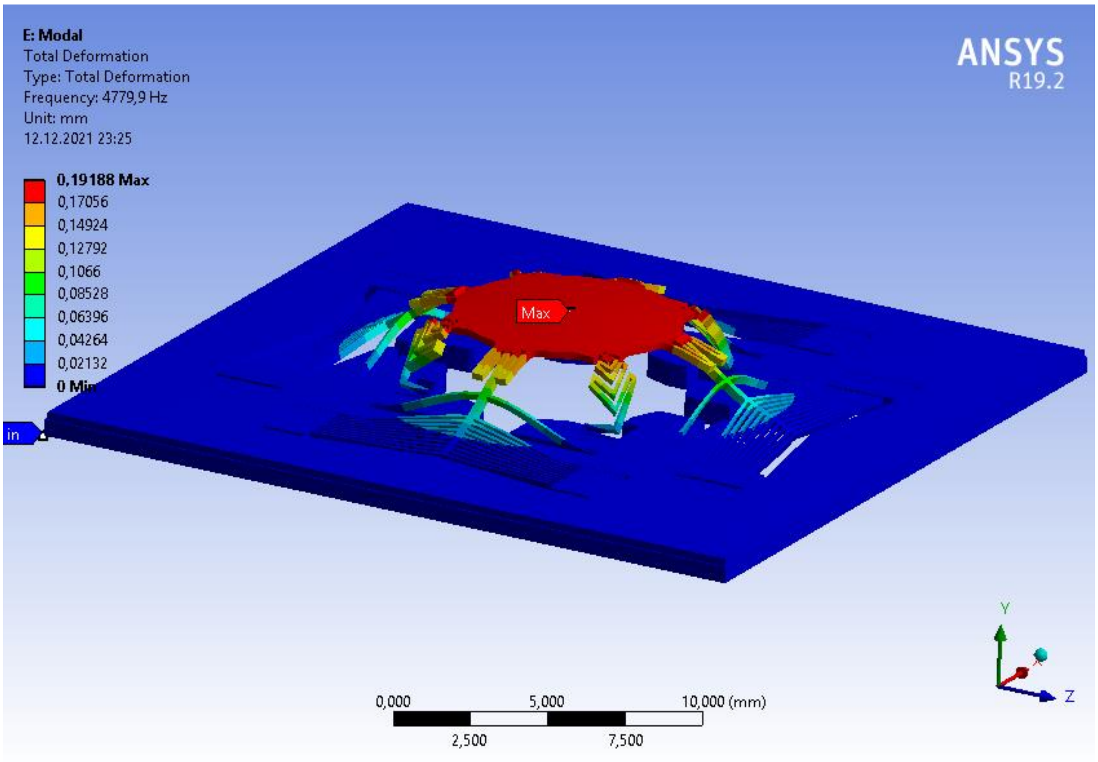

Figure 4.14 Natural frequency (4779 Hz) of alternative design 1

Table 4.4. *Modal Analysis Results*

Mode	*Frequency [Hz]*	
	Design 1	*Design 2*
1,	4779.9	3755.7
2,	8656.5	6852.5
3,	8773.1	6949.1
4,	9614.7	8494.4
5,	13941	9975.6
6,	13951	10020

When the results are evaluated, it seems that the maximum principal stress is much lower than young modulus of anisotropic silicon which is 140 GPa approximately. The minimum required displacement is 7,5 micrometers. The maximum stress usually occurs at the meandering part and the leaf springs. H. Kapels and R. Aigner defined the fracture strength of silicon in their research as 2.2 GPA for long time aging over 10^6 cycles of thermal actuator. This value is taken as the limit of fatigue failure for our thermal and electromagnetic actuators. As it can be seen that it is not so crucial because the maximum value is much smaller than the allowable yield stress and fracture strength. If the safety factor is taken as 2, the applied electrical voltage is extracted from Table 4.3 as 6 V to obtain 15 μm displacement. On the other hand, the maximum heating temperature under applied electrical voltage occurring in the chevron actuator zone is 553 C^0 which is acceptable for operation. Decouple performance, displacement at the vertical direction of actuation axis, is quite satisfying.

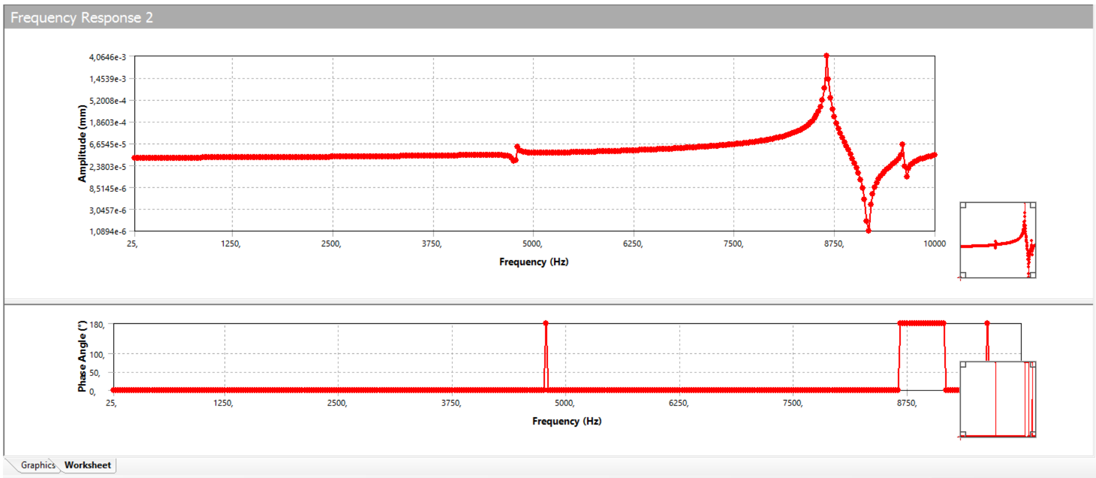

Figure 4.15 Harmonic analysis results of design 1

The first mode of modal analysis indicates the natural frequency which is 4779 Hz shown in Figure 4.15. Harmonic analysis was performed for actuation force and the results imply that the actuator responds the actuation force to the mode 1 frequency without any resonance.

The thermal-electrical and structural analysis have been performed for design alternative 2. The results for different applied voltages are indicated in Table below. Maximum stress of the design 2 is lower than the design 1 which is an advantage against long time failure of the structure.

Table 4.5. *Transient Thermal-Electrical Analysis Results of Design 2*

V	$D, \mu m$	t, sec	T_{max}, ^0C	T_{center}, ^0C	σ_p, MPa
6	25	0.1	421.81	26.09	175.49
8	49.03	0.1	732.77	32.74	341.99
10	45	0.05	672.08	28.06	308.36
12	27.86	0.02	468.83	25.49	229.4

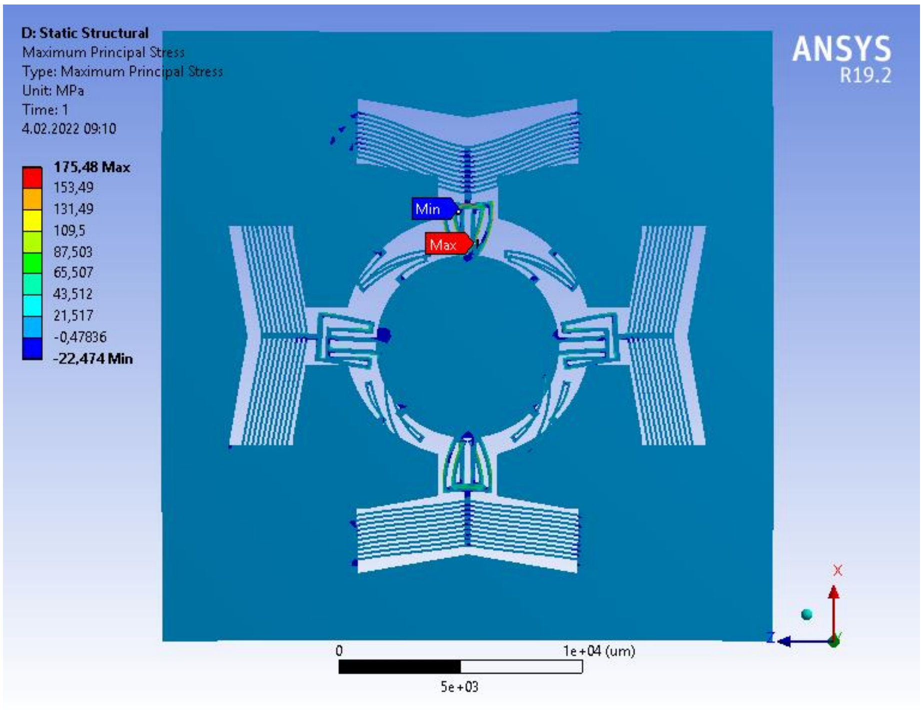

Figure 4.16 Maximum principal stress distribution of design 1 at actuation with 6V

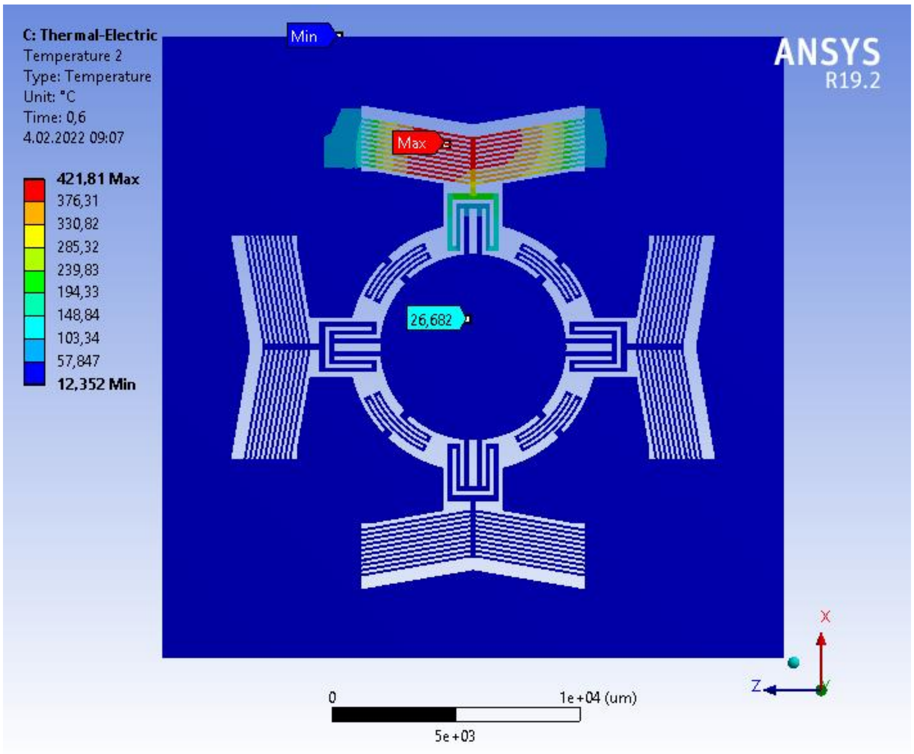

Figure 4.17 Temperature distribution of design 1 at actuation with 6V

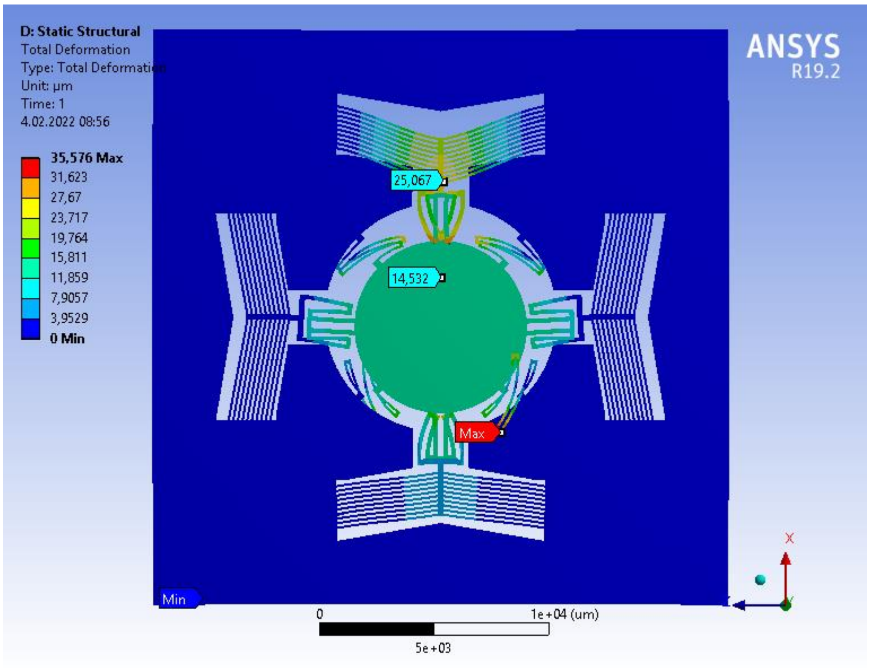

Figure 4.18 Total deformation of design 1 at actuation with 6V

Electrical voltage distribution and directional current density at actuation zone are similar with design 1 shown in the figure below.

All multi-physics analysis of both design 1 and 2 have been performed with the AL 6061 aluminum alloy holder part shown below by using the same contact type and boundary conditions.

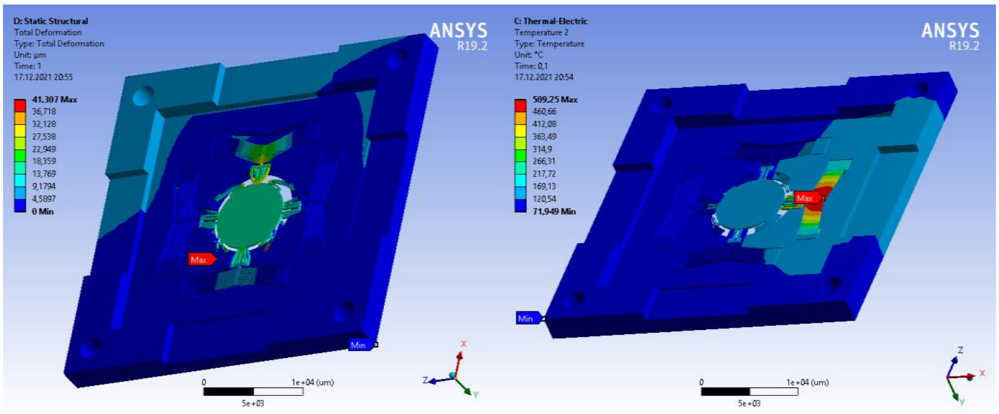

Figure 4.19 Analysis results with holder

4.5. The Fabrication of Updated Chevron Designs

Some production-oriented changes were made by METU-MEMS to the actuator structures. While producing the actuator and coded mask, any face of 1 silicon disc (with 100 µm and 400 µm cavities) was thought to be fabricated. The dimensions of the actuators frame were shortened by 1.5 mm from each side, without touching the actuating parts of the sensor so that 10 actuators can be fitted on a 4-inch wafer instead of 6 actuators. In the layout file, a 50 micron thick dummy structure was added to the middle of the spring supporting the middle in design 1. In design 1, the rear part of the actuators, between the actuators and the spring, and around the springs connecting the middle to the anchor were filled to ensure uniformity of etching.

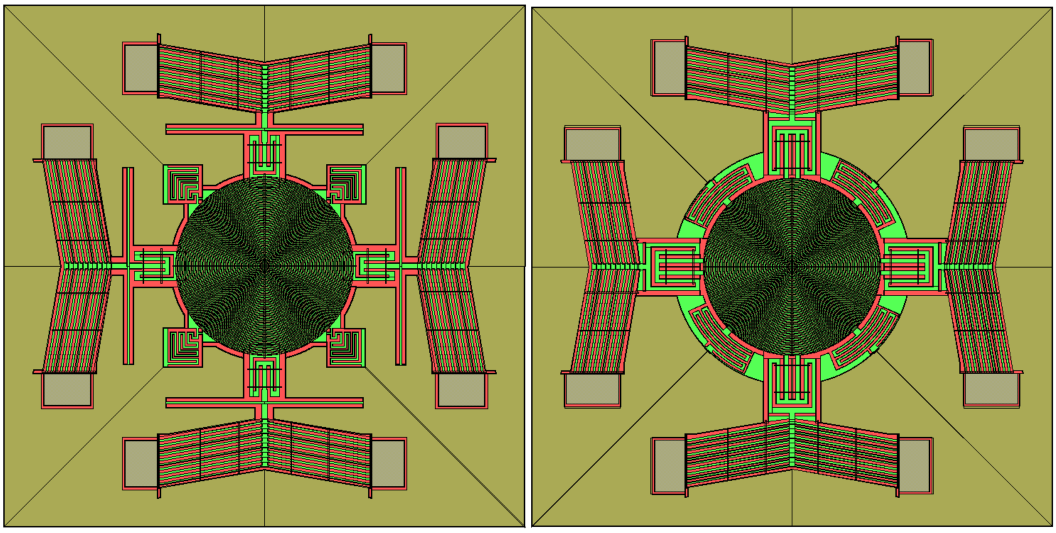

Figure 4.20 Mask layout of design alternative 1 and 2

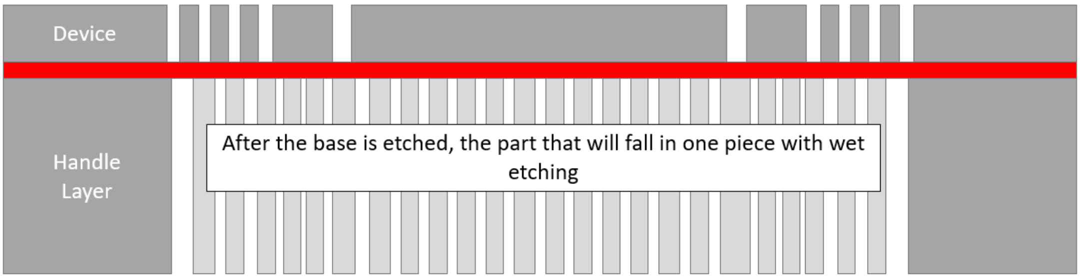

Figure 4.21 Support cross section

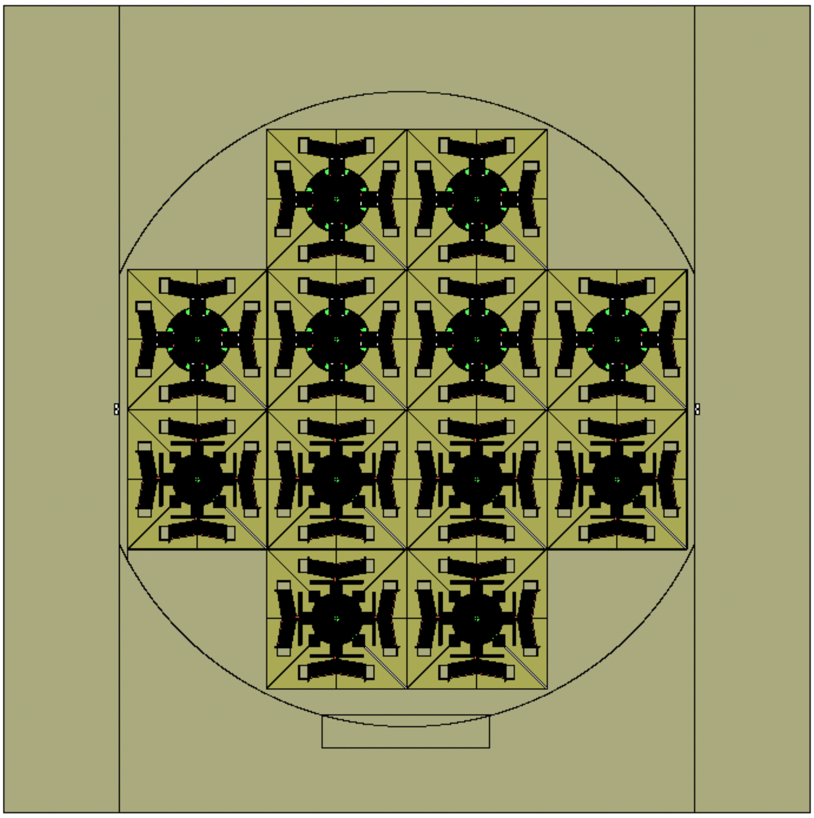

Figure 4.22 4 Inch SOI wafer mask layout of design alternative 1 and 2

After the wafer level fabrication, each actuator module was separated by using Dicers.

Table 4.6. *Properties of Silicon on Insulator (SOI)*

SOI Properties		*Handle Layer*	*Device Layer*
Size (mm)	100+/-2		
Buried Oxide Thickness (μm)	2		
Type-Dopant		P/B	P/B
Orientation		<1-1-1>	<1-1-1>
Thickness (um)		100+/-5	400+/-10
Resistivity (ohm-cm)		<.005	<.005

Gold (Au) is a good conductor and reflects visible, mid wave and long wave infrared wavelengths; therefore, it is perfect choice for the contact and coded mask layer. The gold layer was patterned by wet etching. The minimum feature size of coded gold mask is 2.5 μm.

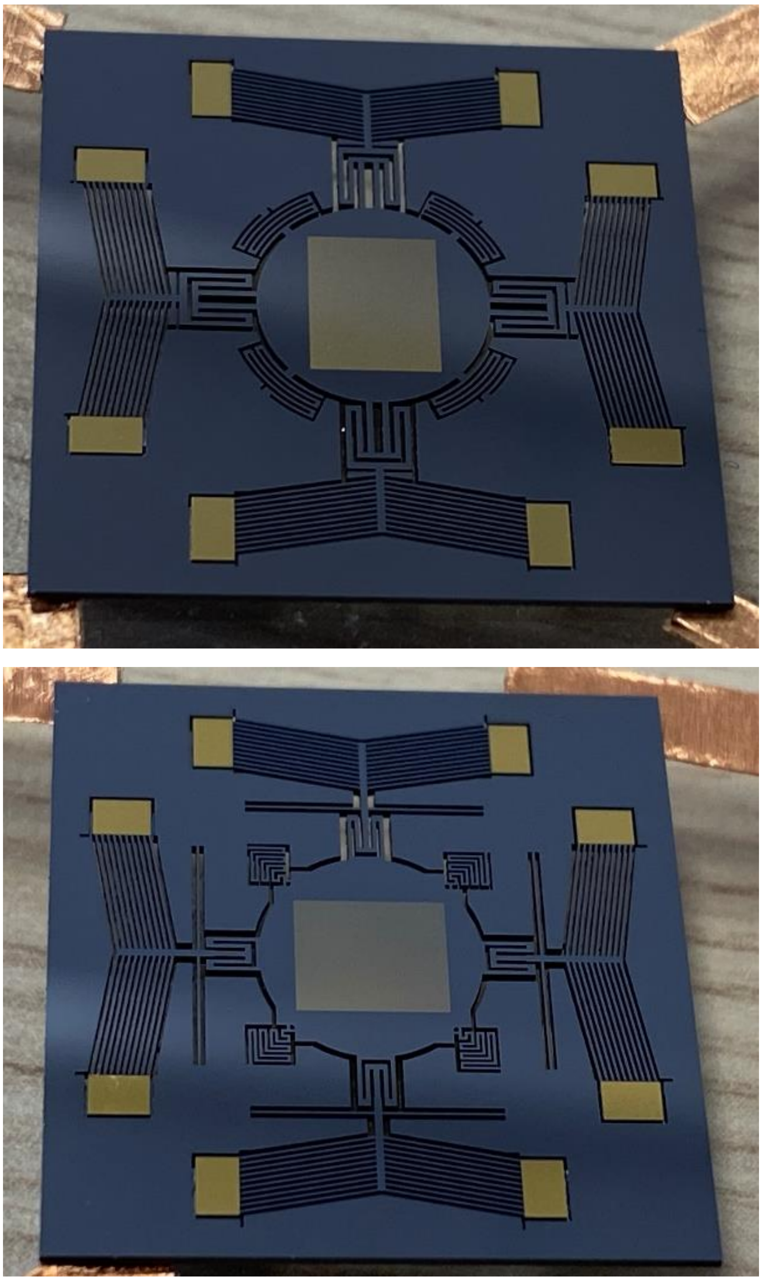

Figure 4.23 Actuator prototype 1 and 2.

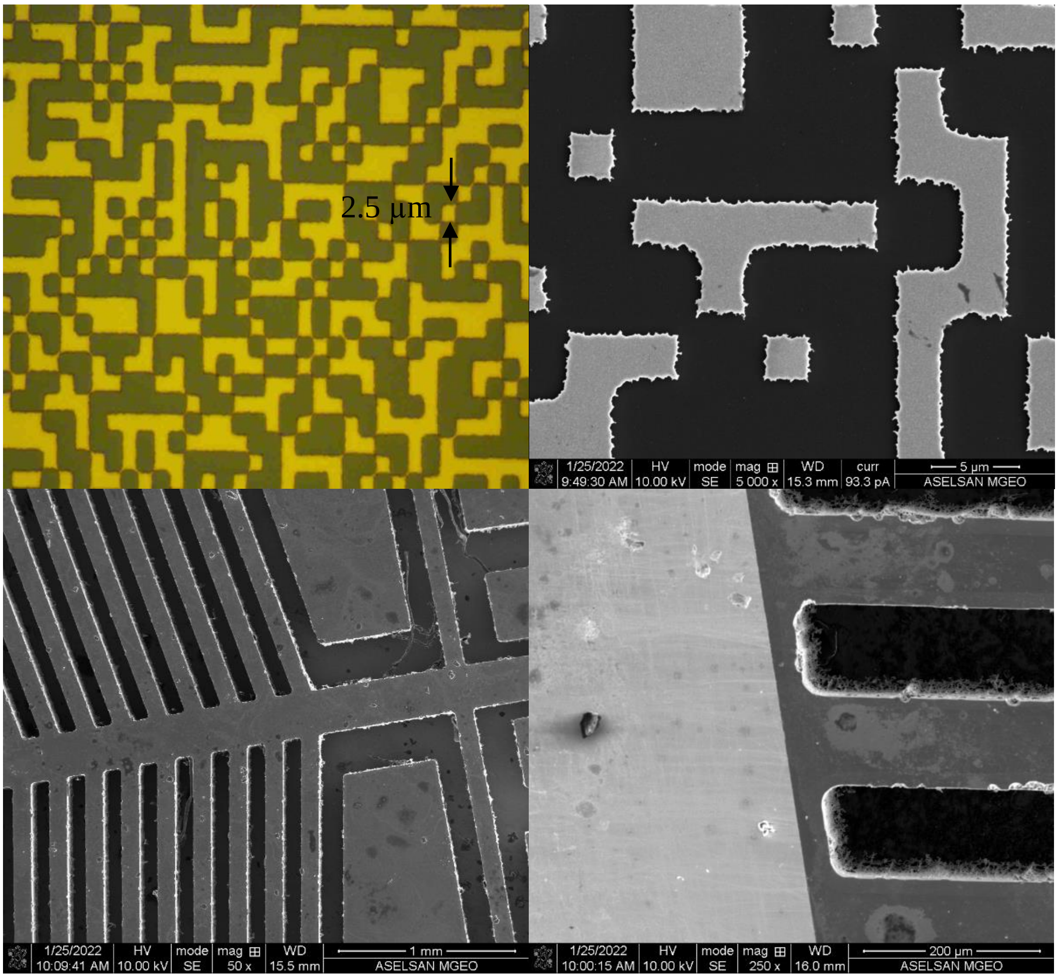

Figure 4.24 Microscope and SEM images of coded mask and actuator features.

Packaging and wire bonding are the next step of fabrication. Aluminum alloy 6061 is the material of the packaging part holding the contact boards. The actuator was bonded to the packaging part by using Silver (Ag) based epoxy adhesive that is frequently used at MEMS systems. Adhesive was cured at 80 C^0 for 3 hours.

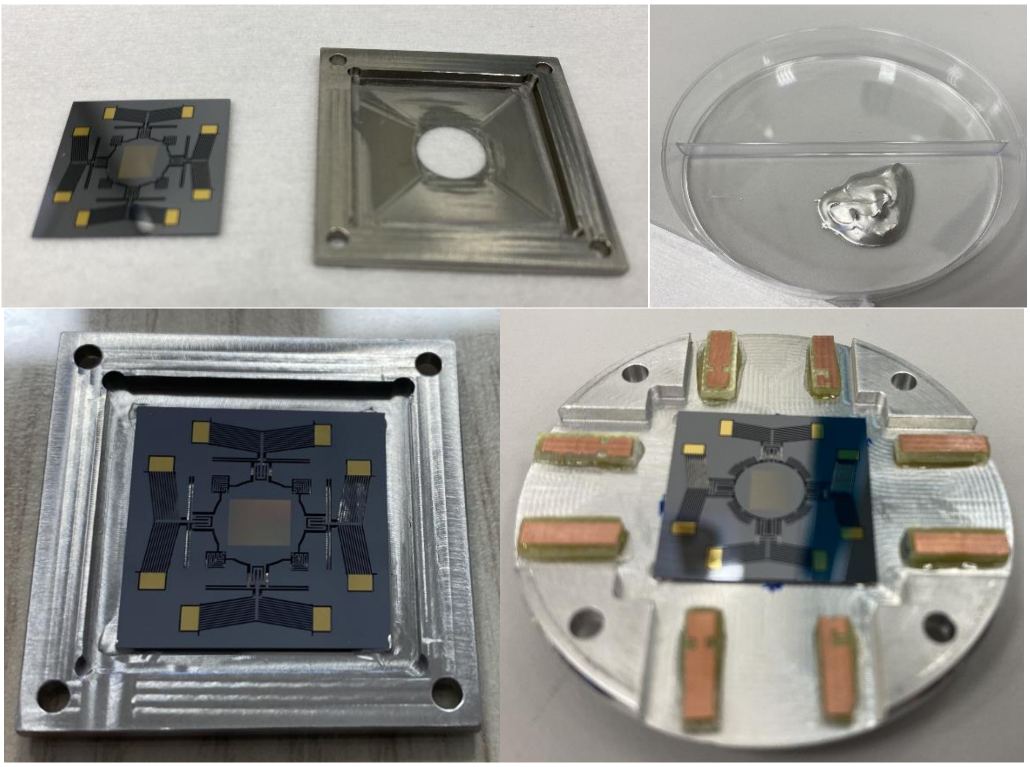

Figure 4.25 Actuator design alternative 1 and 2.

In order to increase the current carrying capacity, the maximum number of wire bonding that can fit in the contact area has been tried to be made. Each 1 mils diameter (0.0254 mm) gold ball-bonded wire is capable of approximately 1 Ampere of electrical current per wire.

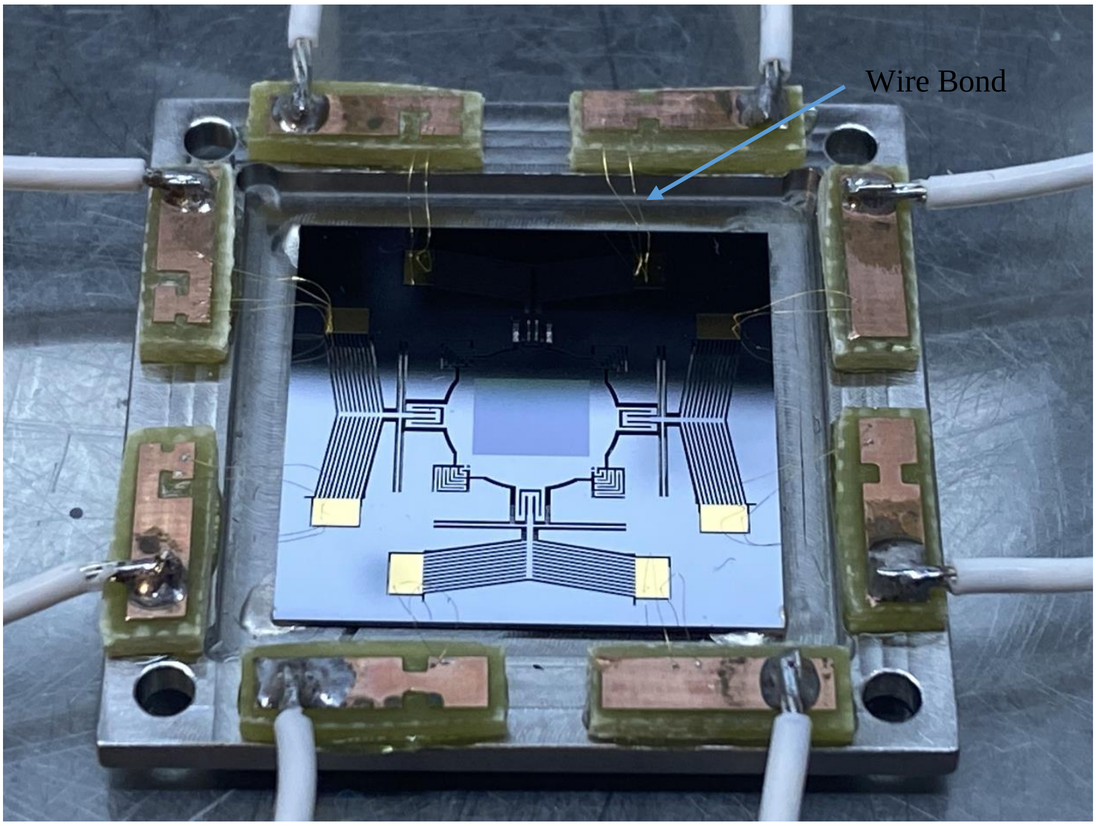

Figure 4.26 Actuator design alternative 1 with wire bonding and cabling.

4.6. The Displacement Test of the Actuator Package

The actuator package was placed to the probe station to observe the displacement under excitation voltage via microscope. Displacement tests were performed for different voltages. Meanwhile, the temperature of actuator was measured with a Fluke Infrared Camera. A microscope was zoomed in to the actuator arm and the actuation motion was captured. The length of one pixel (l_{px}=3.42 μm) is able to be calculated from a feature whose length is known. Images of power on and off positions were inspected and the displacement can be calculated from pixel shift. Blue and red horizontal lines in the following figure demonstrate the power off reference position and displacement under excitation voltage, respectively.

Figure 4.27 Displacement test equipment

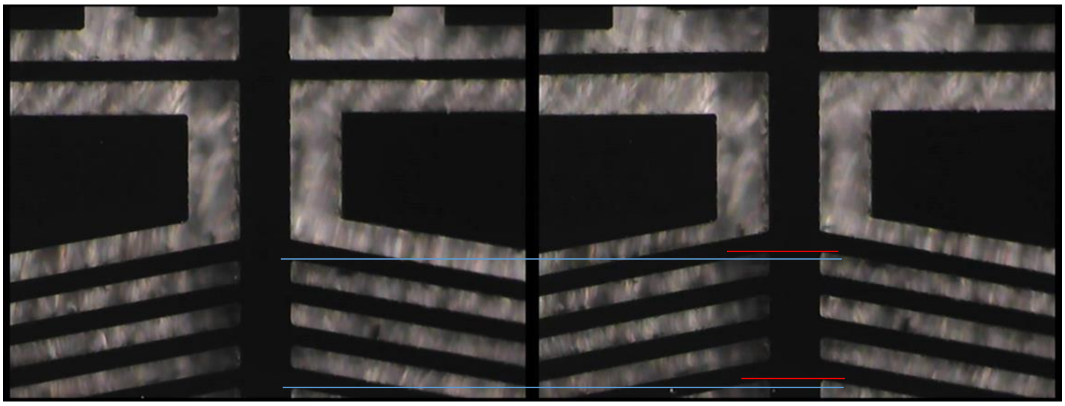

Figure 4.28 a) Power off and b) Power on microscope images of actuator center

To show and calculate the displacement, the differences in power off and on frames were extracted, registered and merged in a single image by changing the color of pixels with position changes in Matlab. The green colored pixels in Figure 4.29 show the displacement of actuator under 11V excitation voltage. As can be seen from the image, the displacement zone indicated by green color did not occur in the parts that remained fixed. This shows that only the actuator region was displaced.

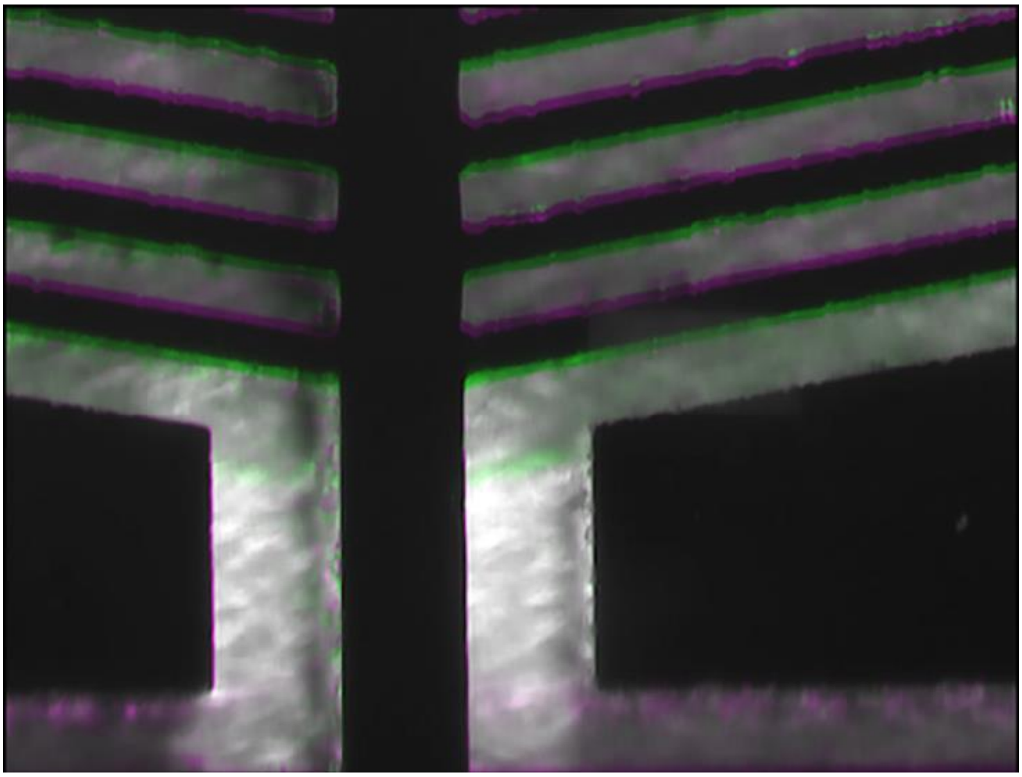

Figure 4.29 Power off and on merged image under 11V excitation

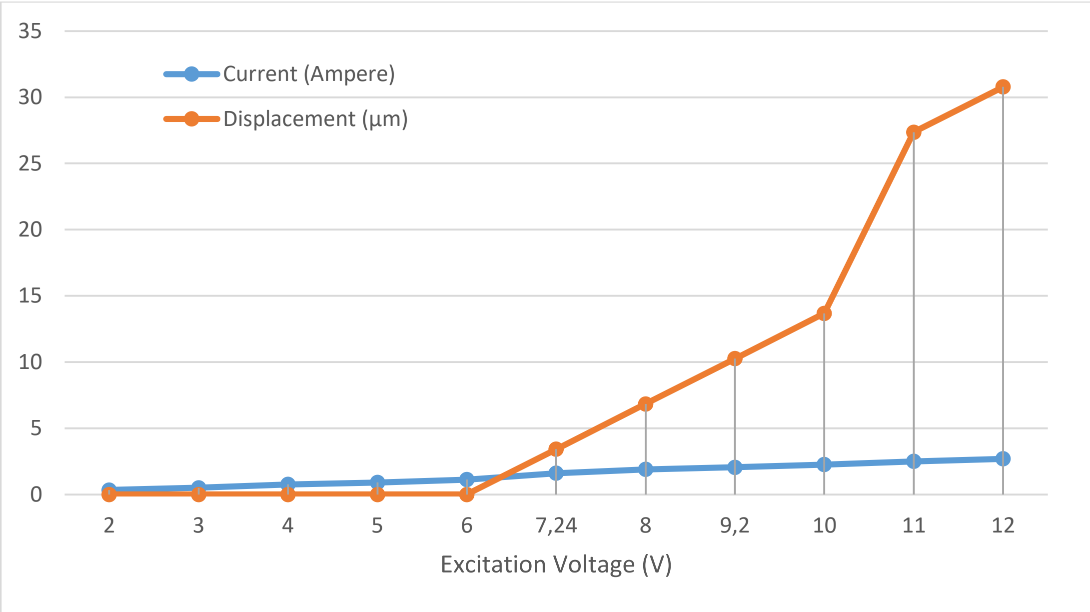

Figure 4.30 Tip displacements and currents of the design alternative 1 at different excitation voltages.

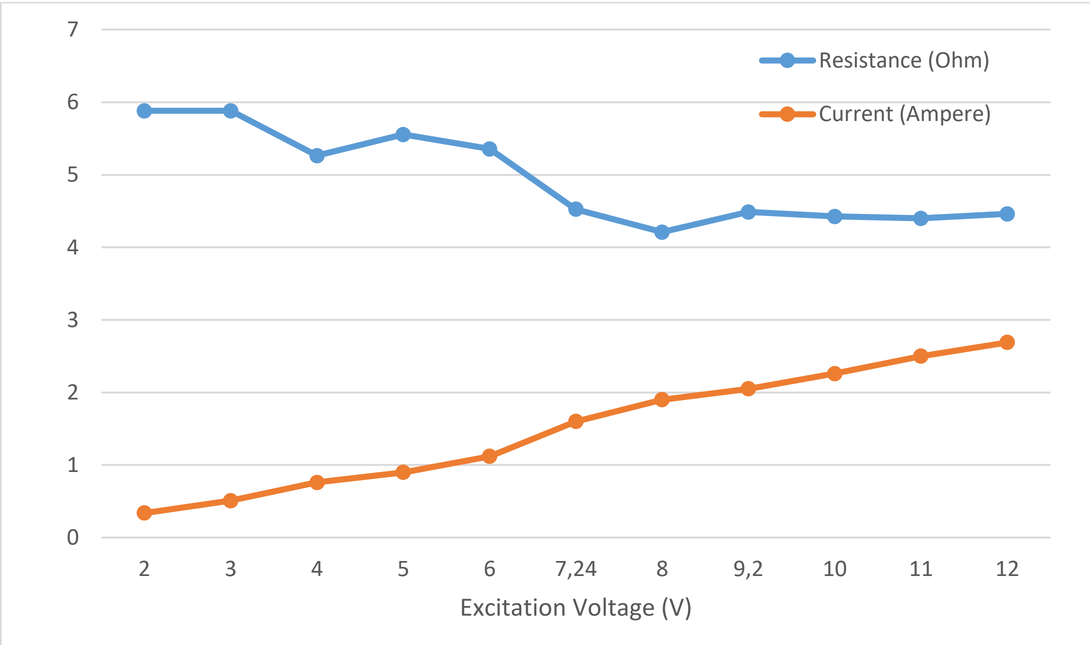

Figure 4.31 Resistance of single chevron actuator versus applied current.

The resistance and current graphs indicate that there is no sudden drop in resistance and increase in the current which means that the actuator is at steady state under excitation voltage. Considering the results of the old design, the voltage applied to obtain the required displacement caused a large increase in the electrical current and a large decrease in resistance, which created a significant amount of heat and put the silicon material in the high temperature unstable region. The material changes its properties at high temperatures and changes from brittle to ductile, and in this case the desired elongation efficiency from the material cannot be obtained. The high temperature of the actuator also delays the cooling and therefore prevents scanning at the desired frequency. In the temperature measurements made with the new design, it was seen that this problem was solved and the material remained in a stable regime at the desired elongations. With the new optical architecture, both the optical unit size and the required displacement has been reduced. In this way, a smaller actuator could be designed and the desired displacement was achieved and the material could be kept in the stable region.

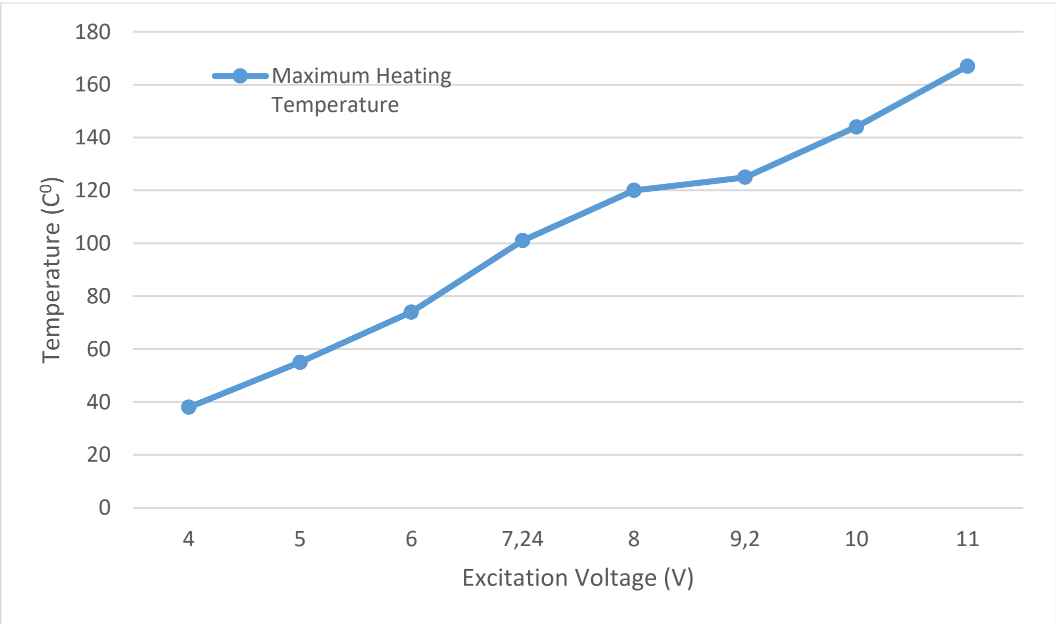

Figure 4.32 Maximum heating temperature of single chevron actuator versus applied current.

When the analysis results are compared with the test results, a difference is seen between the applied voltage and the displacement obtained. After detailed examination, the SOI resistivity, which was taken as 0.005 ohm/cm according to the data sheet, was evaluated to be higher than it should be. In order to understand how high it was, resistance measurement was made from the device layer by using a multimeter. In addition, the resistivity value was changed to bring the results obtained from the analysis closer to the test results. When it was 0.03 ohm/cm approximately, it has been observed that the excitation voltage and displacement results at test and analysis overlapped for high voltage and heating. The resistivity has been decreasing with increasing temperature. It has been considered that fabrication processes and temperature change are effective in changing the resistivity value.

Table 4.7. *Thermo-Electrical analysis and test results of design 1 for different resistivity*

Resistivity (0,005 ohm.cm)		*Resistivity (0,03 ohm.cm)*		*Test Results*	
V	*D,μm*	*V*	*D,μm*	*V*	*D,μm*
4	9.46	6	6.02	6	0-3.42
6	25	8	12.67	8	6.8
8	49.26	11	27.17	11	27.36

The current according to the applied voltage was measured as shown in Figure 4.31 and the resistance was calculated. When the resistivity was calculated from the resistance values according to the equation below, it was confirmed again that it was higher than the values specified in the data sheet. Finite element analyses were repeated using different resistivity values at each voltage value according to the calculated resistivity values.

$$\rho = R\frac{A}{l} \tag{38}$$

where R is the electrical resistance of a uniform specimen of the material, l is the length of the actuator, A is the cross-sectional area of the actuator.

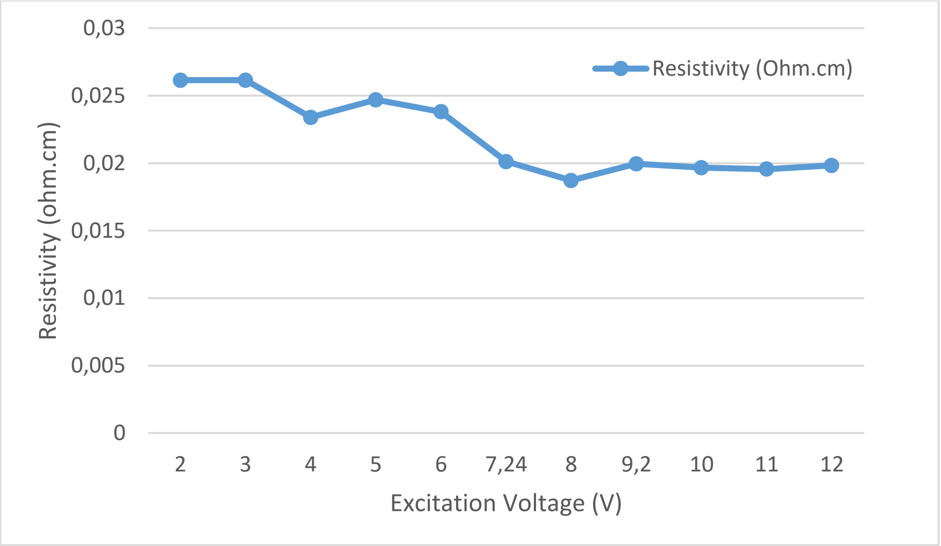

Figure 4.33 Resistivity change with respect to the excitation voltage

In the probe station tests, when a voltage of 13 Volts and above is applied, material burning occurred in the chevron actuator contact areas and conductivity was lost. When the source of the error was examined, it was seen that the gold thickness in the contact area was not sufficient and the chrome bonding layer did not provide sufficient adhesion. For this reason, it is considered that no successful results can be obtained from wire bonding and ribbon bonding trials. In addition, it was concluded that due to this situation, sufficient conductivity was not formed in the contact areas and the application voltages were higher than expected.

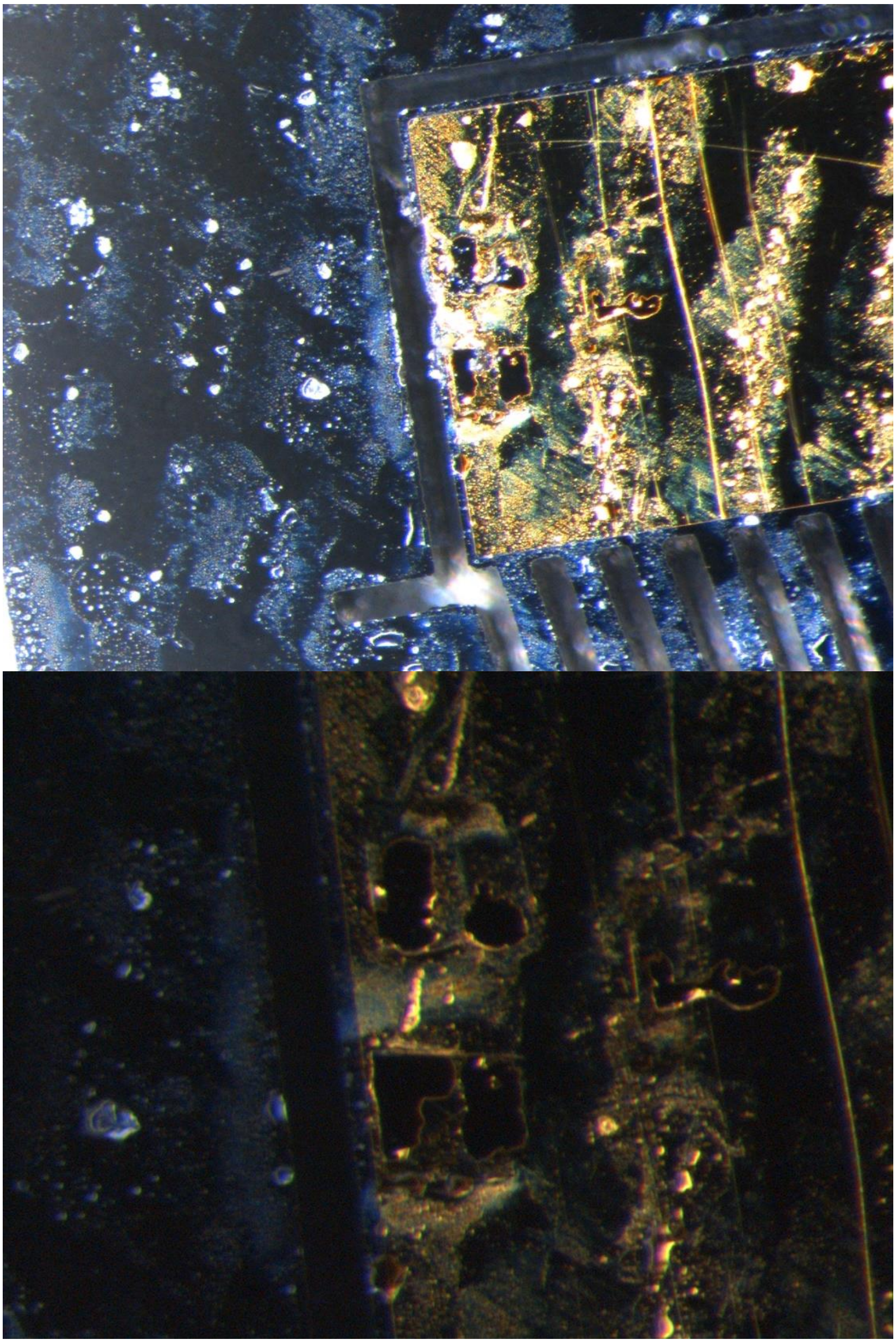

Figure 4.34 Au layer peel off at ribbon wire bonding

4.7. The Position Control Method of Actuation

Open and close loop control of the actuator is possible for precise motion control. The image of coded mask occurs on FPA so that motion of coded mask can be tracked by processing the image to observe closed loop control. To discriminate the function of positioning and resolution enhancement, special patterns were embedded to the coded mask so that the image processing algorithm is able to check the motion and feedforward position to the controller of the actuator. This control method gives many advantages like the elimination of additional position sensors on actuator, simplifying the system and size reduction. The flow chart below defines the image reconstruction and control loop briefly.

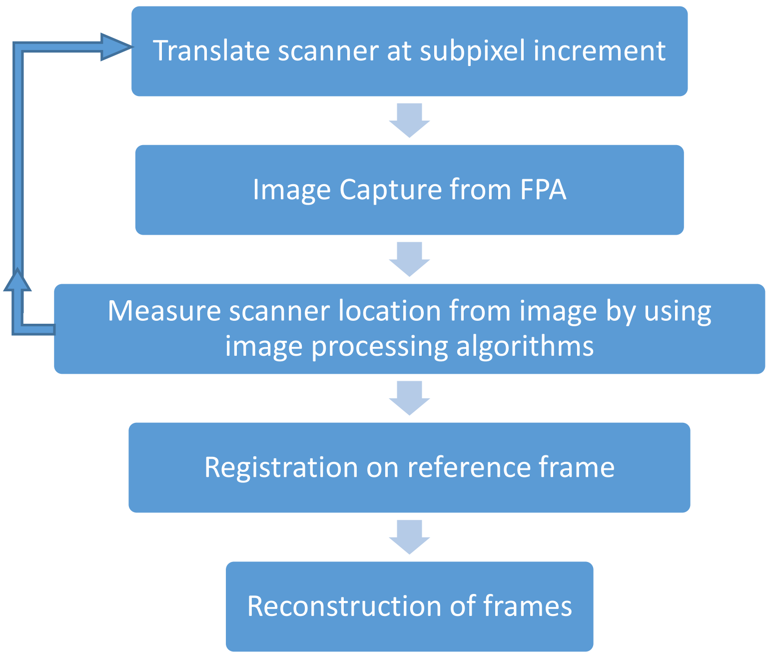

Figure 4.35 Position control and image reconstruction flow chart

CHAPTER 5

DESIGN OF AN ELECTRO MAGNETIC MOEMS MICROSCANNER WITH INTEGRATED METALENS FOR RESOLUTION ENHANCEMENT AND STABILIZATION

In this chapter, the electromagnetic MEMS actuator is evaluated in order to achieve higher displacement and lower excitation voltage than an electro thermal actuator with replacing the coded mask with a metalens doublet. A metalens doublet consists of two metasurfaces subwavelength diffractive nanoholes. One of the metalenses is scanned translationally. The other one, used for reducing the chromatic aberration and focusing to the internal image plane, is fixed. The most important performance parameters, mechanical and electrical features of electromagnetic MOEMS actuator are described in detailed. In additionally, the metalens theory and a novel optical layout for metalens implementation in macro level imaging system are indicated.

5.1. An Overview of a MEMS Based Electro Magnetic Actuator

At the chapter 3, the advantages and disadvantages of the MEMS based actuator types are defined briefly. The Main advantage of a MEMS based electromagnetic actuator is lower heating than the thermal chevron, if the conduction layer can be coated at proper thickness. If large displacement and high force are needed, high heating and thermal management of chevron become difficult problems to solve.

With that perspective, the complicated fabrication and additional magnetic field necessity of electromagnetic actuator become acceptable to take the advantage like low heating, easy thermal management, reasonable power consumption, high displacement and force. The excitation force of a magnetic actuator is generated by the Lorentz force resulting from the interaction of an electric field and a magnetic field. The magnetic field is perpendicular to the current for generating the force through the other perpendicular direction. Current passes through non-magnetic material to eliminate magnetic hysteresis.

5.2. The Theory and Working Principle of an Electro Magnetic Actuator

Both the electric field and magnetic field can be defined from the Lorentz force law. The electric force is straightforward, being in the direction of the electric field if the charge q is positive, but the direction of the magnetic part of the force is given by the right hand rule. The force is perpendicular to both the velocity $\vec{v}$ of the charge q and the magnetic field $\vec{B}$. $\vec{E}$ is the electric field.

$$\vec{F}_{total} = \vec{F}_{electrical} + \vec{F}_{magnetic} = q\vec{E} + q\vec{v} \times \vec{B} \tag{39}$$

$$\vec{F}_{magnetic} = q\vec{v} \times \vec{B} \tag{40}$$

When the magnetic force relationship is applied to a current-carrying wire, the right-hand rule is used to determine the direction of force on the wire. The Lorentz force on wire can be expressed as

$$\vec{F}_{magnetic} = I\vec{L} \times \vec{B} = BIL\sin\theta \tag{41}$$

where B (Tesla, Newtons per Ampere meter) is the magnetic flux density of the magnetic field , I (Ampere) is the current flowing through the beam, L (meter) is the beam length, and θ is the angle between the current and the magnetic field which is 90 degree here.

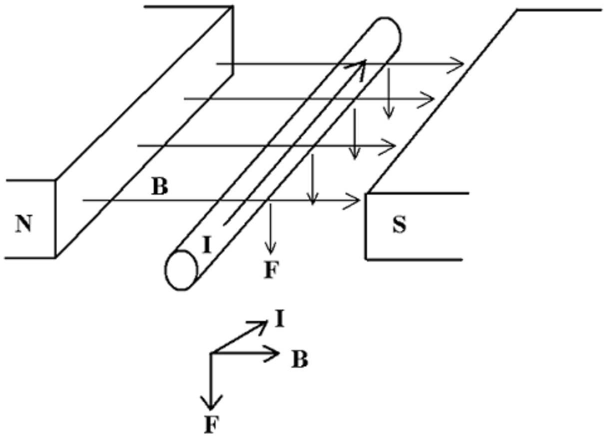

Figure 5.1 Lorentz Force Schematic

The actuator consists of a set of simply supported beam which is obtained by adding two U-shaped flexure Sections at the end of fixed end supported beam to enhance the lateral movement.

The Lorentz force generated deforms the beam elastically and the magnitude of deformation is related with the spring constant of beam. The spring constant k of beam depends on the geometry and material properties of beam structure.

$$\vec{F}_d = k \cdot y \tag{42}$$

$$\vec{F}_d = k \cdot y = BIL \tag{43}$$

At the equilibrium state, displacement y of the beam can be calculated by

$$y = \frac{BIL}{k} \tag{44}$$

To achieve large displacement, numerator of the equation shall be increased by increasing the magnetic field, applied current and length of beam and also denominator shall be decreased by reducing the spring constant of single beam structure. To increase the total force, the number of the beam can be increased and the current passing through each beam has to be electrically isolated by masking. These are the key optimization parameters of the design of a magnetic actuator.

5.3. The Metalens Theory and Optical Architecture of the System

The transition from conventional components to flat optics in optical technologies has accelerated with the development of micro and nanofabrication methods and capability of electromagnetic analyzes in the finite difference time domain. Macro optics are designed and validated using ray theory, but wave theory is used in flat optics and there are micro and nano structures on the surfaces that will change the phase of the light other than bulky spherical or aspherical shapes. Metasurfaces are used for these surfaces and metalens definition is used for lenses. The biggest advantage of flat optics will be the reduction of optical systems in terms of volume and weight. In 2021, Samsung received a patent for a mobile phone camera lens consisting of metalenses.

The most important advantages of our application in terms of meta lens are that the actuator is made of semiconductor silicon material, which is also permeable at certain infrared wavelengths, and the use of micro and nanofabrication methods for production. There is also the potential to achieve the optical performance that can be achieved with a few conventional curved lenses with a metalens. For these reasons, a metalens was designed to be placed in the center of the actuator. This approach can be used for different purposes from different optical architectures.

So far, researchers have struggled to design metalenses that provide broadband imaging, high numerical aperture. Especially with the recent developments, this has become possible. Ansys, the most important software producing multiphysics solutions, acquired Lumerical, which specializes in FDTD analysis in 2019, and then Zemax OpticStudio, the leader of the optical design software market, in 2021. In this case, macro and micro optics design activities are combined in a single platform. The figure below indicates the process of metalens design from micro to the macro level.

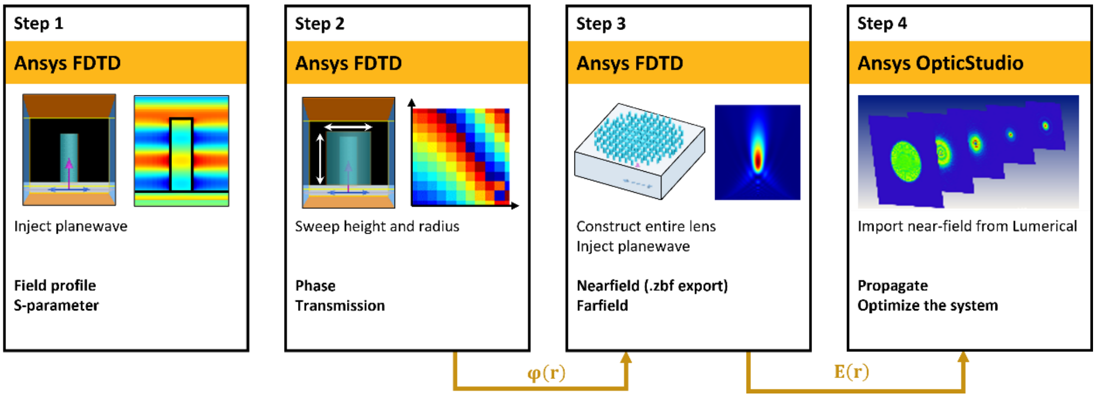

Figure 5.2 Process flow of metalens design[58]

For a hyperbolic lens;

$$\vartheta(x,y) = \frac{2\pi}{\lambda}.(f - \sqrt{f^2 + x^2 + y^2}) \tag{45}$$

where ϑ is the phase on the metalens surface, f is the focal length, x, y is the spatial coordinates with respect to the center of the lens, λ is the wavelength of system.

For a cylindrical lens;

$$\vartheta(x,y) = \frac{2\pi}{\lambda}.(f - \sqrt{f^2 + r^2}) \tag{46}$$

where r is the distance to the metasurface center.

As it can be seen from formulation that phase formulation has single wavelength input. For multi wavelength achromatic design, the equation should be solved for all wavelength. The primary geometries are nanohole and nanopillar. The metalens design starts with unit cell design. Unit cell consists of 2D array of nanorods or pillar having changing height or radius with respect to the height. Focusing efficiency is another critical parameter of the metalens performance.

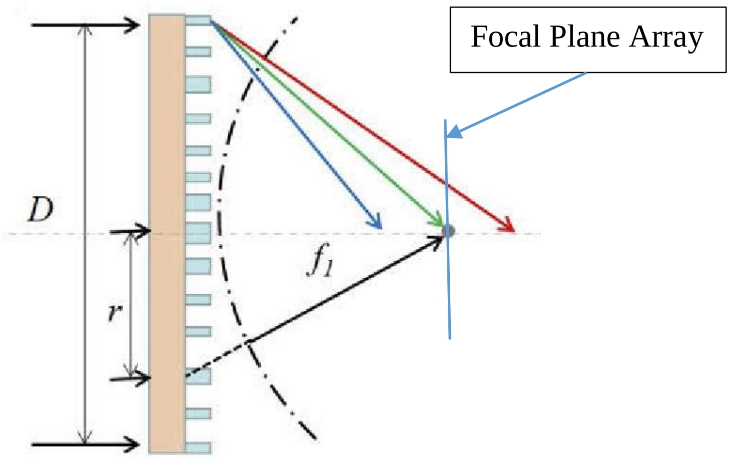

Figure 5.3 Optical layout of single metalens

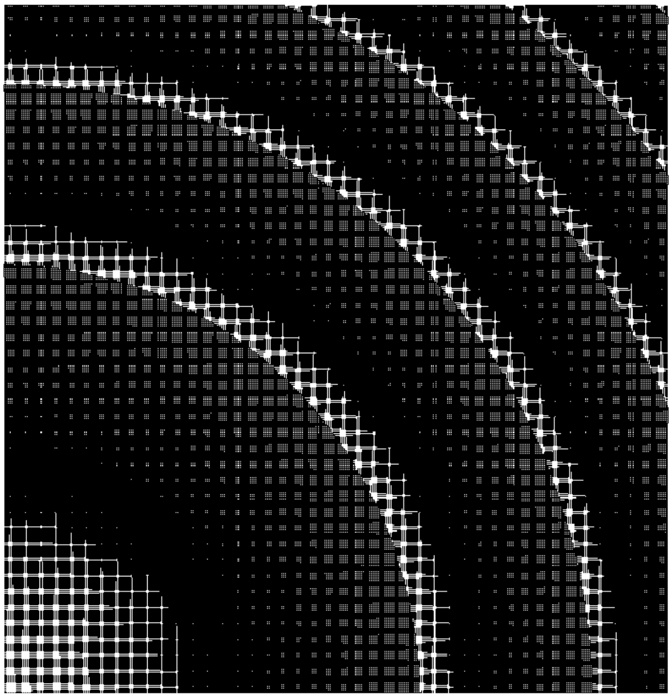

Figure 5.4 Metalens nanohole distribution

If two metalenses, 1x magnification telecentric imager group, is placed to the optical layout after internal image plane and the one or two metalenses are decentered at subpixel distance, the beam is steered through the displacement of metalens. This case gives the opportunity to achieve resolution enhancement by microscanning and also optical stabilization within a small package. The metalens can be changed with a microlens but it brings additional micro lens manufacturing steps. The main advantage of using a metalens is that it is fully compatible with the actuator fabrication process. The figure indicates the paraxial bi-telecentric imager group working at midwave infrared wavelength (3-5 μm) and having 4 mm object and image height. The aperture stop is at the middle of metalenses.

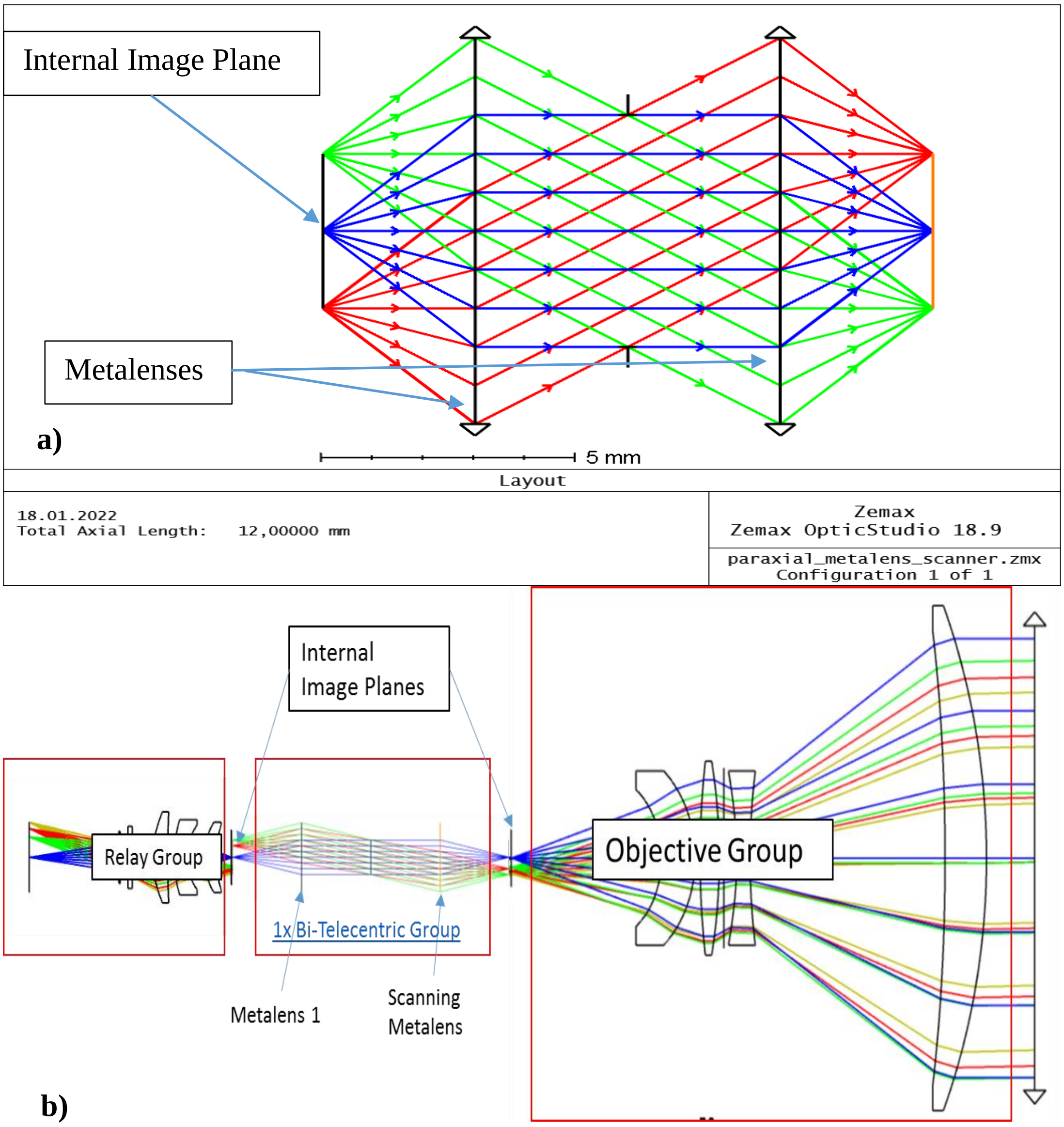

Figure 5.5 Optical layout of metalens (a) bi-telecentric imager group and (b) system

5.4. The Structural Design, Analysis and Optimization of a Magnetic Actuator

A significant design target of actuator for an microscanning and stabilization of a MWIR or LWIR metalens is to succeed a lateral displacement with a fast response time and low power consumption.

Four optimization problems of

a) minimizing the actuation force directly related with current
b) maximizing the displacement under an actuation load
c) compactness
d) making decouple the actuation axis

are performed for the electromagnetic actuator.

The material of substrate is silicon and the conductor layer is gold. The variables of single beam are the initial height of the flexure (x1), the gap between the meandering part and the anchor (x2), the vertical size of the meander (x3) and the half-length of a beam (x4), as shown in figure.

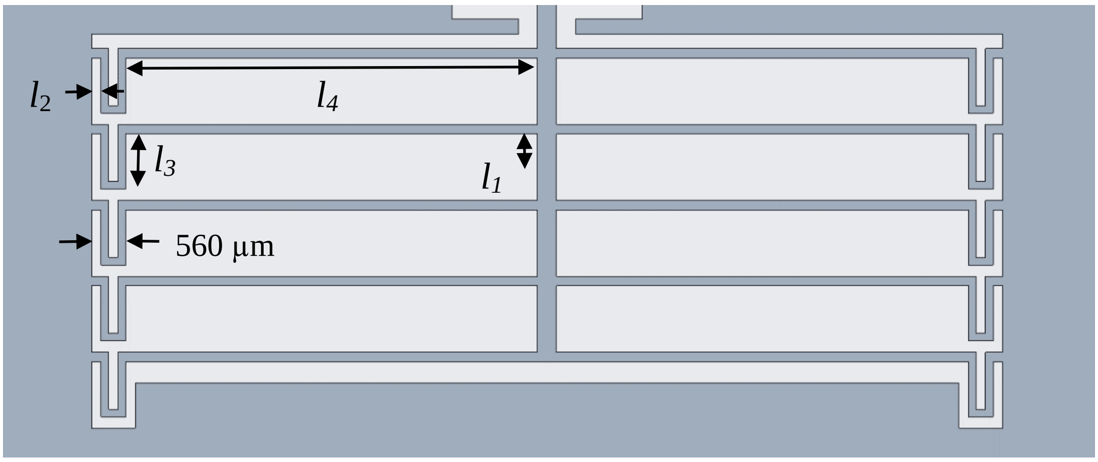

Figure 5.6 Variables of single beam actuator

The upper and lower bound of the variables defined as below.

Table 5.1. *Lower and upper limit of design variables.*

Design Variable	*Lower*	*Upper*
l_1 *(µm)*	0	225
l_2 *(µm)*	20	100
l_3 *(µm)*	200	500
l_4 *(µm)*	2000	4500

The optimization was executed by using the finite element method in the Ansys multiphysics analysis software. Total actuation force is calculated by using equation 18 for each wire and then is applied as line pressure (N/mm) at the analysis. A permanent magnet is placed at the bottom of substrate generating a magnetic field in the vertical direction. The magnetic flux density (B) of the permanent magnet is 1,4 Tesla (Newtons per Ampere meter).

After the parametric optimization of the structure with respect the requirements, the optimum values of variables are obtained as defined at table below where d is the displacement of actuator on metalens at the actuation axis, i is the applied current value, d_{couple} is the displacement of actuator on metalens sector at the other vertical coupled axis.

Table 5.2. *Comparison of Optimization Results*

d(µm)	l_1 *(µm)*	l_2 *(µm)*	l_3 *(µm)*	l_4 *(µm)*	$i_{req}(A)$
2.26	0	100	500	2000	4.5
19.794	0	100	500	4440	4.5
16.9	0	100	200	4440	4.5
26.415	225	100	500	4340	4.5

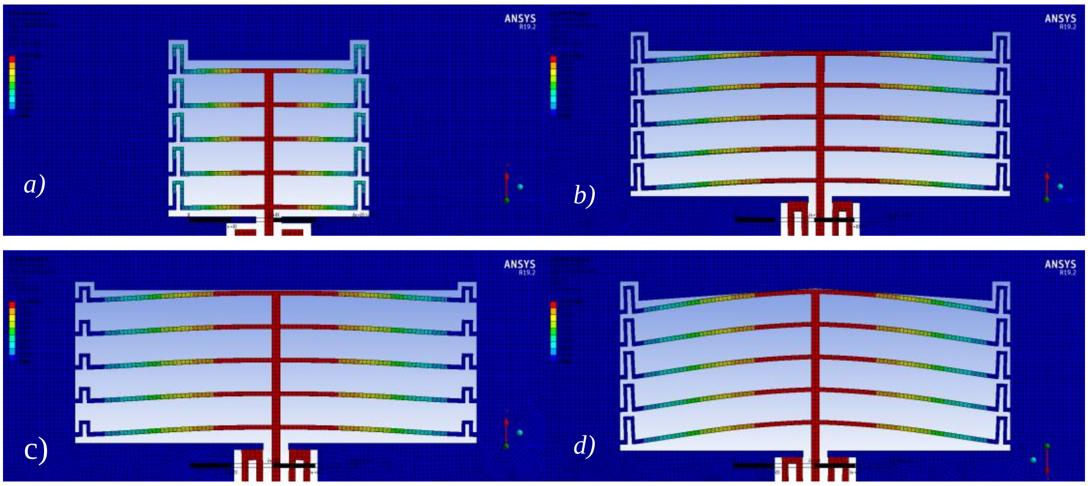

Figure 5.7 Deformation is visualized at 10x magnification a) d(μm)= 2.26 b) d(μm)= 19.794 c) d(μm)= 16.9 d) d(μm)= 26.415

Table 5.3. *Comparison of Optimization Results*

d(μm)	*Natural Frequency (Hz)*	*Maximum Stress(MPa)*	$d_{couple}(\mu m)$
2.26	2840	17.14	1.18×10^{-3}
19.794	2165	74.6	1.49×10^{-2}
16.9	2264.7	73,45	1.7×10^{-2}
26.415	2140.3	88.9	1×10^{-2}

Maximum actuation displacement has been obtained by performing many structural optimizations. Results show that slight modification of the shape of the micro actuator leads to a substantial improvement in the displacement-load response. The buckling behavior of the curved structure is the main reason for the large displacements of the actuator under actuation force. The maximum stress usually occurs at the connecting area of the flexure geometry of the meandering part and is not so crucial because the maximum value is much smaller than the yield stress. The actuation force is directly proportional with the number of the row that is limited by the effective area of structure and the placement of vertical axis actuators and their electrical contacts.

After optimization of the module of single electromagnetic actuator, the two axis decoupled electromagnetic actuator has been designed in detail. At the detailed design phase, arc-shaped actuator module supplying the highest displacement has been chosen and the parameters of the decouple flexure structure has been optimized for micro scanning and the stabilization of the metalens placed at the center of axis.

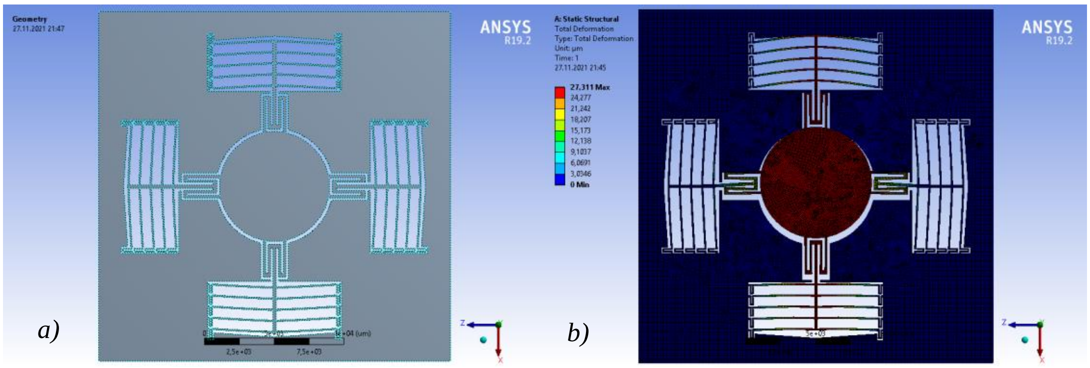

Figure 5.8 Actuator and metalens system design a) Design geometry b) Displacement behavior under actuation force

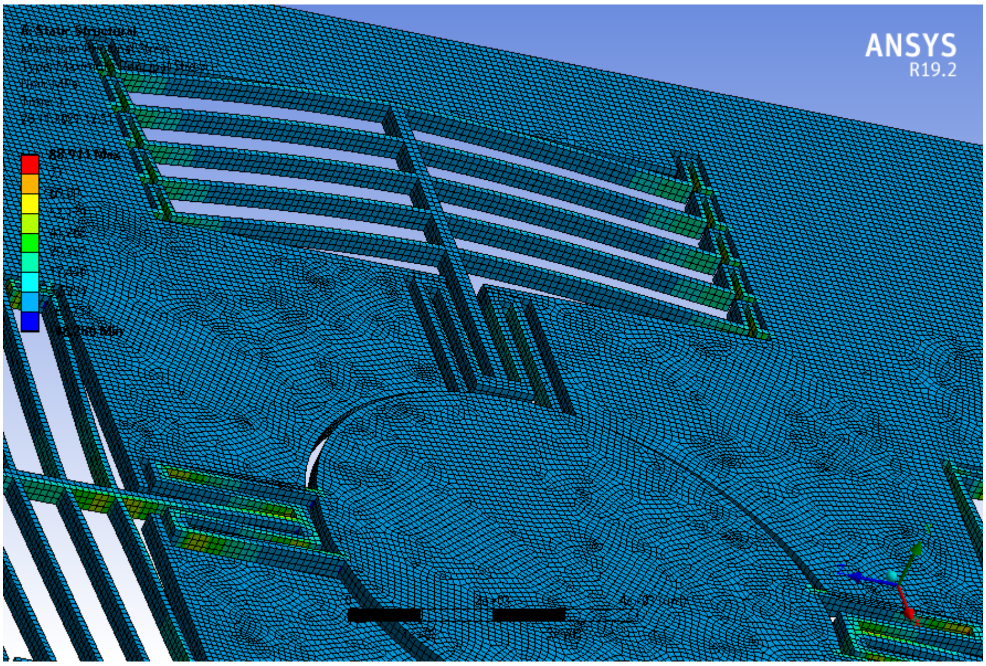

Figure 5.9 Maximum Stress – Stress distribution under actuation force

Table 5.4 and Figure 5.10 indicate the frequency results and displacement profile of modal analysis where natural frequency at mode 1 occurs at the direction of Y axis and the frequency of mode 2 and 3 same because of the axial symmetry of geometry occurs at the direction of X and Z axis.

Table 5.4. *Modal Analysis Results*

Mode	*Frequency [Hz]*
1,	2140.3
2,	2668.6
3,	2668.8
4,	3285.9
5,	4087.2
6,	4651.

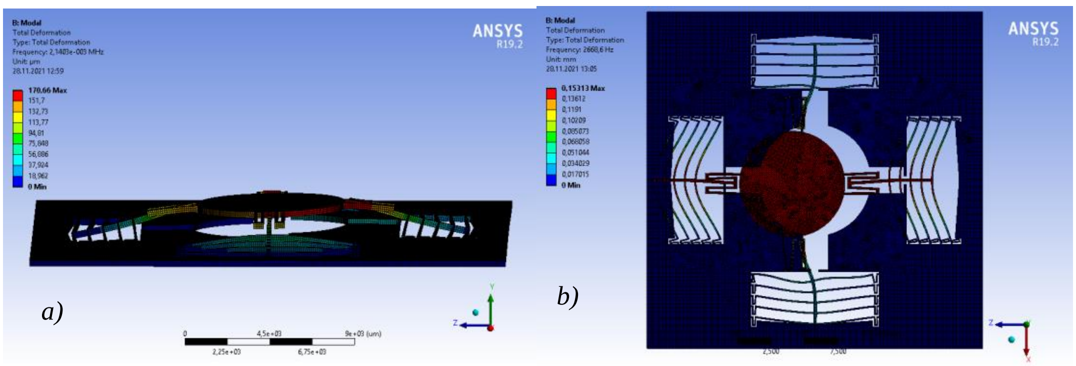

Figure 5.10 Natural Frequency – Mode 1(2140.3 Hz at Y axis) and Mode 2 (2668.6 Hz at Z and X axis) Results of Modal Analysis

The required power for actuation has been analyzed electro thermally on gold and thin aluminum film coating by using the finite element method. The resistivity of thin film aluminum becomes comparable to the bulk value for films thicker than ≈ 340 nm and The bulk resistivity of aluminum thin film coating (ρ_b) is 2.65 × 10−8 Ωm.

The thickness of a thin film conductor layer (th_c, µm) has been optimized to obtain required directional current density. The parameters of current flow (*I, mA)* are the cross-section area of the thin film coating on each conduction arm (A_{ca}, μm^2), directional current density (I_d, *mA/* μm^2), applied voltage difference (*V*, *volt*), time (*t*, *sec*).

$$I = A_{ca} \cdot I_d \tag{47}$$

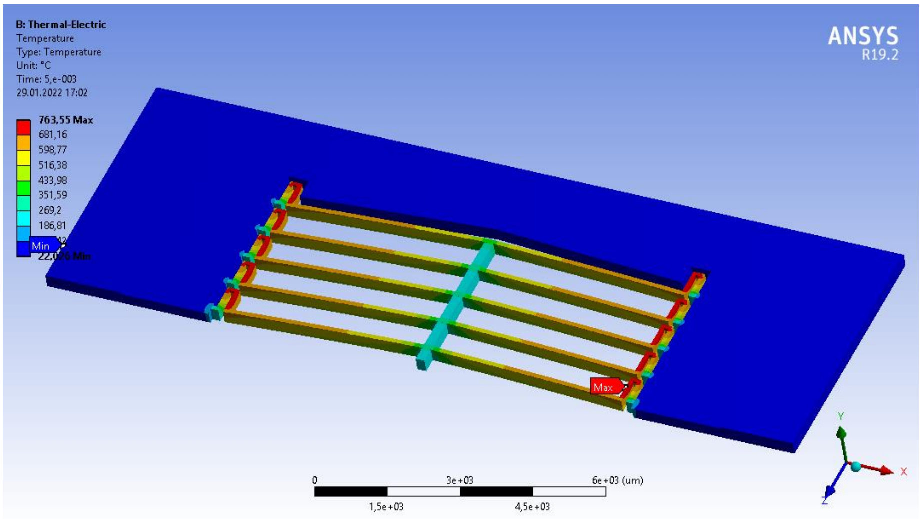

Figure 5.11 Temperature distribution of actuator having 4 μm thickness conductor layer excitation time 0.005 s and voltage 8V

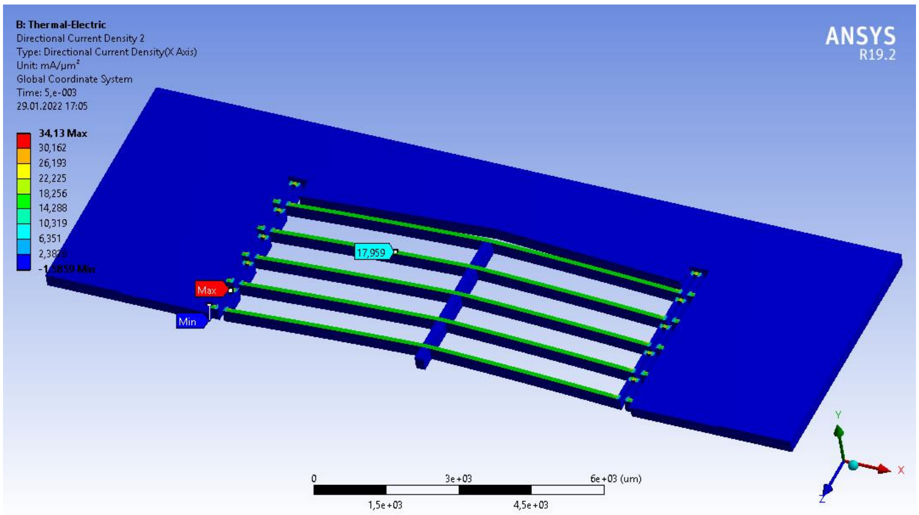

Figure 5.12 Directional Current Density of actuator having 4 μm thickness conductor layer excitation time 0.005 s and voltage 8V

Table 5.5. *Thermo-Electrical Analysis Results of Aluminum Thin Film Coating*

(th_c, µm)	V	A_{ca} , µm^2	I_d, *mA/* µm^2	*t, Time(s)*	*T, C^0*	*I , mA*
50	0.4	5000	0,895	Steady State	879	4475
50	0.4	5000	0,895	“	880	4475
50	2	5000	4.47	“	2675	22350
50	4	5000	8.953	“	3984	44756
20	0.6	2000	1.344	“	860	2688
20	1	2000	2,240	“	1285	4480
10	1	1000	2.24	“	1000	2240
10	2	1000	4.47	“	1621	4479
10	4	1000	8.959	“	2512	8959
10	1	1000	2.24	0.1	588	2240
4	1	400	2.24	0.1	157	895.9
4	4	400	8.959	0.1	1897	3583.6
4	4	400	8.959	0.02	540	3583.6
4	5	400	11.23	0.02	811	4480
4	8	400	17.96	0.01	1274	7184
4	8	400	17.96	0.005	763	7184

As seen from the table, the lowest electrical potential difference and steady state heating is obtained by using the 50 µm thickness of aluminum thin film coating for required current flow on each wire. However, coating thicker aluminum thin film is a difficult process. Sputtering is the best method to coat thicker aluminum thin film than other techniques. Sputtering process capability to coat aluminum on silicon wafer defines the system parameters. The first process trial indicated that 20 µm aluminum thin film can be coated by using sputtering. If 20 µm aluminum or gold thin film is not applicable, lower thickness (10 and 4 µm) cases are evaluated as well.

Another point that should be underlined is that the temperatures indicated in the Table 6.5 are steady state and transient temperatures. The temperatures will change depending on the excitation time. It is considered that a much lower temperature is obtained, since voltage is applied at low time intervals. Transient analysis shows that when applied voltage is increased and the time is decreased, the directional current density and frequency can be increased while the maximum temperature can be held below the critical level. As defined before, an increase at directional current density causes significant increase at the Lorentz Force on each actuator arm. In conclusion, with that method and adjusted parameters, frequency and force can be augmented and this is the superior property of this method. Flexures at the end of beams eliminate the buckling caused by heating.

CHAPTER 6

NOVEL MICRO SCANNING SYSTEM DESIGN BY USING MOEMS BASED THERMAL CHEVRON AND ELECTRO MAGNETIC HYBRID ACTUATOR

After studying MEMS-based thermal chevron and electromagnetic actuators separately, the advantages and disadvantages of both methods are revealed. It has been evaluated that some of these disadvantages can be reduced with a hybrid method and an actuator with better performance can be designed. When the literature was searched, it was seen that such hybrid solutions were not included much.

The thermal chevron structure basically changes the direction of the elongation and magnifies it by creating compression and buckling on the fixed beam at both ends with the elongation resulting from heating. Heating is achieved by passing the current through each beam. Similarly, current passes through the beam under the magnetic field to obtain the Lorentz force. If these two forces can be combined, the amount of displacement increases or the same displacement can be done by consuming less power and generating less heat.

With this approach, the magnetic field applied displacement and the heating behavior of the thermal chevron actuator were analyzed and investigated. The magnitude of excitation voltage, maximum temperature and displacement define the efficiency of the hybrid method.

In this chapter, the design, analysis, fabrication and test of novel MOEMS based hybrid actuator are demonstrated in detail.

6.1. The hybrid Actuator Design and Analysis

The chapter 4 and 5 define the whole theory of Thermal Chevron and Electromagnetic actuator designs, separately. When the magnetic field is applied to the proper direction on the Chevron actuator, the total applied force and displacement can be increased. A permanent magnet was placed under the chevron actuator and the current flow direction was arranged to obtain the force at the same direction chevron actuator's one. Neodymium is the material of the permanent magnet and the polarization axis of the magnet is vertical to the actuator.

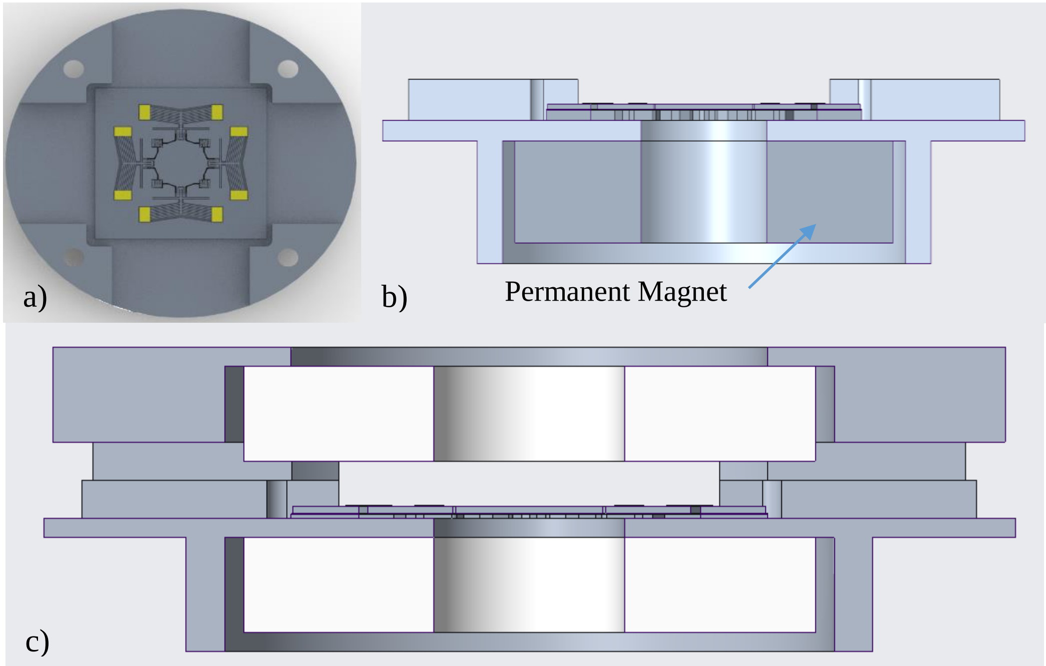

Figure 6.1 a) Top view and b) right view of single magnet hybrid system c) right view of double magnet capsulated hybrid system

The magnetic fields and the electromagnetic forces were tried to be analyzed by using Ansys Multiphysics modules where the specification of magnet and other materials, the current flow direction and the magnitude of it were defined and after that total and directional magnetic flux density, force and current density were analyzed. The residual induction and coercive force of Neodymium 35 magnet are 1,2 Tesla and $9x10^5$ A/m respectively. The direction of current flow was defined as below figure and the magnitude of it is 2 A. Neodymium magnets are graded by their maximum energy product (BH)max. N52 grade neodymium provides the greatest magnetic performance and N35 is the weakest. The magnetic properties of the various grades of neodymium magnets are adjusted by using varying amounts of rare earth elements in the alloy mixture, with each element adjusting the materials characteristics in a different way. If N52 grade magnet is used, the difference in the amount of displacement between chevron and hybrid actuator will increase by the difference in magnet energy. If a second magnet is placed on the actuator, placed between the two magnets, the magnetic field strength will increase, which will further increase the amount of displacement.

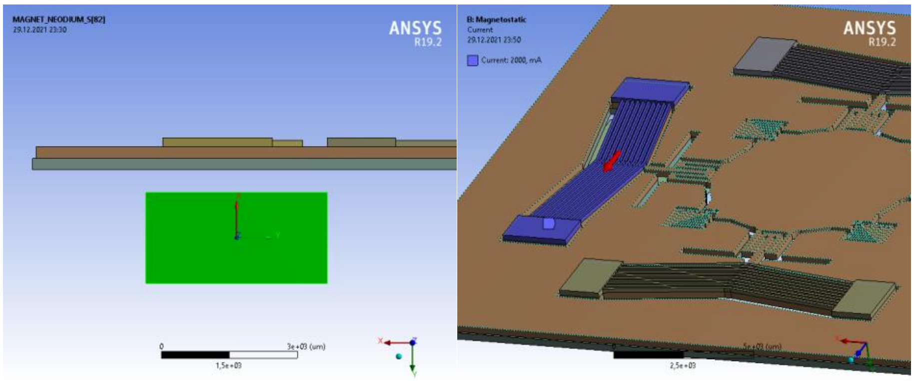

Figure 6.2 a) Polarization axis of magnet and b) current flow direction

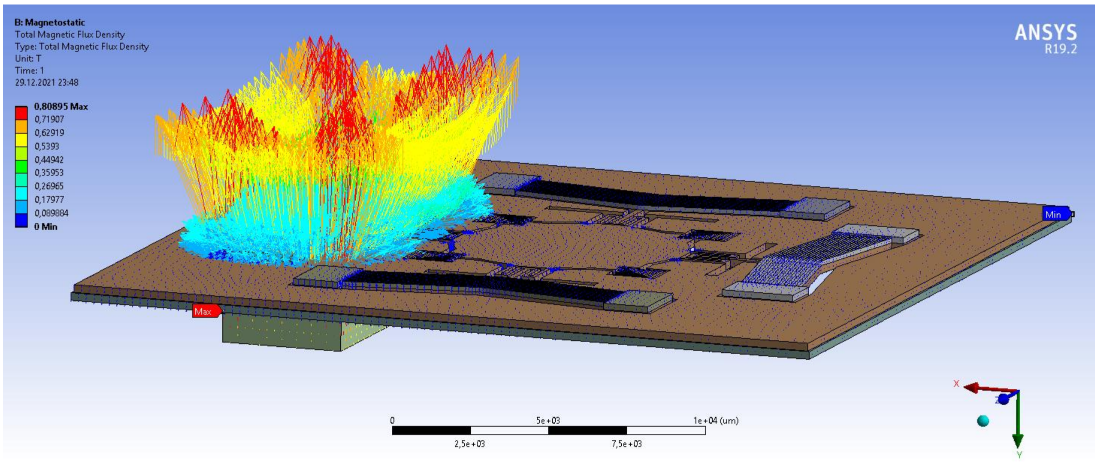

Figure 6.3 Total magnetic flux density caused by single permanent magnet

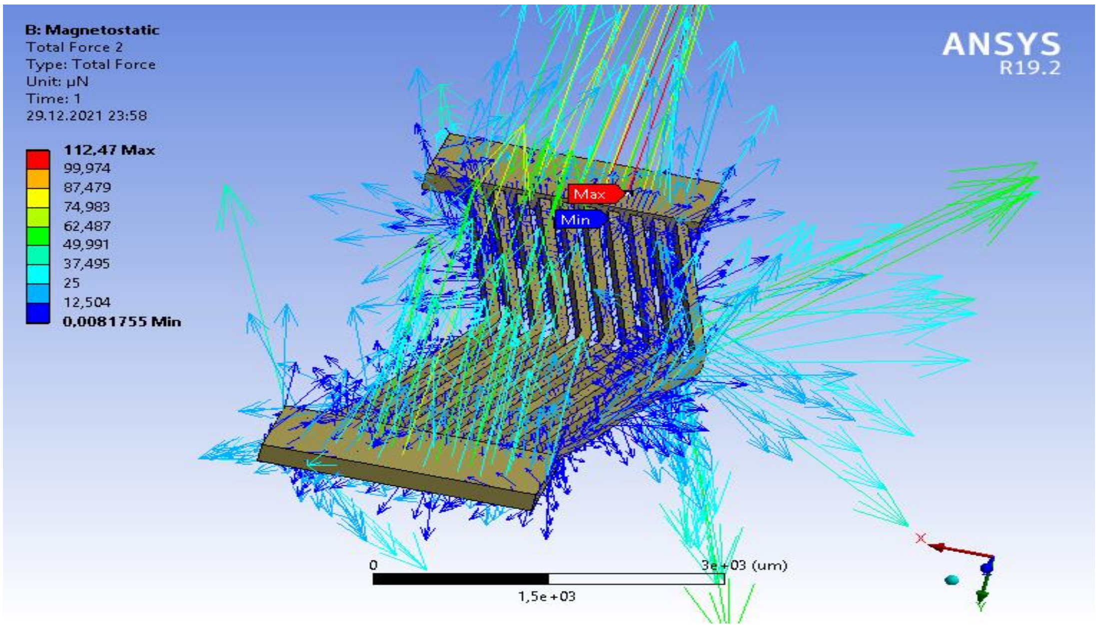

Figure 6.4 Total magnetic force distribution on the Chevron unit

Figure 6.4 demonstrates the electromagnetic force distribution on chevron unit. Forces in the x-axis direction contributes the displacement of the Chevron actuator.

Figure 6.5 Double magnet assembly prototype

Test results of the thermal chevron actuator can be used to calculate the electromagnetic forces on the actuators.

6.2. Displacement test of hybrid actuator package

The displacement test was performed by applying the same voltages to the actuator and magnet package and the results were compared with the results in chapter 5 in the graph below. As can be seen from the graph, when the same voltage difference is applied, the hybrid actuator system provides more displacement than the chevron structure due to the additional Lorentz force. The other meaning of this results is that same displacement can be achieved with less voltage difference and heating.

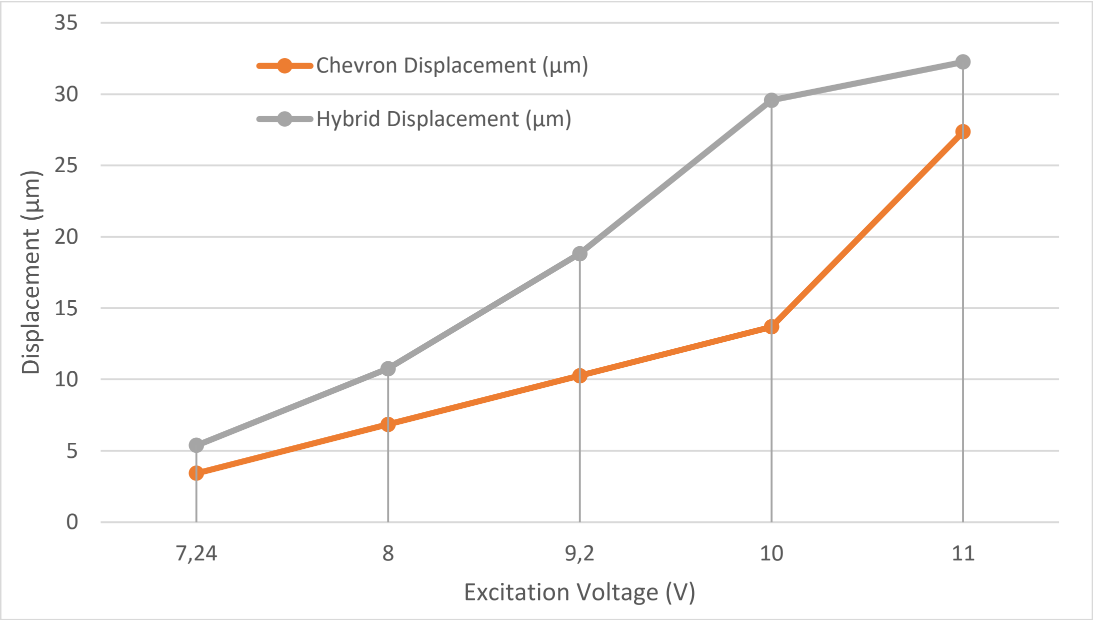

Figure 6.6 Displacement of thermal chevron and hybrid actuator

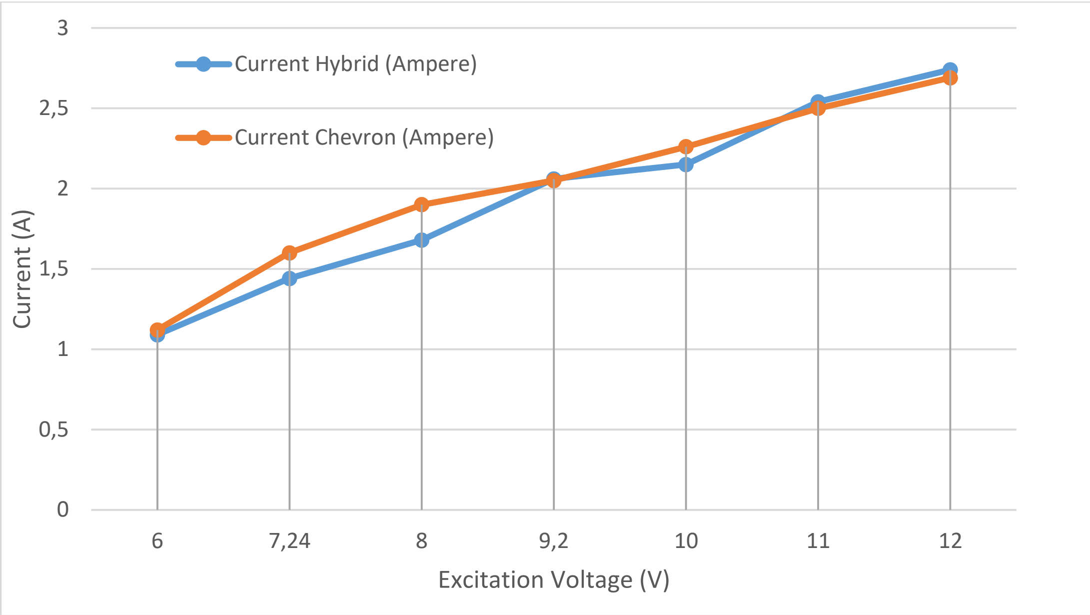

Figure 6.7 Current of thermal chevron and hybrid actuator

After examining the displacement amounts with the hybrid actuator, studies were started to test the dynamic behavior of the actuator at different frequencies. An oscilloscope, a signal generator, a dual output power supply and an H-bridge motor driver board are added to the probe station test setup.

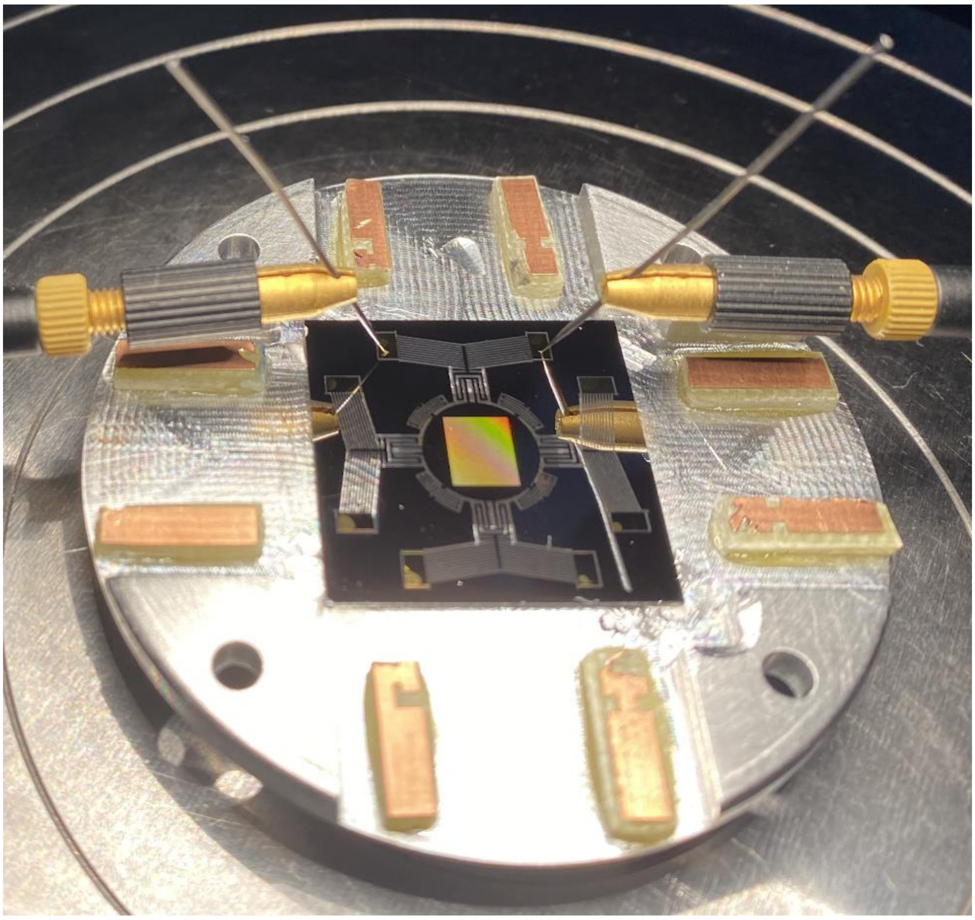

Figure 6.8 Permanent magnet and actuator assembly with probes of test station

The driven voltage was checked by connecting output cables to the oscilloscope. The motor driver board is driven by 12 V. By generating square wave at 2.5, 5, 7.5, 10 Hz with a signal generator, the motor driver board was fed and the output voltage of it was changed from 9 V to 16 V. The main difficulty in this test was the improper thickness and adhesion layer of gold contact region which prevented the application of high voltage to see high frequency dynamic behavior of the actuator. Microscope images for different frequency and excitation voltage were captured to investigate the motion. A code was written at Matlab to track the motion of actuator.

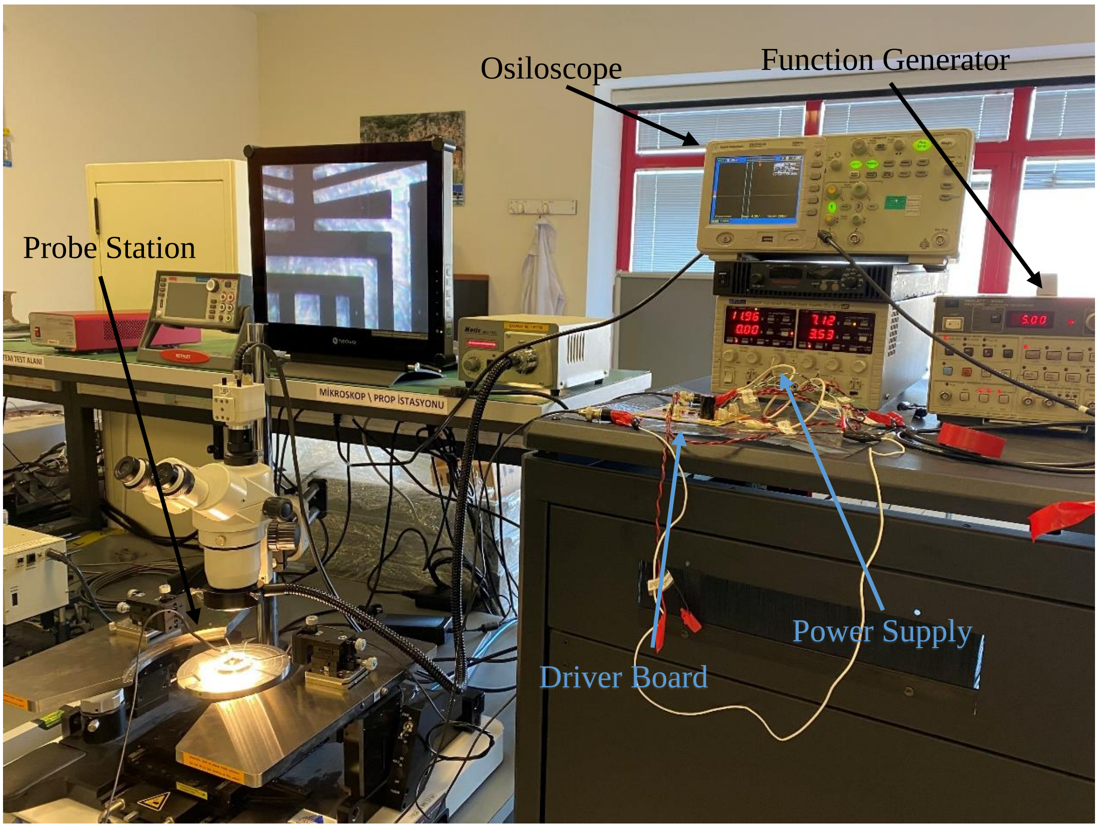

Figure 6.9 Test setup for frequent actuation

Figure 6.10 Oscilloscope screen for 5Hz frequency and 16 V excitation voltage

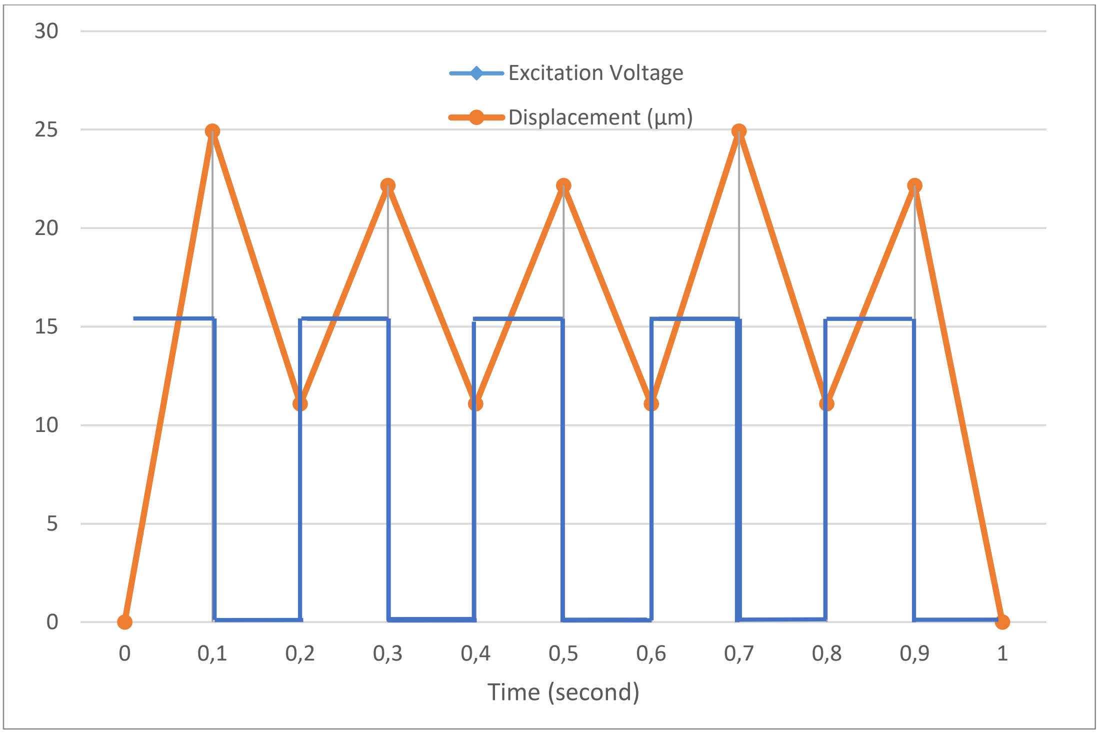

Figure 6.11 Displacement measurement and excitation voltage (5 Hz, 16 V) profile vs time

Figure 6.11 indicates that because of not enough time to cool down of actuator to room temperature at the tests, the constant displacement drift occurs while 5 Hz excitation. Therefore, scanning displacement decreases and the offset displacement shall be corrected by controller.

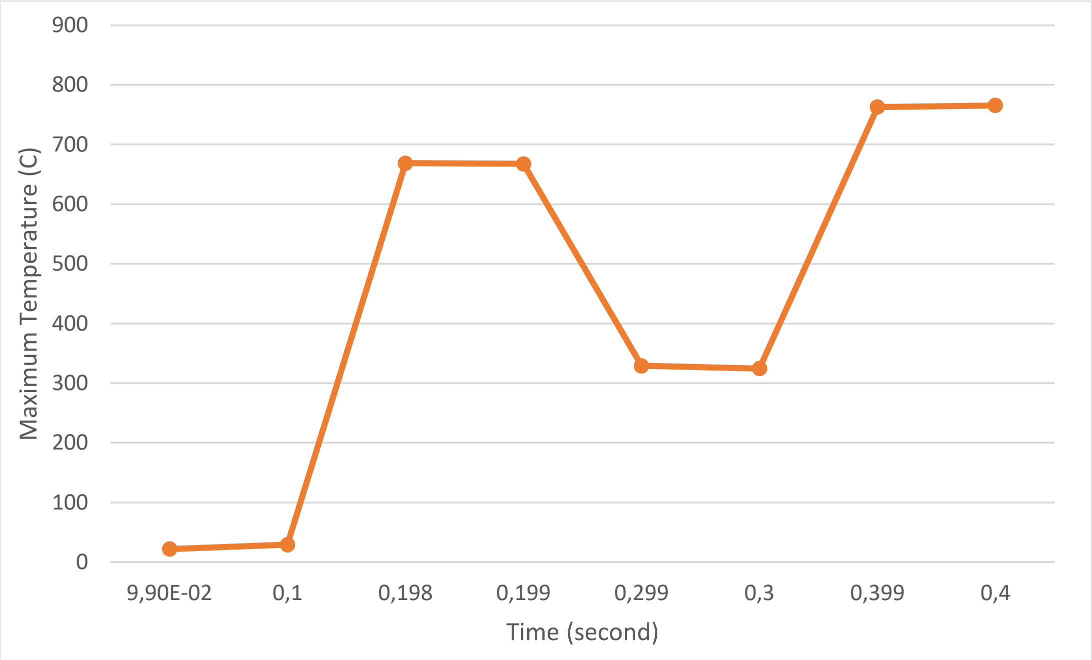

Figure 6.12 Maximum temperature profile with respect to the time for 5 Hz Excitation

The transient thermal electrical analysis performed with respect to the excitation frequency exhibits that the ambient cooling by convection for 0.1 second can reduce the temperature by half, approximately. This result is in agreement with the measurements at Figure 6.11.

However, the actuator excitation profile is different from the one at Figure 6.11 because there are 4 actuators and there is more cooling time. This significant difference is considered that this effect will be much less in real application.

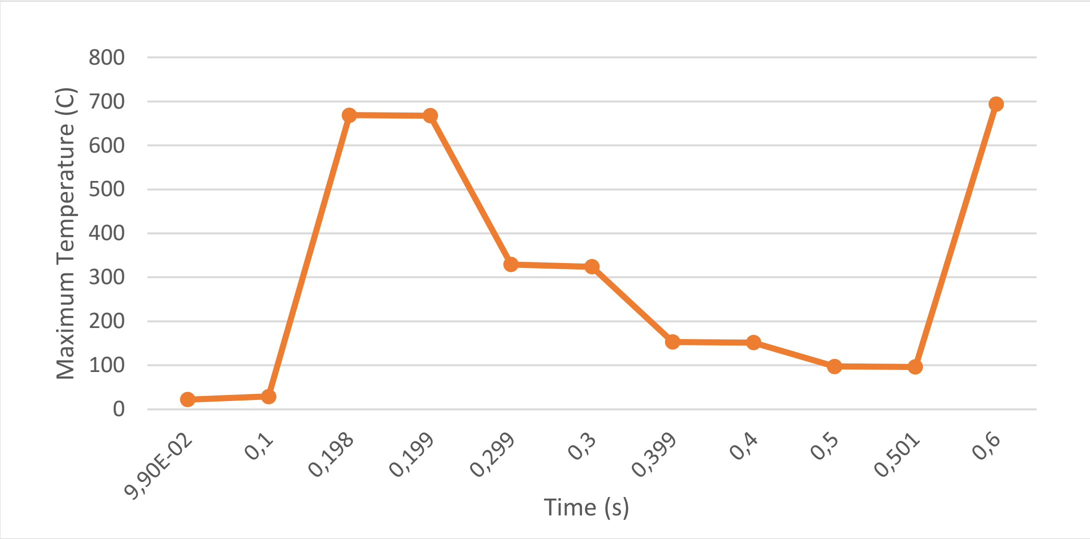

Figure 6.13 Maximum temperature profile with respect to the time for 5 Hz four actuator excitation serially

6.3. The Modified Hybrid Actuator Approach

The fact that the silicon wafer resistivity value mentioned in the chevron studies reduces the passing current and increases the amount of supply voltage needed, creates application difficulties. In the analyzes made in the hybrid approach, it has been seen that the thermal beams are also covered with conductive material, reducing the required supply voltage, reaching the desired temperature with low voltage, and with the decrease of the resistance. The wafer resistivity problems are prevented. The amount of current passing under the magnetic field increases and indirectly the amount of Lorentz force increases. In this way, it has been seen that the amount of displacement can be achieved with much lower electrical power consumption, and the force obtained under the magnetic field will reach the same levels as the single electromagnetic actuator. This method is a novel modified thermal and electromagnetic hybrid actuator approach.

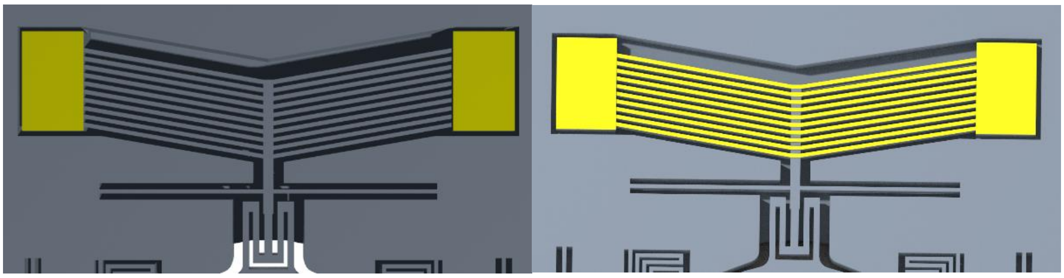

Figure 6.14 Hybrid and modified hybrid actuator arms

Table 6.1. *Thermo-Electrical Analysis Results of Actuation Methods*

Method	V	A_{ca} , μm^2	I_d, mA/ μm^2	T, C^0	I , mA
Chevron	10	40000	4.23e^{-3}	772	169.2
Electromagnetic	0.7	2000	2.33	708	4660
Hybrid	10	40000	5.19e^{-3}	737	207.6
Modified Hybrid	0.4	2000	1.7565	717	3513

Table 6.1 demonstrates that same heating can be obtained with less excitation voltage and high current density by using a modified hybrid actuator. The meaning of same heating is the same displacement for same chevron structure. For the magnetic and hybrid actuator, the thickness of conductor layer defines the magnitude of the applied voltage. As demonstrated in Table 6.1, when the thickness of conductor layer decreases, the applied voltage increases inverse proportionally. Therefore, the sputtering coating method can be used to obtain a conductor layer coating as thick as possible. At Table 6.1, the coating thickness of conductor layer is assumed as 20 μm. If thinner coating is applied like 4 μm (means lower cross section area of conductor), the required voltage difference is 8 V for the modified hybrid actuator for heating within a short time interval.

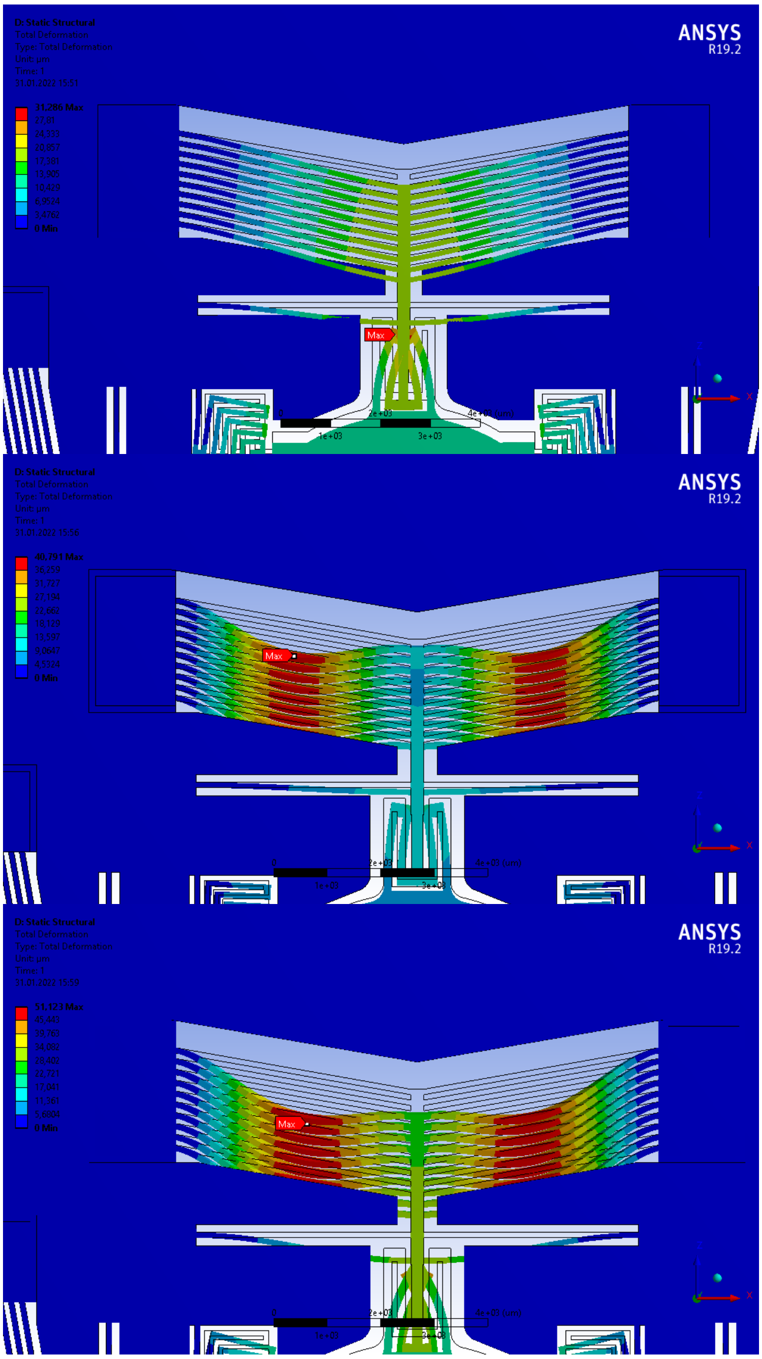

Figure 6.15 a) Thermal b) Electromagnetic c) Hybrid displacements at 11V excitation voltage (Scale=17)

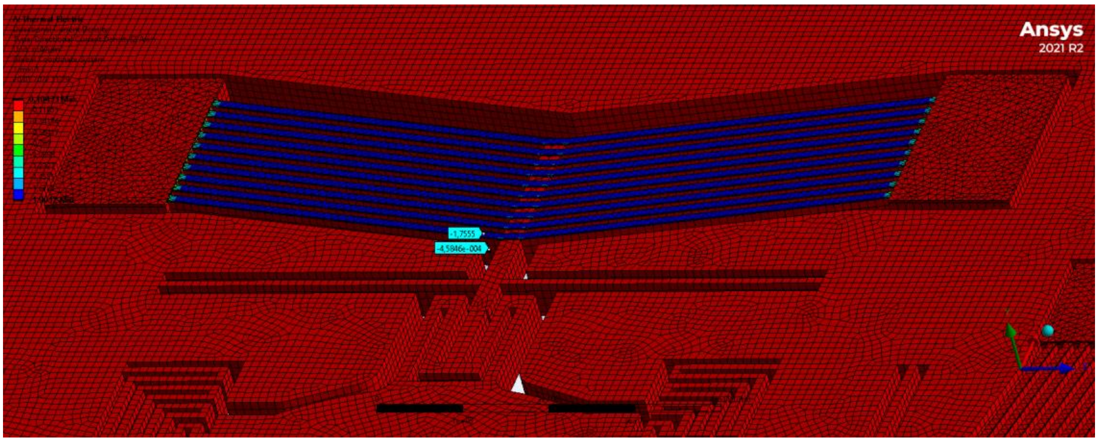

Figure 6.16 Directional current density on conductive gold and silicon layer

On the other hand, high current density means the high Lorentz force under same magnetic field. With these two effects, displacement of the actuator is increased with respect to the other methods and device layer resistivity of SOI will not be a concern anymore. Maximum heating shall be lower than the melting point of conductive layer such as 1064 degree Celsius for a thin film Au.

Table 6.2. *Displacement Results of Actuation Methods*

Method	V	A_{ca} , µm^2	I_d, $mA/$ µm^2	Δd_z, µm
Thermal	11	2000	4.23e^{-3}	20.38
Electromagnetic	11	2000	1.7565	7.56
Modified Hybrid	11	2000	1.7565	27.94

Δd_z is the directional displacement of center column of actuator at Z axis. As seen from the Table 6.2 and Figure 6.15, modified hybrid actuator has highest displacement because of the resultant force of thermal and electromagnetic.

$$F_{total\_hybrid} = F_{magnetic} + F_{thermal} = N.(F_{int} sin\theta + BIL) \tag{48}$$

In addition, the center of the beam has the highest displacement due to the electromagnetic force. This case is caused by the fixed end of thermal beam and reduces the effect of the electromagnetic force. If a flexure is added to the end of beam, the effect of electromagnetic force can be improved but this time, the displacement from thermal expansion caused by buckling of beam reduced. This situation is a pure design optimization problem.

CHAPTER 7

CONCLUSION, DISCUSSION AND FUTURE RESEARCH

The objective of this study is to develop a novel Thermal and Electromagnetic Hybrid MOEMS Microscanner with integrated spatial light modulation and metalens for resolution enhancement and stabilization of infrared imaging systems. There are many different types of macro actuation and MOEMS based systems for scanning, steering and modulating the light in the literature or market. Macro actuators have high power consumptions with large power electronics and need high volume in optical layouts. On the other hand, most of the MOEMS can be applied to the micro imaging systems with millimeter or sub-millimeter aperture like micro microscopes because of the size limitation of micro fabrication techniques. The DMD and adaptive mirror are major exceptions for this definition but it needs a fold in the optical architecture and the foot print of rays should fit in the clear aperture of the DMD and execute only at reflection mode which may not be possible every time. The MOEMS demonstrated here has an ultra-compact design, low cost, low power consumption, high displacement and is applicable in centimeter-scale aperture. In addition, this system can be applied any infrared imaging system with a proper sized internal image plane and also fabricated with microelectronics fabrication techniques. The frequencies and displacement can be engineered by choosing an appropriate actuator beam length and number, thickness and magnetic field. A silicon substrate material with proper resistivity is fully compatible to execute at transmission mode.

Following conclusions can be obtained based on goals achieved during these studies:

1) A high load carrying capacity can be achieved with actuators designed with piezo ceramic materials. It is often necessary to use an amplification mechanism to increase the elongation amounts. Due to the high power requirement, a large size driver electronics is needed. This poses a problem for miniaturization. With the designed piezo actuator lens system, the resolution has been removed from being limited and an increase has been achieved. Very close results were obtained between the displacement obtained by the analysis and the displacement obtained in the prototypes. These results show that the piezo ceramic characterization is quite realistic.
2) With the changes made in the optical architecture, the reduction studies of the microscan system were carried out. The dimensions of the scanning lens have been reduced to dimensions that can be driven with MEMS actuators by using a diffractive surface. By designing a Novel MEMS-based thermal chevron actuator, the scanning of this lens has been tried to be obtained. In the experiments, the effects of the SOI structure reaching high temperatures under voltage were investigated. The points that require the improvement of the structure were determined in the tests.
3) Afterwards, the optical architecture and resolution enhancement method were completely changed and the dimensions of the structure were halved and a coded mask was placed instead of the lens. In this way, the lens production process was removed and the structure was made completely producible with microfabrication methods. Since the production of the coded mask structure was done at the same time as the contact, there was no need for an additional process. The main source of the differences in the results obtained in the analyses and tests is the change in the properties of the silicon material according to the crystal orientation and temperature. The analyses were repeated with some results obtained in the tests and the results. The contact points were scraped and the connection to the cards was made with wire

bonding. Wire bonding did not carry the current they should carry and some of them ruptured. Afterwards, the tests were continued with the probe station.

4) After determining the whole character of the chevron type actuator, a micro-scanner design was made with an electromagnetic actuator. With this alternative design made, the parameters and values required to obtain the desired displacements were determined. Unlike the thermal chevron structure, since the current passes through the conductive layer in the electromagnetic actuator, the thickness of this layer is critical in terms of the current carrying capacity. Aluminum and gold are used as the conductive material between the contacts. The maximum thickness of the aluminum coating has been studied by producing it with the sputter method. As can be seen in the analyses obtained here, a minimum of 20 μm thick aluminum coating is required to obtain low voltage excitation. If thick conduct layer cannot be achieved, excitation voltage has to be increased and the excitation time has to be shorten to prevent temperature increase in order not to exceed the melting point. Since SOI is not required for the electromagnetic actuator, the use of undoped wafers is possible. This allows the large-area fabrication of small dimensions with the stepper and the use of transmissive wafers at LWIR wavelengths, thus allowing metalens structures to be built into the actuator center.
5) In line with the studies mentioned above, the advantages and disadvantages, structural properties and behaviors of thermal and electromagnetic activators was clearly determined. In the light of this information, it was seen that there may be a hybrid actuator approach. In this context, the behavior of the chevron actuator under magnetic field was examined and tested. According to the results of the tests, it was observed that the amount of displacement obtained from the actuator increased under the magnetic field applied in the appropriate direction. Consequently, it has been seen that the hybrid actuator concept works.
6) The point of similarity for both actuators is Joule heating. In chevron actuators it is a goal for displacement, while in electromagnetic actuators it is a physical

result of displacement. Considering this phenomenon, it has been seen in the ongoing analyses that the hybrid actuator structure can be driven with a much lower voltage by a modification at conduction layer. Therefore, the current density on actuator arm and the resulting Lorentz force is increased. The main dissimilarity is the difference of beam end. The thermal actuator is needed to fixed end to obtain a buckling effect and displacement due to expansion and buckling. On the other hand, an electromagnetic actuator produces evenly distributed force on the beam and so that the end point of beam is needed to be flex by using a flexure structure. For modified hybrid actuation, this dissimilarity is the main optimization problem for application. In this application, with the modified optical architectures, the required displacement has been reduced to 7.5 μm. Therefore, the experiment results show that the displacement of the actuator satisfies the requirement. On the other hand, frequency is another critical parameter of the actuator. For the pure electromagnetic actuator, the frequency highly satisfies the requirement of the system. For a pure thermal actuator, cooling of the actuator defines the frequency of the actuator but the critical point here is that you do not need to wait cooling down to room temperature. An offset and drift occur on displacement profile and when the offset is eliminated with the controller of the actuator, cooling profile will not be a significant problem for thermal actuator. The most powerful property of the modified hybrid actuator is the instantaneous heating capability with a lower voltage that shortens the period significantly.

Many goals have been achieved and all objectives have been successfully completed within this study. However, there are still some further studies and improvements that can be done, in order to increase the performance of hybrid MOEMS micro scanner for resolution enhancement. These possible studies and improvements can be listed as follows:

1) In this study, it was observed that the conductive metal coating of actuators and the thickness of this layer are so critical to increase the magnitude of directional current density flowing through the actuator beams and to decrease the magnitude of voltage. In this way, the low resistivity requirement of substrate is eliminated and the SOI wafer options are increasing. In order to decrease the excitation voltage from 10 V to 0.7 V, the thickness of the conductive layer should increase from 4-5 μm to 20 μm. The analysis results demonstrate an inverse correlation between the thickness of conductive layer and excitation voltage. This is one of the key parameters for high performance and low power consumption of the system. Therefore, future fabrication should be planned for the highest thickness of the conductive layer that can be achieved with the thin film coating method.
2) It was observed that the transmission of silicon wafer at mid-wave infrared wavelengths depends on the resistivity of the wafer. At the test, the transmission of the wafer was not so good and the root cause of this problem was defined as the low resistivity of silicon layer. 50-100 ohm-cm resistivity gives better transmission at the required wavelength 3.6-4.8 μm. Conflicting requirements for high transmission and low resistivity for low power consumption can be solved by coating the beams with conductive layer defined in paragraph one.
3) At the displacement test, some samples had fatigue failure at the anchor structure because of residual micro crack arising at fabrication and high stress spots at maximum deflection. The main aim of this structure is to decouple the axis motion. There should be an optimization to improve the strength of anchor structure and the yield and to reduce the failure risk form fabrication without degrading the decouple and displacement performance of axis. To do this, stress at the anchor at maximum displacement position should be reduced by optimizing the thickness and length of structure.
4) Because of the small feature size of metalens, the stepper should be used for photolithography of the nano holes at metasurfaces. An 8-inch SOI wafer is

needed to use a stepper. For the prototyping of the metalens version, the design thicknesses should be optimized with respect to the device and handle layer of the 8-inch SOI wafer.

5) It was observed that the nickel adhesion layer of Au metal coating and the thickness of metal is crucial for ribbon or wire bonding. At the wire bonding trial, it was hard to get conduction and a special bonding solution was needed to use, but the disconnection occurred at the low current magnitudes. At the ribbon bonding trial for electrical connection, the metal layer peeled off and the bonding could not be achieved. Therefore, a titanium adhesion layer should be used for better adhesion of metal layers and also the thickness of metal layer should be higher than the previous process.

In conclusion, many various actuator and optical designs and also fabrication techniques were used to develop a novel MOEMS based micro scanner for resolution enhancement and stabilization of infrared imaging systems. In order to achieve desired performance, different multi physics finite element analysis methods like static structural, transient thermal-electric, modal, magnetostatic and harmonic were utilized with parametric optimization techniques. Also, the fabrication process of a MOEMS with coded mask, a novel MOEMS with metalens and an optical architecture with telecentric metalens doublet are proposed. It is evaluated that MOEMS based metalens applications will become widespread in literature and market in the future especially for infrared imaging.

REFERENCES

[1] Hoad, T . F., 2002, The Concise Oxford Dictionary of English Etymology. ,Oxford University Press,

[2] Frisius, G., 1558, De Radio Astronomico et Geometrico Liber, Lvtetiae

[3] Janesick, J. R., 2001, Scientific Charge-Coupled Devices, SPIE Press

[4] Daniels, A., 2018, Field Guide to Infrared Systems, Detectors, and FPAs, Third Edition, SPIE Press

[5] Zhang, X. F., Huang, W., Xu M. F., Jia , S. Q., Xu, X. R., Li, F . B., Zheng, Y. D., 2019, Super-Resolution Imaging for Infrared Microscanning Optical System, Optics Express, 1-19.

[6] Wiltse, J. M., Miller, J. L., 2005, Imagery improvements in staring infrared imagers by employing subpixel microscan. SPIE Optical Engineering 44(5), 056401 https://doi.org/10.1117/1.1917312

[7] Güngör, A., Kar, O., 2019, A Transform Learning Based Deconvolution Technique with Super-Resolution and Microscanning Applications., IEEE International Conference On Image Processing (ICIP). pp. 2159-2163

[8] Alam, M., Bognar, J., Hardie, R., Yasuda, B. , Infrared image registration and high-resolution reconstruction using multiple translationally shifted aliased video frames., IEEE Transactions On Instrumentation And Measurement. 49, 915-923 (2000)

[9] Stadtmiller, T., Gillette, J., Hardie, R. ,1995, Reduction of aliasing in staring infrared imagers utilizing subpixel techniques., Proceedings of The IEEE 1995 National Aerospace And Electronics Conference. NAECON 1995. 2 pp. 874-880 vol.2

[10] Bennett, C. R., Ridley, K. D., de Villiers, G.,D., Watson, P. J., Slinger, C. W., and Rogers, P. J., 2010, Optical design of a coded aperture infrared imaging system with resolution below the pixel limit, Proc. SPIE 7818, Adaptive Coded Aperture Imaging, Non-Imaging, and Unconventional Imaging Sensor Systems II, 78180H https://doi.org/10.1117/12.861396

[11] Aselsan Inc. Microelectronics, Electro-optical and Guidance Sector, 2022, https://www.aselsan.com.tr/MIKROBOLOMETRE_Sogutmasiz_Kizilotesi_Dedektorler_3673.pdf

[12] Opgal, 2022, https://www.opgal.com/blog/thermal-cameras/intro-to-ir-part-3-sensitivity-resolution-and-frame-rate/

[13] Edmund Optics, 2022, https://www.edmundoptics.com/knowledge-center/application-notes/optics/introduction-to-modulation-transfer-function/

[14] Fortin, J., Chevrette, P. C., 1996, Realization of a fast microscanning device for infrared focal plane arrays, Proc. SPIE 2743, Infrared Imaging Systems: Design, Analysis, Modeling, and Testing VII, https://doi.org/10.1117/12.241959

[15] Bell, D.J., Lu, T.,J.,2005, MEMS actuators and sensors: observations on their performance and selection for purpose, J. Micromech. Microeng. 15 S153–S164
[16] PI, How Does a Piezo Flexure Stage Work - Why use Piezo Nanopositioning Stages?,2022,https://www.pi-usa.us/en/products/piezo-flexure-nanopositioners/pztflexurenanopositioners-2-3/
[17] D. Hayne, What is image stabilization and does Nikon D7200 have it?, 2019, https://www.quora.com/What-is-image-stabilisation-and-does-Nikon-D7200-have-it
[18] Algamili, A.S., Khir, M.H.M., Dennis, J.O., 2021, A Review of Actuation and Sensing Mechanisms in MEMS-Based Sensor Devices. Nanoscale Res Lett 16, https://doi.org/10.1186/s11671-021-03481-
[19] Nielson, G.N,. Barbastathis, G. ,2006, Dynamic pull-in of parallel-plate and torsional electrostatic MEMS actuators., Journal of Microelectromechanical Systems 15(4):811–821
[20] Yang, S., Xu, Q., ,2017, A review on actuation and sensing techniques for MEMS-based microgrippers. J Micro-Bio Robot 13:1–14
[21] Bao, M., ,2005, Analysis and design principles of MEMS devices. Elsevier, Amsterdam
[22] Huang, Q.A, Lee, N.K.S., 1999, Analysis and design of polysilicon thermal flexure actuator. J Micromech Microeng 9(1):64
[23] Younis, M.I.,2011, MEMS linear and nonlinear statics and dynamics., Springer, Berlin
[24] Allen, J.J. ,2005, Micro electro mechanical system design. CRC Press, Cambridge
[25] Motamedi, M. E., 1993, Merging Micro-optics with Micromechanics: Micro-Opto-Electro-Mechanical (MOEM) devices, Critical Reviews of Optical Science and Technology, V. CR49, SPIE Annual Meeting, Proceeding of Diffractive and Miniaturized Optics, page 302-328, July, 1993
[26] Motamedi, M. E, MOEMS: Micro-opto-electro-mechanical Systems, SPIE Press, Bellingham
[27] Plander, I., Stepanovsky, M.., 2016, MEMS optical switch: Switching time reduction. Open Computer Science. 6. 10.1515/comp-2016-0010.
[28] Lin, C-Y., Chiou, J-C.,2012, Design and Fabrication of MEMS-Based Thermally-Actuated Image Stabilizer for Cell Phone Camera, Solid-State Electronics, 64-77.
[29] Zhou, L., Yu, X., X.-L., Feng, P., Li, J., Xie H., 2020, A MEMS lens scanner based on serpentine electrothermal bimorph actuators for large axial tuning. Opt. Express 28, 23439-23453
[30] Yu, N., Capasso, F.,2014, Flat optics with designer metasurfaces. Nature Mater 13, 139–150 (2014). https://doi.org/10.1038/nmat3839
[31] Roy, T., Zhang, S. Jung, W., Troccoli, M., Capasso, F., Lopez, D., 2018, Dynamic metasurface lens based on MEMS technology, APL Photonics 3, 021302
[32] Arbabi, E., Arbabi, A., Kamali, S. M., Horie Y., 2018, MEMS-tunable dielectric metasurface lens, Nature Communications, DOI: 10.1038/s41467-018-03155-6

[33] Han, Z., Colburn, S., Majumdar, A. ,2020, MEMS-actuated metasurface Alvarez lens. Microsyst Nanoeng 6, 79 (2020). https://doi.org/10.1038/s41378-020-00190-6
[34] Subbarao, M., Lu, M-C., 1999, Computer Modeling and Simulation of Camera Defocus, Proceedings of Spie - The International Society for Optical Engineering, 1-24.
[35] Letty, R. L., Barillot, F. , Fabbro, H., 2004, Piezoelectric actuators for active optics, International Conference on Space Optics—ICSO 2004
[36] Senousy, M., 2013, Piezoelectricity In Ansys Mechanical, Say Goodbye To Command Snippets!, 1-10.
[37] IEEE, Standard on piezoelectricity. IEEE Transactions on Ultrasonics Ferroelectrics and Frequency Control, 1996. 43(5): p. A1-A54.
[38] Samsung Electronics Co. Ltd, California Institute of Technology, 2021, Patent: US2021/0318516 A1
[39] Enikov, E. T., Kedar, S. S., Lazarov, K. V.,2013, Analytical Model for Analysis and Design of V-Shaped Thermal Microactuators, IEEE Journal of Microelectromechanical Systems, 14. 788–798.
[40] Yilmaz, N., Çetin, R., Sozak, A., Yasan, E., 2021, High Efficiency Nanohole Based Immersion Metalens for Light Concentration, SPIE Nanoscience+Engineering Vol. 11795, Metamaterials, Metadevices and Metasystems
[41] Sozak, A., Azgın, K., Şimşek, E., 2019, A MEMS Based Lens Microscanner for Resolution Enhancement of Infrared Imaging Systems, IEEE Sensors,
[42] Lobontiu, N., Garcia, E., 2003, Analytical Model of Displacement Amplification and Stiffness Optimization for A Class of Flexure-Based Compliant Mechanisms, Comput.Struct., 81. 2797–2810.
[43] Duzng, N. T., 2018, Modeling and Simulation of V-Shaped Thermal Actuator, American Journal of Engineering Research, 222-227
[44] Lv, X., Wei, W., Mao, X., Chen, Y., Yang, J., Yang, F., 2014, A Novel Mems Electromagnetic Actuator with Large Displacement, Sensors and Actuators, P: 23-28.
[45] Zand, J., 1996, Coded aperture camera imaging concept, NASA Astrophysics Science Division, https://asd.gsfc.nasa.gov/archive/cai/coded_intr.html
[46] Tang, X., Chen, I-M., Li, Q.,2006, Design and Nonlinear Modeling of a Large-Displacement Xyz Flexure Parallel Mechanism with Decoupled Kinematic Structure, Review of Scientific Instruments, 77. 1-11.
[47] Sun, C-M., Wu, C-L, Wang, C., Chang, C-L., Yip, M-C, Frang, W, 2012, Implementation of Complementary Metal Oxide Semiconductor Microelectromechanical Systems Lorentz Force Two Axis Angular Actuator, Japanese Journal of Applied Physics, 1-5
[48] Baracu, A., Voicu, R., Müller R., Avram, A., Pustan, M., Chiorean R., Birleanu, C., Dudescu, C., 2015, Design and Fabrication of a Mems Chevron-Type Thermal Actuator, Aip Conference Proceedings, P:25-29

[49] Huang, Q-A., Ka, N., Lee, S., 1998, Analysis and Design of Polysilicon Thermal Flexure Actuator, Journal of Micromechanics and Microengineering, 64-70.
[50] Milman, Y. V., Gridneva, I. V., Golubenko, A. A., 2007, Construction of Stess-Strain Curves for Brittle Materials by Indentation in A Wide Temperature Range, 67-75.
[51] Marxer, C., De Rooij, N. F.,1999, Micro-Opto-Mechanical 2 2 Switch for Single-Mode Fibers Based on Plasma-Etched Silicon Mirror and Electrostatic Actuation, Journal of Lightwave Technology, 2-6.
[52] Jeong, S., Han, S., Ko, J. S., Korvink, J. G., 2014, Structural Optimization of a Large Displacement Electromagnetic Lorentz Force Microactuator for Optical Switching Applications, Journal of Micromechanics and Microengineering, 1585-1596.
[53] Xie, H., Zhao, M., Wang, Y., Chen, H., Yang, T., Yang, L.,2019, Switchable Fov Infrared Imaging System Using Micro-Lens Arrays, Osa Continuum, 1925-1937.
[54] Vutukuru, M., Christopher , J. W., Pollock, C., Bishop, D. J., Swan, A. K., 2018, Modeling and Thermal Metrology of Thermally Isolated MEMS Electrothermal Actuators For Strain Engineering Of 2D Materials, Journal Of Microelectromechanical Systems, 2-8.
[55] Yosefi, G., Mirzakuchaki, S., Raissi, F., Afrang, S.,2014, Design and Analysis of A High Force, Low Voltage And High Flow Rate Electro-Thermal Micropump, Micromachines, P:1323-1340.
[56] Kim, Y-S., Shi, H., Dagalakis, N. G, Gupta, S.K., 2016, Design of A MEMS-Based Motion Stage Based on a Lever Mechanism for Generating Large Displacements and Forces, Journal of Micromechanics and Microengineering, 1-13.
[57] Lin, C-Y., Chiou, J-C., 2011, Design, Fabrication and Actuation of Four-Axis Thermal Actuating Image Stabiliser, Micro & Nano Letters, 549-552.
[58] Metalens - Zemax Interoperability, https://support.lumerical.com/hc/en-us/articles/360042097313-Metalens-Zemax-Interoperability
[59] Livermore, C., 2007, Design Choices: Mems Actuators, Design and Fabrication of Microelectromechanical Devices, MIT Open Course Lecture Notes, 1-21.
[60] Thiem, C. D., Collins, J. A., 2004, Mechanical Properties of Mems Materials, Air Force Research Laboratory, P: 7-45.
[61] Messenger, R. K., 2004, Modeling and Control of Surface Micromachined Thermal Actuators, 1-76.
[62] Akın, O., Demir, H.V., 2015, Mid-Wave Infrared Metasurface Microlensed Focal Plane Array for Optical Crosstalk Suppression, Optical Society of America, P: 1-8.
[63] Cho, A.R., Han, A., Ju, S., Jeong, H., Park J-H., Kim, I., Bu, J-U., Ji, C-H., 2015, Electromagnetic Biaxial Microscanner with Mechanical Amplification at Resonance, 1-11.
[64] Liu, T., Rajadhyaksha M., Dickensheets D. L., 2019, Mems-In-The-Lens Architecture for A Miniature High-Na Laser Scanning Microscope, Official Journal of The Ciomp, 1-11.

[65] Cragun, R., 2003, Thermal Micro Actuators for Microelectromechanical Systems (Mems), Byu Scholars Archive, 1-75
[66] Pokines, B.J., Garcis, E., 1998, A Smart Material Micro-amplification Mechanism Fabricated Using LIGA, Smart Material and Structure., 7. 105–112.
[67] Appapillaia, A. T., Sachs, E. M., 2011, A Method for Temperature Profile Measurement of Silicon Wafers in High-Temperature Environments, Journal of Applied Physics, 034902. 1-8.
[68] Akın, O., 2017, Metasurface Microlens Focal Plane Arrays and Mirrors, PhD Thesis Bilkent University Electrical and Electronics Engineering , 1-120
[69] Hopcroft, M., A., Nix, W. D., Kenny, T. W., 2010, What is The Young's Modulus of Silicon?, Journal of Microelectromechanıcal Systems, 229-238.
[70] Darius, D., Vaivods, T., 2018, Resistance of Aluminium Thin Films, School of Physics and Astronomy University of Manchester Second Year Laboratory Report, 1-8.
[71] Shah, J., 2012, Estimating Bond Wire Current-Carrying Capacity, Power Systems Design, 22-2.
[72] Rusu, C., Tatar, M. O., Besoiu, S., 2021, Design and Closed-Loop Control of a Piezoelectric Actuator, IOP Conference Series Materials Science and Engineering, 1-6.
[73] Madec, P-Y, 2012, Overview of Deformable Mirror Technologies for Adaptive Optics and Astronomy, P: 1-16.
[74] Qi, K.Q., Xiang, Y., Fang ,C., Zhang, Y., Yu, C.S., 2015, Analysis of the displacement amplification ratio of bridge-type mechanism, Mech. Mach. Theory, 87, 45–56.
[75] Sachs, D., Nasiri, S., Goehl, D., Image Stabilization Technology Overview, Digikey Electronics, 1-17.
[76] Staworko, M., 2008, Modeling and Simulation of Piezoelectric Elements-Comparison Of Available Methods And Tools, Mechanics, 161-170.
[77] Stockham, A., Smith J. G.,2006, Tolerancing Microlenses Using Zemax, Society of Photo-Optical Instrumentation Engineers, 1-12.
[78] Chen, P-S., 2006, Analysis and Design of a Piezoelectric Micro-Actuator, 3-86.
[79] Yan, J., Maekawa, K., Tamaki, J., Kuriyagawal, T.,2005, Micro Grooving on Single-Crystal Germanium For Infrared Fresnel Lenses, Journal of Micromechanics And Microengineering , P: 1925-1931.
[80] Mukaida, M., Yan, J., 2017, Fabrication of Hexagonal Microlens Arrays On Single-Crystal Silicon Using the Tool-Servo Driven Segment Turning Method, Micromachines, 1-18.
[81] Rosli, A., Manaf, A., Sugiyama, T., Yan, J., 2017, Design and Fabrication of Si-Hdpe Hybrid Fresnel Lenses for Infrared Imaging Systems, Optics Express,1-19.
[82] Shaikh, H., Pawade, R., Brahmankar, P.K., 2016, Some Investigations in Single Point Diamond Turning of Germanium Aspheric Lens, International Conference On Advances In Mechanical And Material Sciences,1-13.
[83] Jónsso, E., 2009, Nonlinear Thermal Electric Analysis of Platinum Microheaters, Sigillum Universitatis Islandiae ,17-78.

[84] System Plus Consulting, Apple’s novel Sensor-shift OIS in the iPhone 12 Pro Max camera, https://www.reverse-costing.com/teardown-notes/apples-novel-sensor-shift-ois-iphone-12-pro-max-ca/

CURRICULUM VITAE

PERSONAL INFORMATION

Surname, Name	: Sözak, Ahmet
E-mail	: e120152@metu.edu.tr

EDUCATION

Degree	Institution	Year of Graduation
MS	METU Mechanical Engineering	2007
BS	METU Mechanical Engineering	2004
High School	Bursa Science High School, Ankara	1999

WORK EXPERIENCE

Year	Place	Enrollment
2004-Present	Aselsan	Manager

FOREIGN LANGUAGES

Advanced English,

PUBLICATIONS

1. A. Sozak, K. Azgın and E. Şimşek; A MEMS Based Lens Microscanner for Resolution Enhancement of Infrared Imaging Systems, IEEE Sensors, 2019

2. N. Yilmaz, R. Çetin, A.Sozak, E. Yasan; High Efficiency Nanohole Based Immersion Metalens for Light Concentration, SPIE Nanoscience+Engineering Vol. 11795, Metamaterials, Metadevices and Metasystems 2021

3. A. Sozak, E. l. Konukseven and M. Dolen; Uncertainty Analysis Methods for Coordinate Measuring Machines Measurements; International Conference on Advanced Design and Manufacture, Vol. 419-420 (2010), pp 63-66

4. A. Sozak, E. l. Konukseven and M. Dolen; An Uncertainty Analysis Software for CMM Measurements, International Conference on Advanced Design and Manufacture, Vol. 419-420 (2010), pp 67-70

HOBBIES

Basketball, Movies, Motor Sports